PROTON MAGNETIC RESONANCE OF LUNG

Mohammadreza Estilaei

B. Sc. (Physics) University of California, Riverside

M. Sc. (Physics) University of California, Riverside

A THESIS SUBMITTED IN PARTIAL FULFILMENT OF

THE REQUIREMENTS FOR THE DEGREE OF

DOCTOR OF PHILOSOPHY

in

THE FACULTY OF GRADUATE STUDIES

DEPARTMENT OF PHYSICS

We accept this thesis as conforming

To the required standard

THE UNIVERSITY OF BRITISH COLUMBIA

March 1998

In presenting this thesis in partial fulfilment of the requirements for an advanced degree at the University of British Columbia, I agree that the Library shall make it freely available for reference and study. I further agree that permission for extensive copying of this thesis for scholarly purposes may be granted by the head of my department or by his or her representatives. It is understood that copying or publication of this thesis for financial gain shall not be allowed without my written permission.

Department of Physics

The University of British Columbia

1956 Main Mall

Vancouver, Canada

Date: March 27, 1998

Abstract

A major problem currently in magnetic resonance imaging is the paucity of specificity and accurate quantification of NMR parameters for clinical use. If the lack of specificity is eliminated and accurate quantification is achieved, it would help physicians and radiologists to employ current therapies more effectively.

Proton nuclear magnetic resonance ^{1}H NMR was used to investigate the entire signal from excised lung tissue. The free induction decay signal contained a motionally restricted component which decayed in a few 10's of μs and a mobile component which persisted about 10 ms or longer. The motionally restricted component was characterized by the second moment of its lineshape which had an average value of $3.42 \pm (0.25) \times 10^9 s^{-2}$. This value was about 1/3 of the rigid lattice M_2 value, indicating that long macromolecules undergo considerable anisotropic motion on the NMR timescale.

The mobile component of the lung was characterized by its T_2 relaxation times which relate to the microscopic tissue environment. Due to the inhomogeneous nature of the structure and biochemical composition of lung, a smooth T_2 distribution was assumed. The mobile signal consistently showed four resolvable components of T_2 range: 2-6, 10-40, 80-110, and 190-400 ms. The 2-6 ms component was present in a fully dehydrated preparation and was therefore assigned to a non-aqueous lung constituent.

Collagen is a major protein present in lung tissue and has high tensile strength, rigidity, and

binding affinity for water. For this reason, the dependence of the second moment, T_2 relaxation times, and T_2 relaxation amplitudes on collagen content were studied.

To determine the lung wet/dry ratio, the hydrogen content per unit mass for lung parenchyma and water were estimated in two ways: 1) on the basis of chemical content and 2) on the basis of comparison of restricted and mobile signals to the gravimetric (G) water content for a lung sample studied at a wide range of water contents. Lung Wet/Dry weight ratios were estimated from the free induction decays and compared with gravimetric measurements. The ratio of $(Wet/Dry)_{NMR}/(Wet/Dry)_G$ was $1.00 \pm (0.08)$ and $1.00 \pm (0.05)$ for the two methods of estimation.

The water content measurements were validated and T_2 distributions were determined in inflated, deflated, and perfused lungs on a clinical 1.5 T MRI scanner. The mean difference between the gravimetric and MRI water contents was $-4.1g \pm 7.6\%$ and an excellent linear correlation squared ($R^2 = 0.98$) was observed between the two independent measurements. A voxel-by-voxel investigation of the T_2 distribution in inflated lung was particularly informative. Plotting the global geometric mean T_2 versus lung-water density in inflated lung helped to differentiate two distinct regions separated by the lung water density of about 0.4 g/ml.

A spherical shell model was tailored to characterize the susceptibility-induced magnetic field gradients in inflated lung and a simulation was performed to assess the effect of diffusion alone on the T_2 decay curve. This approach demonstrated that the multiexponential nature of the T_2 distribution was largely due to diffusion of water molecules in the magnetic field gradients. This study also enabled measurements of the inherent T_2 relaxation. In addition, it was found that the inherent T_2 relaxation was dependent upon lung water density.

The estimation of the magnetic field gradients facilitated measurement of the apparent diffusion coefficient by collecting images at a fixed imaging time using a multiecho pulse sequence with different echo spacing. The apparent diffusion coefficient decreased from about $1.1 \times 10^{-5} cm^2/s$ to $1.7 \times 10^{-6} cm^2/s$ as diffusion time increased from 12 to 60 ms.

Table of Contents

List of Tables

List of Figures

Acknowledgement

I would like to take this opportunity to thank my supervisor, Dr. Mackay, for his guidance, enthusiasm, and ever lasting support throughout this research project. I also would like to extend my many thanks to every single member (Dr. M. Bloom, Dr. E. Burnell, Dr. S. Xiang, and Dr. J. Mayo) in my Ph.D. advisory committee for their input and direction. I also would like to thank Dr. Clive Roberts who educated me in the fine art of biochemical analysis of samples.

I also thank my parents for their encouragement over the years, my uncle and my aunt for their support, and all of my friends for all reasons they are very well aware of. I also would like to acknowledge the support made by Dr. John Elliott and Dr. John Gerogakakos.

Chapter 1

Introduction

1.1 Pulmonary Diseases

Chronic infiltrative lung diseases such as pulmonary fibrosis, hypersensitivity pneumonitus, and sarcoidosis are lung diseases which are characterized by inflammation. For instance, fibrotic lung disease is a chronic inflammatory disorder in which inflammatory processes in the lower respiratory tract injure the lung and modulate the proliferation of mesenchymal cells that form the basis of fibrotic scars [1, 2]. In this regard, the biological basis of pulmonary fibrosis is analogous to the process of normal wound-healing; any injury is followed by inflammation and then repair by the mechanism of scar formation.

In a simple minded approach, the injury in fibrotic lung disease causes breaks in the basement membrane and loss of epithelial cells of type I and generally involves the entire organ . The repair process, however, includes proliferation of mesenchymal cells along with the deposition of connective tissue and replacement of type I cells with type II which causes thickening the alveolar wall [3, 4]. Since the inflammation associated with fibrotic lung disease is mostly confined to the alveolar structures, it is referred to as an "Alveolitus". It is well known that inflammatory processes are driven by the immune system, or at least in part by immune complexes produced within the lower respiratory tract [5, 6]. All available evidence is consistent with the concept

that the fibrotic lung disease results from an uncontrolled and chronic inflammatory process caused by mediators which amplify the inflammation by recruiting inflammatory cells.

Cardiopulmonary diseases are another class of lung diseases responsible for more than three million hospitalizations and thirty thousand deaths annually in North America alone. Cardiopulmonary edema is characterized by an increase in lung water content and its severity is determined by the degree of dysfunction. It is worthwhile mentioning that pulmonary edema conveys different meanings to different specialists because of the diversity of cases that fall under their observations. The type of pulmonary edema under scrutiny is trauma to the lung. Pulmonary edema was investigated by Laennec in 1819, primarily from the pathological standpoint, and it was described as the infiltration of serum into the substance of this organ to such a degree as to diminish its permeability to the air in respiration [7]. Edema in the interstitium separates the microvascular circulation from alveoli. Interestingly enough, the descriptor in the original report on the syndrome used " The wet lung of trauma."

Pulmonary edema most often affects the lower lung lobes. The lungs increase in size and the affected areas become heavy, soggy and plum in colour [8, 9]. According to histological studies, edema first develops in peravascular spaces around the blood vessels and airways and there maybe a slight collection in alveolar corners. Finally, alveolar filling begins scattering and reducing the effective volume. There is not much known about the mechanism that causes alveolar edema, however, it seems to occur in an all-or-nothing fashion. The further development of this process frequently leads to adult respiratory distress syndrome (ARDS), damaging the lungs and ultimately resulting in respiratory failure.

1.2 Motivation

A large number of publications have shown that nuclear magnetic resonance (NMR) can be applied to the assessment of lung-water content, its distribution, and its relaxation-time properties. Due to its intrinsic and exquisite sensitivity to proton density, Magnetic Resonance Imaging (MRI) has the potential to quantify water content, measure relaxation times and determine the apparent diffusion coefficient in the lung accurately.

Reliable data are needed for each type of measurement mentioned above to improve upon the accuracy of MRI quantification. Since pathological processes alter water content, composition and/or conformation of tissue macromolecules, MR properties can be used to detect disease processes. For example, accurate quantitative knowledge of lung-water content is valuable information for determining edema fluid, for early diagnosis, and for patient management with pulmonary edema. To be more specific, acute inflammation is a lung condition which can be treated if diagnosed early enough. Otherwise, it progresses to an irreversible process named fibrosis. Also, when in the repair stage of acute inflammation, tissue characteristics are different from that of early development of the illness. As a result, we would expect to see these changes reflected in the relaxation times thereby helping differentiate the acute from the repair stage and this knowledge makes current therapies more effective. Since MRI offers the capability of performing measurements in a noninvasive and nondestructive method, it would be an ideal tool for assessment of these lung diseases. Hence, it would enable physicians to diagnose and treat these diseases promptly.

Measuring the diffusion coefficient of the water molecule is a powerful technique for studying

motions. The diffusivity of water may be modified by interaction with macromolecules or restricted by barriers. In biological tissues, protons exist in a variety of different environments and move in a random fashion due to Brownian motion. This random motion provides the spin-bearing protons with an opportunity to sample the surrounding tissue during the course of the experiment. Therefore, the measurement of how the magnetization decay curve is modified due to the diffusion process should enable us to obtain information on geometry, length scale, and transport properties. It is important to note that all these properties would change as the tissue characteristics change due to pathological alterations. Thus, diffusion is another significant parameter which could be measured by MRI and be used to monitor the lung tissue pathology and its structure.

1.3 Thesis Objectives

The aims of this thesis were:

- To understand the nature of the entire ^{1}H NMR signal from the lung, establish correlations between the ^{1}H NMR signal and its biochemical constituents, and to measure lung water content accurately *in vitro*.

- To validate the use of a whole body MRI scanner to measure water content in inflated lungs and comprehend the T_2 distribution as a function of lung water density.

- To establish a mechanism to account for the multiexponential nature of the T_2 distribution.

- To estimate the magnetic field gradients induced by the susceptibility difference at the air-tissue interfaces and the effect of diffusion on the T_2 distribution.

- To measure the diffusion coefficient of water in lung and investigate its dependence on diffusion

time.

The ultimate goal was to characterize pathological processes in the lung by measurement of lung water content, relaxation properties of the ^{1}H NMR signal, and diffusion.

1.4 Thesis Outline

The outline of the thesis is as follows. Firstly, a brief explanation of the respiratory system and the biochemical composition of lung are presented. The history of lung NMR is reviewed and insights into previous studies on topics such as relaxation times, water content, and diffusion measurements are given. The general theory of NMR relaxation and diffusion are covered in chapter two. Details of the experimental techniques are given in chapter three. The non-negative least squares fitting routine, which is used to analyze the relaxation measurements, is briefly described in the same chapter. This algorithm is designed to account for the multiexponential nature of the T_2 distribution in biological systems such as lung.

In chapter four, the entire NMR signal from lung is characterized and two distinct components are differentiated (motionally restricted and mobile components) based on their mobility. The second moment of the motionally restricted component is determined and its correlation with the collagen content is investigated. Also, the effect of incremental dehydration on the evolution of the second moment is monitored.

Chapter five covers *in vitro* water content measurements and relaxation times on excised lungs using the NMR spectrometer operating at 90 MHz. An incremental dehydration technique was applied to monitor the evolution of the T_2 relaxation times. It also helped us to assign the shortest T_2 time to the nonaqueous mobile protons such as cytoplasmic proteins and DNA

material. Furthermore, The correlation between the collagen content and various components of the T_2 distribution was investigated. Finally, the wet/dry ratio of the excised lung tissue was measured using two different techniques.

Chapter six includes *in vitro* water content and relaxation measurements performed on inflated lungs using a GE clinical imager operating at 1.5 T. T_2 relaxation measurements were also performed on deflated and *in vivo* lungs in order to extend our previous results and evaluate the significance of MRI technology as a noninvasive method utilized to diagnose the early stages of acute inflammatory diseases. A new global characterization of the T_2 distribution in the lung is introduced using the geometric mean T_2 concept. This concept was used to establish a unique correlation between the geometric mean T_2 distribution and the lung water content.

To understand the nature of the lung water density distribution as a function of the geometric mean T_2, the characteristics of the susceptibility-induced magnetic field gradient are investigated in chapter seven. This task was accomplished by tailoring a spherical shell model to depict the lung parenchymal region. This model is used to estimate the spatial distribution of the magnetic field gradient. Furthermore, this characterization and estimation of the magnetic filed gradient in conjunction with the CPMG pulse sequence are employed (in chapter eight) to determine the diffusion coefficient of lung water. Also, the dependence of the apparent diffusion coefficient on diffusion time is examined.

1.5 Lung and Water Distribution in the Lung

1.5.1 Structure of the Lung

The respiratory system is divided into upper and lower parts based on their function, the conducting division and the respiratory division. The conducting part consists of all the cavities and structures that transport gases to the respiratory division. Air is conducted through the

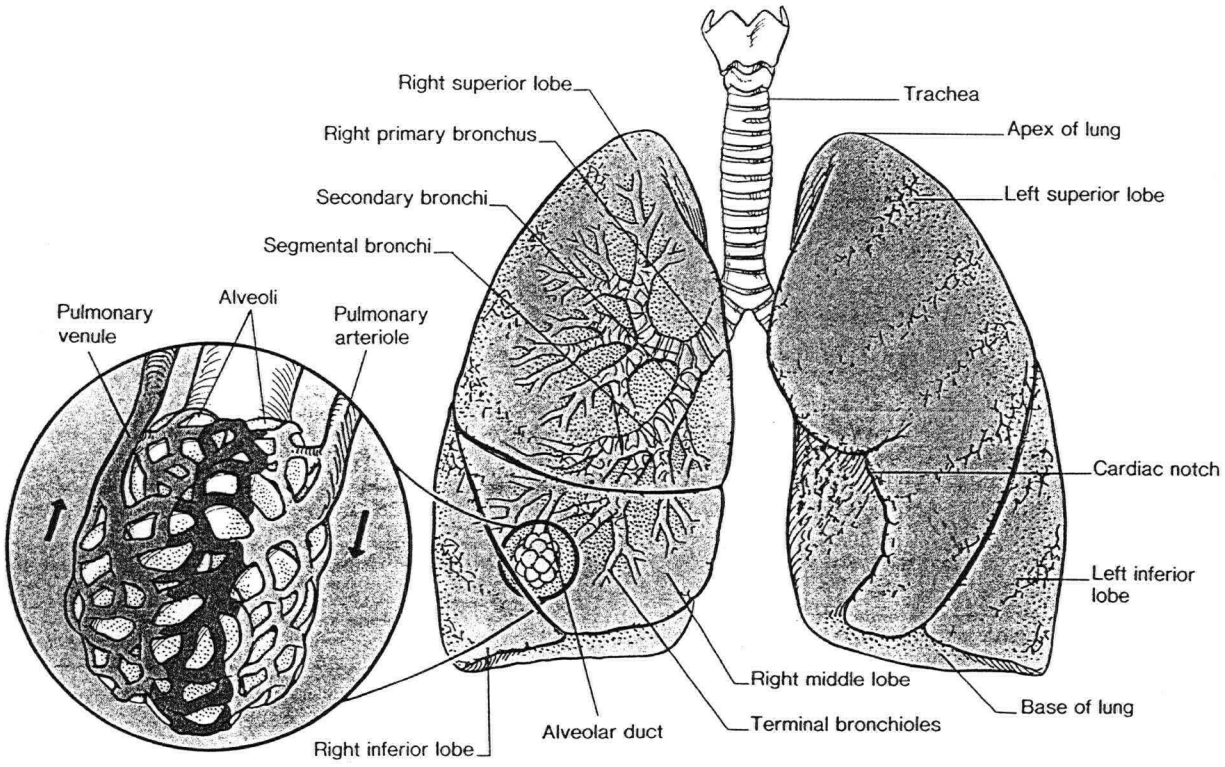

Figure 1.1: An anterior view of the lower respiratory system, showing the bronchial tree, alveoli, and lungs. [Graaff and Fox 1989]

nasal and oral cavities to the pharynx and then through the larynx to the trachea and bronchi. The trachea is a rigid tube connecting the larynx to the bronchial tree. The bronchial tree is so named because it includes a series of respiratory tubules that branch into progressively narrower tubes. The branching begins with primary bronchi and divides in the lungs to form secondary and tertiary bronchi (Fig. 1.1).

The bronchial tree continues yet to branch into smaller tubules called bronchioles. Terminal bronchioles run deep in the lungs to provide the air-conducting pathway (Fig. 1.2). Air from the

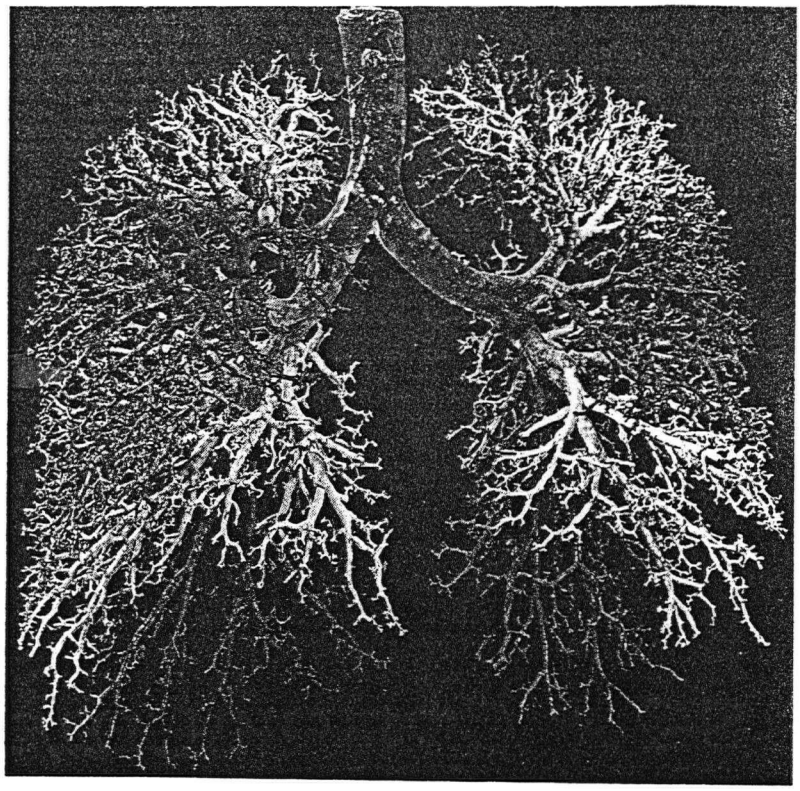

Figure 1.2: A photograph of a plastic cast of the conducting airways from the trachea to the terminal bronchioles. [Graaff and Fox 1989]

terminal bronchioles enters the alveolar ducts which contain individual alveoli as outpouchings along their length. The alveolar ducts terminate with clusters of alveoli named alveolar sacs (Fig. 1.3). The last three structures mentioned constitute the respiratory division.

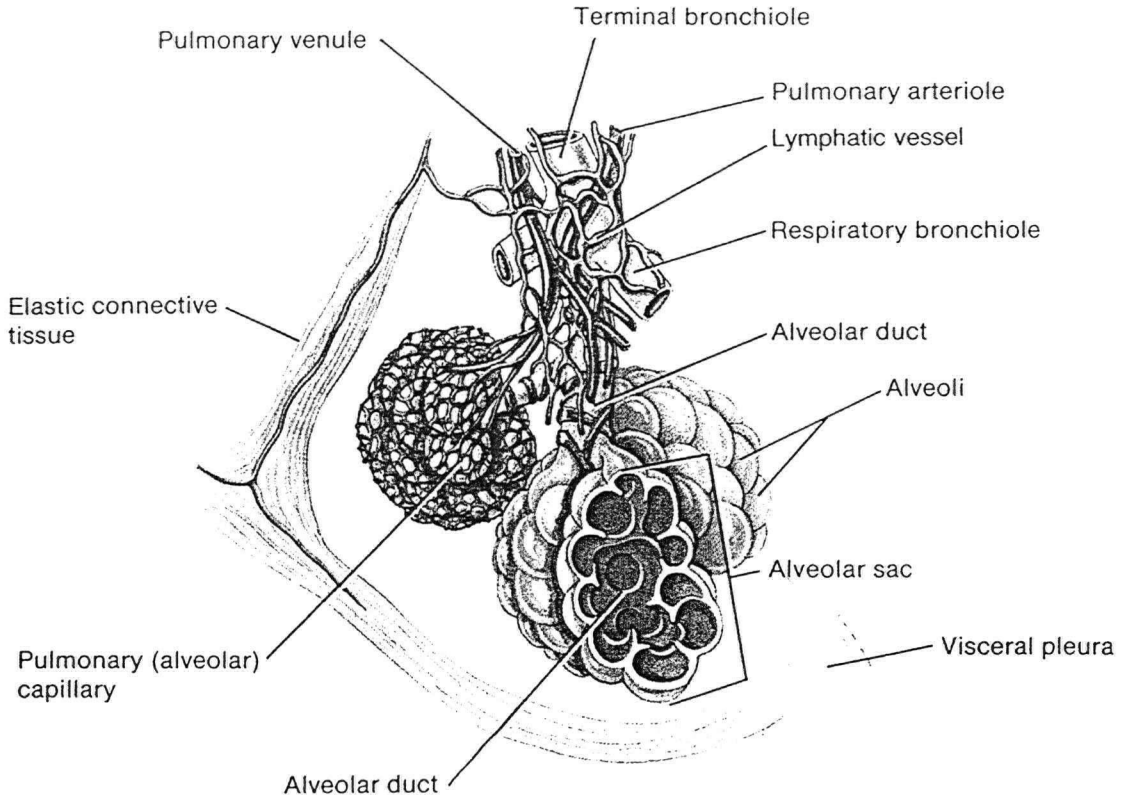

Figure 1.3: A diagram of a portion of a lobule of the lung. The respiratory tubes end in minute alveoli, each of which is surrounded by an extensive capillary network. [Graaff and Fox 1989]

The lungs are paired cone-shaped organs which are large and spongy and located in the

thoracic cavity. The right lung is thicker and broader than the left, weighing more than 700-800 g. The whole lung in an adult has about 700 million alveoli which provide an enormous surface area of about 70 to 100 (m^2). With each inspiration, about 500 ml of air enters the lung. Because of the short diffusion distance (the alveolus is one-cell-layer thick) and the fact that each alveolus is surrounded by so many capillaries, the lung is an ideal machine for the rapid exchange of gases between the air and blood.

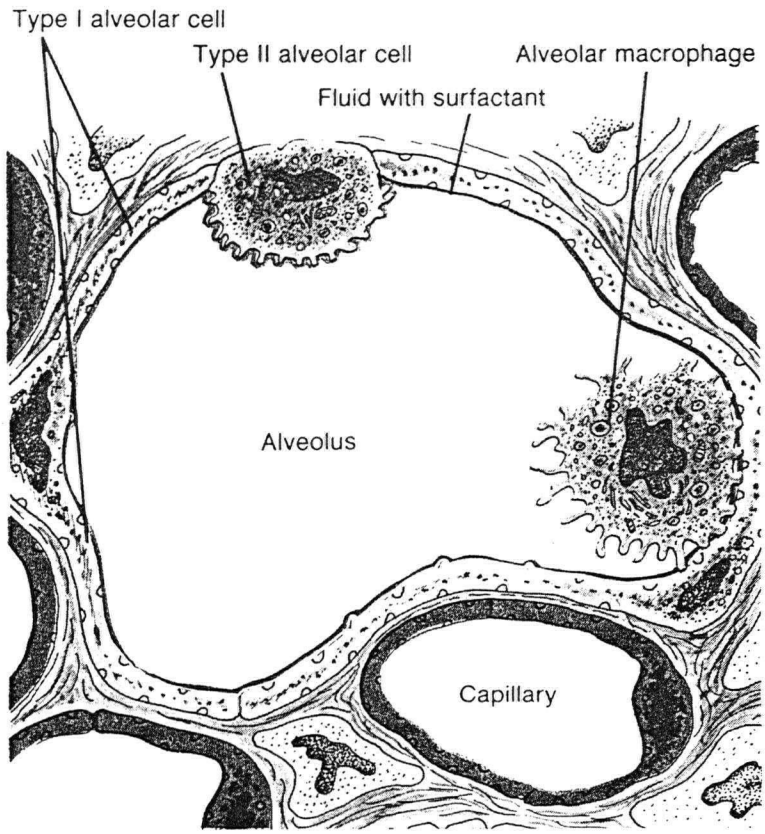

Figure 1.4: A diagram showing the relationship between alveoli and pulmonary capillaries. [Graaff and Fox 1989]

Alveoli are polyhedral in shape and are usually clustered together to form alveolar sacs.

Although the distance between the alveolar ducts and terminal alveoli is about 0.5 mm, alveoli comprise most of the mass of the lungs. Alveoli are cup-shaped outpouchings lined by epithelium and supported by a thin elastic basement membrane. Gas exchange occurs at the walls of alveoli (Fig. 1.4). For this reason, alveoli are the main functional units of the respiratory system.

1.5.2 Biochemical Composition of the Lung

During the past three decades, connective tissue studies of the lung have generated a great deal of interest. The reason for this is that there is no other organ in the body that depends so heavily on the proper architecture and stability of connective tissues to function properly. Biochemically, lung tissue contains collagen, elastin, and "whole cells" suspended in water (see Table. 1.1). Various types of collagens are the major group of proteins in the lung and constitute about 15 to 20 % of dry weight human lung tissue. Collagen is present in all main structures such as airways, blood vessels, and the interstitium of the lung parenchyma. A collagen molecule has a typical rod like structure of about 300 nm in length and 3 nm in diameter. Collagens form a very tightly packed fibril with diameters up to 100 nm [10, 11] and behave as the skeleton for the lung structure to maintain its high tensile strength and rigidity. There are at least eleven different types of collagens which are coded by a group of about twenty genes. Each collagen type includes 3 polypeptide chains intertwined in a right handed triple helix. The individual chains typically contain about 1000 amino acids and all of them have a high content of glycine, proline, and hydroxyproline residues [12].

Several investigators have isolated collagens from the lung and examined their distributions. The most abundant collagens present in the lung are types I and III and they are in a ratio of

Table 1.1: Biochemical Composition of the Lung

Component	Average Dry Weight %	Subcomponent	Average Dry Weight %
Collagen	30		
Elastin	25		
		Lipids	30
Whole cell	45	Proteins	25
		Non-aqueous mobile	45

2:1 [12]. Since there is a tight balance between all the proteins present in connective tissues in the lung, any irregular change in the proportion of collagens can cause disorders of the lung such as pulmonary fibrosis. Also, any large deposits of collagen with the right balance yet the incorrect orientation may drastically impede gas exchange.

Conversely, the presence of elastin provides the lung with an intrinsic elasticity necessary to stretch or constrict whenever required. The elastin content of lungs in different species displays quite a wide range, from 2 to 30 % ; In humans, elastin comprises 28 % of the lung dry weight [13]. Elastin is one of the nature's most non-polar proteins and is composed of almost 33 % glycine, about 12 % proline, and over 40 % of the remaining amino acids contain hydrophobic side chains [14, 15]. The elastin fiber consists of two distinct components: the elastin amorphous and microfibrillar component. The elastin amorphous is the major fraction and comprises 90 % of a mature fiber. The microfibrillar component is mostly displayed in newly synthesized elastin. It has been suggested that microfibrils are primarily secreted into the extracellular matrix to facilitate the path for future elastin deposition [16].

Elastin is certainly one of the most important determining factors in lung elasticity under physiological pressures. The elastin fibers can stretch to 140 % of their resting length compared to collagen which can stretch only to about 2% . Elastin fibers are present everywhere and they are closely associated with collagen and proteoglycans. This remained a perplexing enigma until it was suggested that collagen and elastin encircled respiratory bronchioles and alveolar ducts in a helical fashion [17]. This allows lung tissue to unfold like a door spring to accommodate its increased volume when it expands. Interestingly, the tissue can expand substantially with a very limited increase in the length of elastin fibers. This is a crucial concept since elastin is very closely packed with collagen. Like collagen, any irregular changes in the elastin synthesis and/or the degradation cycle can cause severe illnesses such as emphysema.

The last component present in the lung tissue is what we call "whole cells". For descriptive purposes, a cell can be divided into three principal parts: Plasma membrane, cytoplasm, and nucleus. The plasma membrane is primarily composed of phospholipids and proteins. The cytoplasm is a fluid and jellylike substance in which organelles are suspended. The nucleus is a large spheroid body within the cytoplasm containing the DNA and other genetic materials of the cell such as RNA and proteins.

All the components (collagen, elastin, and whole cells) mentioned above, are suspended in water. It is well known that about 70 to 75% of the body is water, however, the distribution of water in the lung and its compartmentalization is not completely understood.

1.6 Literature on ^{1}H NMR of the Lung

The fundamental approach to heterogeneous systems (i.e. lung) is based upon the measurement of the usual NMR properties such as intensity, frequency, and relaxation behaviour. In general, accurate measurement of NMR properties is contingent upon the characterization of magnetization decay curves. For this reason, it is crucial to determine the relaxation times precisely. NMR studies on the relaxation properties in animal and human tissue were performed by Odelblad *et al.* in the late 1950's [18, 19, 20]. The purpose of early NMR studies was to investigate the ability of NMR measurements to discriminate between normal and malignant tissue and determine the diagnostic capabilities of the approach at the early stages of development [21, 22]. Relaxation measurement studies in lungs were undertaken in early 1972 by Frey *et al.* [23]. In that report, T_1, T_2, and $T_{1\rho}$ relaxation times of non-malignant tissues with tumor were measured in different systems such as heart, lung, and kidney. Subsequently, *in vitro* experiments confirmed that abnormal and/or malignant tissues have significantly longer values of T_1 and $T_{1\rho}$ than corresponding normal tissues [23]. Yet T_2 relaxation times did not show any systematic variation for other tissues such as heart, spleen, and kidney. However, in malignant lung tissue, a slight increase in the T_2 relaxation value was observed.

Generally, T_2 relaxation value has proved to be a sensitive and useful parameter in the lungs. In a study by T. A. Case *et al.* in 1986, it was shown that the FID decay curve from inflated lung (pressure of 20 cm H_2O) was much shorter than in deflated or collapsed lung [24]. This anomalous behaviour was attributed to the local magnetic field inhomogeneity caused by the difference between the diamagnetic susceptibility of air and water at air-tissue interfaces.

In order to explain this observed inhomogeneous broadening in lung, the magnetic field shift was calculated for different models of lung [24, 25]. This calculation established a correlation between the state of inflation and linewidth broadening.

Dependence of lung relaxation times (T_1 and T_2) on the external magnetic field and temperature was investigated by Kveder *et al.* [26]. These measurements were performed on excised and whole lung samples. Their findings indicated the multiexponential nature of the T_2 distribution. In that study, the T_2 measured by Hahn echo and Carr-Purcell-Meiboom-Gill (CPMG) echo train methods showed a two T_2 component decay. One component had a T_2 between 50 to 100 ms and the other component had a very short T_2 value of 1 ms. To investigate the field dependence of the T_2, FID curves from the lung were measured at Larmor frequencies between 29 and 270 MHz. These measurements showed that $(T_2)^{-1}$ and the B field were linearly related to each other. Later work by Kolem *et al.* compared T_2 magnetization decay curves obtained with Hahn and CPMG pulse sequences in excised lung tissue [27]. It was found that the CPMG decay curves had at least four resolvable components ranging from a few ms to 400 ms.

Following these works, more studies [28, 29] were conducted to verify and confirm the results. Also, the multiexponential nature of the T_2 distribution in lung was observed using imaging techniques on small bore imagers [29]. In that investigation, by the same group, it was demonstrated that *in vitro* T_2 relaxation measurements did not significantly differ from those obtained *in vivo* and a two-component T_2 decay curve for normal peripheral lung tissue was obtained. The measured value T_2 components were 9.5 ± 1.0 ms and 34 ± 5 ms for the right lung and 9 ± 1.5 ms and 32 ± 4.5 ms for the left lung.

Alteration in water content is another important property which can characterize acute inflammation and pulmonary edema. To estimate the water content *in vivo*, lung images are needed. However, the main problem is that MR imaging of the lung tissue is difficult. This is for three reasons: 1) low proton density, 2) magnetic susceptibility differences at the air-tissue interface, 3) signal loss due to blood flow (perfusion). Nonetheless, the possibility of measuring the lung-water content from MR images remains quite attractive because of its noninvasive and nondestructive nature. Hayes *et al.* in early 1982 performed *in vitro* MRI measurements on normal and saline-filled lungs and demonstrated a correlation between MR signal intensity and relative lung-water content [30]. That study demonstrated that NMR is capable of determining the lung-water density. Later studies by Ailion *et al.* (in 1984) validated NMR methods for quantitative lung water measurements by comparing the results with those of gravimetric measurements [31, 32]. The best fit to the results was very close to a straight line passing through the origin (with a slope of one) and the coefficient variation (SD as a percentage of mean) of values for the gravimetric and MRI measurements ranged from 13% to 40% and 12% to 30% respectively. These high and large SD's left room for improvements [31].

Subsequent studies of water content measurements essentially tested the reliability and the resolving power of NMR methods as a means of assessing regional and whole lung water distribution. In many cases, a good agreement was obtained between the NMR and gravimetric measurements, however, the uncertainties involved in determining the values were large, up to 30% [33].

Self-diffusion of water in lung is yet another significant parameter which may help to characterize some pathological diseases in the lung. Diffusion measurements in excised rat lung tissue

were initiated by Kevder *et al.* in early 1987 [26, 34]. The pulsed field gradient method was used to perform the measurements and it was found that the apparent diffusion coefficient was smaller than that of free water ($D \approx 2.0 \times 10^{-5} cm^2/s$) by an order of magnitude. Furthermore, their measurements indicated that the diffusion coefficient was time dependent and decreased from $4.0 \times 10^{-6} cm^2/s$ to $3.2 \times 10^{-6} cm^2/s$ in the 45 ms interval time between 5 and 50 ms. Also, the mean square displacement of the spins moving about was proportional to the square root of time. Some explanations were offered to account for this apparent non-Brownian behaviour such as diffusion in the field gradient.

Diffusion studies were also done by Zhong *et al.* in 1991 [35]. Measurements were carried out on excised lung, heart, kidney, and liver tissue, using the pulsed field gradient technique. In that project, the variation of D as a function of diffusion time was related to restricted diffusion and/or diffusion in a field gradient effects. The value of D in lung ranged between $4.6 \times 10^{-6} cm^2/s$ to $0.5 \times 10^{-6} cm^2/s$ as the diffusion time interval changed from 15 to 85 ms.

The diffusion coefficient measurements were revisited by Laicher *et al.* in 1996 [36]. These measurements suggested that the diffusion coefficient was constant with regard to diffusion time. It was proposed that the time dependence of the previous measurements was due to the presence of the internal field gradient and its coupling with the applied field gradient in the PFG method. A previously validated pulse sequence was used to eliminate the effects of the internal gradient and its coupling with the external field gradient [37]. The value of the diffusion coefficient was found to be about $4.0 \times 10^{-6} cm^2/s$) and remained unchanged over a range of time from 18 to 106 ms Also, in the same study it was reported that their recent results, using an Ultra-High Static Field Gradient method ($\sim 0.4 T/cm$) indicated a decrease in

the apparent diffusion coefficient with increasing diffusion time.

1.7 Relaxation

The phenomenon of evolution towards statistical equilibrium of a macroscopic system is referred to as "relaxation" [38]. From the NMR point of view, the whole system includes two weakly coupled parts: the spin system and the lattice. The spin system consists of all degrees of freedom associated with molecular translation and rotation. Nuclear magnetic relaxation is the evolution of the spin system towards thermal equilibrium with the lattice, called spin-lattice relaxation (T_1). Since the lattice temperature is barely affected by the exchange of energy with the spin system taking place during relaxation, it is considered to be an "infinite" bath.

In general, the only physical quantities measured directly in nuclear magnetic resonance are the components of the nuclear polarization (M_x,M_y,M_z). When a static field is applied along the Z axis, the total magnetization is aligned with the magnetic field. If the system is perturbed by a resonant rf pulse, it is no longer in thermal equilibrium. The evolution of M_z towards M_0 modifies the energy of the spin system and corresponds to an exchange of energy with the lattice. On the other hand, the transverse relaxation is a process whereby the nuclear spins come to thermal equilibrium with each other. It is therefore named the spin-spin relaxation(T_2). In fact, transverse magnetization corresponds to a state of phase coherence between the nuclear spin states, meaning that T_2 relaxation is sensitive to interaction terms causing the nuclear spins to dephase and lose coherence. It is worthwhile mentioning that the processes which give rise to T_1 can also affect T_2.

Felix Bloch [39, 40] used a phenomenological approach in which it was assumed that the

evolution of the magnetization towards equilibrium was exponential with two time constants (T_1 and T_2) for the spin-lattice and spin-spin relaxations, respectively. For the spins to exchange energy with the lattice a mechanism is required. In the case of hydrogen, the most prominent interaction responsible for the relaxation is the dipole-dipole coupling. The proton in the nucleus of the hydrogen atom has spin-angular momentum of $I = 1/2$ and possesses an intrinsic magnetic moment. This moment associated with each spin exerts a strong magnetic field on its neighbors. Since the orientation and magnitude of the magnetic field produced by the dipole moment is modulated as a function of time by the molecular motion, the relaxation Hamiltonian averages out to zero in the fast motion regime, $(\omega_0\tau_c)^2 \ll 1$.

To have a better understanding of the relaxation times and the mechanisms involved, consider the Bloch equation:

$$d\vec{M}/dt = \gamma(\vec{M} \times \vec{B}) \tag{1.1}$$

where M is the macroscopic magnetization , and B is the magnetic field, $B = B_0 + b$. In Eqn. 1.1, the vector product can be expanded in terms of the components along the three Cartesian axes. From this, we immediately see that b_x and b_y are effective in both T_1 and T_2 relaxation processes. However, the fluctuation in the b_z is only effective for T_2 relaxation processes. In other words, the T_1 relaxation processes arise only from the fluctuating fields with components in the x and y directions, while T_2 processes arise from components in all three directions. Since b_z is quite close to zero in the rotating frame, there would be zero-frequency contributions to T_2 processes. Therefore, $T_2 \ll T_1$ in the presence of very slow motions and as a result, the significance and effect of these motions is recognized immediately. However, a static component of b in the x or y direction corresponds to a high frequency, meaning that only high frequency

processes can affect T_1 . As one can see the same high frequency processes also affect T_2. These topics are covered in more detail in the next chapter.

1.8 Diffusion

According to the Bloch equation, for a uniform sample, the free induction signal decays exponentially with a constant T_2 time. However, this is true only if the magnetic field was the same at the site of all spins. In practice, the magnetic field always has inhomogeneity and spins experience a distribution of fields. As a result, magnetization undergoes a decay much faster than that due to T_2. The spin echo is capable of refocusing this kind of dispersion, however, it has a limited range of applicability because of the effect of molecular diffusion. Translation of spins from one location to another introduces a temporal variation in the magnetic field experienced by any nucleus because of the heterogeneity present in the lung structure. Since the motion is random and irregular, the temporal variation is not identical at different periods of time. For this reason, the effect of diffusion is dependent upon the spatial magnetic field distribution.

Torrey modified the Bloch equations by using Fick's law to account for the diffusion effect. In that approach, it was assumed that spins would experience a linear magnetic field gradient. However, in lung, the inhomogeneous magnetic fields are induced by spatial variations of the magnetic susceptibility between air-tissue interfaces and can be nonlinear. Besides, the diffusivity of water may be modified by interaction with macromolecules or restricted by the presence of barriers. Thus, the nonlinearity of the magnetic field present in the system combined with the randomness of the molecular motion and the presence of restrictions make the diffusion

measurement and its interpretation difficult.

There have been two rather different approaches to the study of molecular diffusion via NMR techniques. The first method employs the well known Hahn spin echo [41] and the Carr-Purcell-Meiboom-Gill (CPMG) [42] pulse sequence to obtain the diffusion coefficient. The second method employs the pulsed field gradient technique [43]. In this study, the first approach was taken to estimate the apparent diffusion coefficient of water molecules in the lung.

Chapter 2

General Theory

2.1 ^{1}H NMR Theory

2.1.1 Relaxation Theory

Larmor found that the motion of the macroscopic magnetization, which is the vector sum of all the nuclei, in the presence of an applied magnetic field can be explained in terms of the differential equation:

$$\frac{d\vec{M}}{dt} = \gamma(\vec{M} \times \vec{B}). \tag{2.1}$$

This equation is not yet complete since it does not account for, what is called as, "relaxation." There are natural processes which cause nuclei to exchange energy with the lattice and each other. These could be treated as first order processes with characteristic times T_1 and T_2, respectively. Bloch *et al.* [39, 40] incorporated these characteristic times in terms of the phenomenological differential equation described below:

$$\frac{d\vec{M}}{dt} = \gamma(\vec{M} \times \vec{B}) - \frac{M_x}{T_2}\hat{x} - \frac{M_y}{T_2}\hat{Y} + \frac{(M_0 - M_z)}{T_1}\hat{z}. \tag{2.2}$$

Thus the equation of motion for the magnetization consists of two parts: (a) the contribution from the torque exerted by the magnetic field on the vector moment and (b) the contribution from the relaxation processes.

In general, any mechanism which gives rise to fluctuating magnetic fields at a nucleus is a possible relaxation mechanism. In the case of protons (spin 1/2) the magnetic dipole-dipole interaction is the most important and dominant relaxation mechanism. When a nucleus (for example, nucleus 1) is exposed to the magnetic field, it experiences a total field (B_t) which is the sum of two parts: (1) a contribution B_0 from the spectrometer or MRI magnet, and (2) a contribution B_2 from the magnetic moment of nucleus 2. The magnetic field surrounding a magnetic moment is expressed in the form:

$$B_2(r) = \frac{\mu_0}{4\pi r^3}[3(\vec{\mu}_2.\hat{r})\hat{r} - \vec{\mu}_2] \tag{2.3}$$

where $\hat{r}$ is the unit vector in an arbitrary direction in space, μ_0 is the permeability of free space and defined to have precisely the value of $4\pi \times 10^{-7}$ Henry/m. The interaction energy of the moment of nucleus 1 with this magnetic field is the magnetic dipolar interaction between the two moments and is expressed as:

$$E_{12} = -\vec{\mu}_1.\vec{B}_2(r). \tag{2.4}$$

If Eqn. 2.3 is substituted in Eqn. 2.4, the classical interaction energy of the two magnetic moments is obtained

$$E_{12}(r) = -\frac{\mu_0}{4\pi r^3}[3(\vec{\mu}_1.\hat{r})(\vec{\mu}_2.\hat{r}) - \vec{\mu}_1.\vec{\mu}_2]. \tag{2.5}$$

This expression is symmetrical with respect to both moments. The effect of this interaction depends strongly upon whether the vector is fixed in space or changing rapidly because of the relative motion in the nuclei. Considering the Hamiltonian for a two-spin system in a magnetic field B_0 is:

$$\hat{H}_t = \hat{H}_0 + \hat{H}_1. \tag{2.6}$$

where $\hat{H}_0$ is the main static Hamiltonian and $\hat{H}_1$ is the interaction Hamiltonian, in this case, $\hat{H}_1 = \hat{H}_D$ where the subscript D stands for dipolar interaction. Owing to the quantization of the magnetic moment $\mu_s = \gamma_s \hbar I_s$, where γ is called gyromagnetic ratio which has a characteristic value for each nuclear species and $\hbar$ is Plank's constant divided by 2π. The main Hamiltonian

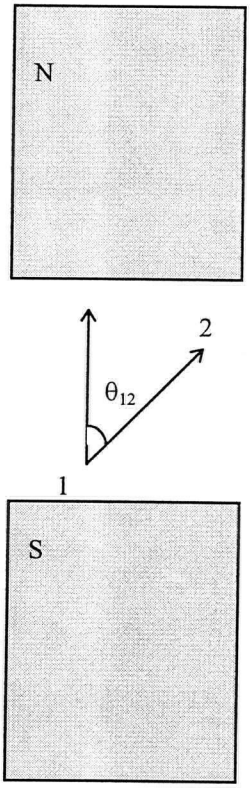

Figure 2.1: Diagram showing the position of the two nuclei 1 and 2 and the angle θ_{12} between their internuclear vector r_{12} and the main magnetic field B_0.

for two spins is given by:

$$\hat{H}_0 = -(\vec{\mu_1} + \vec{\mu_2}).\vec{B}_0 \tag{2.7}$$

$$= -\hbar(\gamma_1 \hat{I}_1 + \gamma_2 \hat{I}_2).\vec{B}_0. \tag{2.8}$$

The expectation values of the operator I are m, hence the expectation values of $\hat{H}_0$, or the energy level of the system is described by:

$$E_M = \gamma \hbar M B_0 \tag{2.9}$$

where $M = m_1 + m_2$.

In order to induce transitions between the energy states, a perturbation of some sort must be introduced. The dipolar Hamiltonian corresponding to the classical energy of two spins is defined as:

$$\hat{H}_D(r) = -\frac{\gamma_1 \gamma_2 \hbar^2}{4\pi r^3}[3(I_1.\hat{r})(\vec{I}_1.\hat{r}) - \vec{I}_1.\vec{I}_2]. \tag{2.10}$$

Let θ and ϕ be the polar coordinates of the vector r and Z axis in the direction of B_0 (see Fig. 1). H_D can be transcribed as

$$\hat{H}_D(r) = \frac{\gamma_1 \gamma_2 \hbar^2}{4\pi r^3}[A + B + C + D + E + F] \tag{2.11}$$

where

$$A = I_{1z} I_{2z}(1 - 3\cos^2\theta) \tag{2.12}$$

$$B = -\frac{1}{4}(I_1^+ I_2^- + I_1^- I_2^+)(1 - 3\cos^2\theta) \tag{2.13}$$

$$C = -\frac{3}{2}(I_1^+ I_{2z} + I_{1z} I_2^+)\sin\theta\cos\theta e^{-i\phi} \tag{2.14}$$

$$D = -\frac{3}{2}(I_1^- I_{2z} + I_{1z} I_2^-)\sin\theta\cos\theta e^{i\phi} \tag{2.15}$$

$$E = -\frac{3}{4}(I_1^+ I_2^+)\sin^2\theta e^{-2i\phi} \tag{2.16}$$

$$F = -\frac{3}{4}(I_1^- I_2^-)\sin^2\theta e^{2i\phi}. \tag{2.17}$$

The energy levels of the first term in the total Hamiltonian ($\hat{H}_t$) are highly degenerate but this degeneracy is lifted by the perturbing Hamiltonian $\hat{H}_D$. However, according to the first-order perturbation theory, only terms which do not induce any change in the value of M contribute in the first order to the splitting of the E_M^0. This leaves only A and B terms which commute with $\hat{H}_0$. Consequently, they are called the secular part of $\hat{H}_D$, resulting in the truncated Hamiltonian which is defined by

$$\hat{H}_D^0 = \frac{1}{2}\frac{\gamma_1\gamma_2\hbar^2}{4\pi r^3}(3(I_{1z}I_{2z} - \vec{I}_1.\vec{I}_2).(1 - 3\cos^2\theta). \tag{2.18}$$

As the molecule (which contains the nuclei) begins to move, the angle θ becomes a time-dependent function. If the motion is rapid enough ($M_2\tau_c^2 \ll 1$) the average value of the local field goes to zero since

$$\int_0^{2\pi}\int_0^{\pi}(1 - 3\cos^2\theta)\sin\theta d\theta d\phi = 0. \tag{2.19}$$

In the above conditional equation M_2 is the second moment of the dipolar broadened lineshape in the absence of motion, and τ_c is the correlation time (the time required for the nuclei to lose phase coherence or memory of an earlier position). Identical spins with a constant separation distance r moving about in space induce a fluctuating local magnetic field. This mechanism causes relaxation and the rates (T_1 and T_2) are described by the Redfield's theory [44]:

$$\frac{1}{T_1} = \frac{\gamma^4\hbar^2}{4r^6}[J(\omega_0) + 4J(2\omega_0)] \tag{2.20}$$

$$\frac{1}{\mathrm{T}_2} = \frac{\gamma^4\hbar^2}{16r^6}[6J(0) + 10J(\omega_0) + 4J(2\omega_0)] \tag{2.21}$$

where ω_0 is the Larmor or resonance frequency and $J(\omega)$ is the spectral density describing the fluctuating part of the Hamiltonian and is the Fourier transform of the correlation function. Correlation functions are defined as:

$$K_i(\tau) = \overline{Y_i(t)Y_i{*}(t+\tau)} \tag{2.22}$$

$$K_i(\tau) = K_i(0)e^{(-|\tau|/\tau_c)} \tag{2.23}$$

where Y_i's are the spherical harmonics and τ_c is the correlation time. Calculating the spectral densities in terms of the above equation, we obtain the relaxation rates in terms of the Larmor frequency (ω_0) and τ_c as defined below:

$$\frac{1}{\mathrm{T}_1} = \frac{3}{10}\frac{\gamma^4\hbar^2}{r^6}\tau_c[\frac{1}{1+\omega_0^2\tau_c^2} + \frac{4}{1+4\omega_0^2\tau_c^2}] \tag{2.24}$$

$$\frac{1}{\mathrm{T}_2} = \frac{3}{20}\frac{\gamma^4\hbar^2}{r^6}\tau_c[3 + \frac{5}{1+\omega_0^2\tau_c^2} + \frac{2}{1+4\omega_0^2\tau_c^2}]. \tag{2.25}$$

As one can see from the above equations, for very short τ_c such that $\omega_0\tau_c \ll 1$, one obtains:

$$\frac{1}{T_1} = \frac{1}{T_2}. \tag{2.26}$$

It is worthwhile mentioning that this theory is valid in the case of a single Poisson process. However, in biological tissues such as lung the correlation functions are quite complex and these equations may not strictly hold.

2.1.2 Translational Diffusion

The phenomenological equations of Bloch give an excellent description of resonance and spin echo. This description assumes explicitly that each moment-bearing nucleus experiences a constant steady field. However, this condition is not rigorously fulfilled in most cases because of the Brownian motion of spins due to their thermal energy. The use of the diffusion equation in conjunction with the Bloch equations was introduced by Torrey [45]. To obtain the equation of motion of spins diffusing in a magnetic field, a simple minded approach will be taken here. In three dimensions, the number density ρ and current density $\vec{J}$ are related through the continuity equation:

$$\frac{\partial \rho}{\partial t} + \nabla . \vec{J} = 0. \tag{2.27}$$

According to the Fick's law, the current density is related to the gradient concentration by $\vec{J} = -D\nabla\rho$ where D is the diffusion coefficient. Substituting this relation in Eqn [2.27] and integrating it over the volume V, we obtain:

$$\int_V \frac{\partial \rho}{\partial t} dv - \int_V (D.\nabla^2 \rho) dv = 0. \tag{2.28}$$

where it has been explicitly assumed that D is a constant. If the integral $\int \rho dv$ is substituted by N (the number of spins in the volume V) and multiplied by the magnetic dipole moment of each spin ($\vec{\mu}$), we obtain the equation of motion for the magnetization of diffusing spins which is:

$$\frac{\partial \vec{M}}{\partial t} = D(\nabla^2 \vec{M}). \tag{2.29}$$

where $\vec{M} = \sum_i < \vec{\mu}_i >$. This term must be added to Eqn [2.2] (Bloch equation). To solve the Bloch equation with the diffusion term added, we will assume a Hahn echo pulse sequence

applied to the sample and the magnetic field is defined as $\vec{B} = (B_0 + \triangle B)\hat{z}$. The analysis is simplest when it is assumed that $\triangle B = \vec{G}.\vec{r}$ where G is a constant field gradient in the z direction. Using the rotating frame of reference, the frequency (ω) reduces to γGz. Disregarding the effect of relaxation, the equation describing the evolution of magnetization in the XY plane is:

$$\frac{\partial M_+}{\partial t} = -i\gamma GzM_+ + D\nabla^2 M_+. \tag{2.30}$$

where M_+ (the transverse magnetization) is a vector precessing about the Z axis. If the effect of diffusion is ignored (D=0), the solution to the equation will be in the form $M_+ = Ae^{-i\gamma Gzt}$. Substituting the M_+ solution in Eqn [2.30] will yield:

$$\frac{dA}{dt} = -D(\gamma G)^2 A. \tag{2.31}$$

This equation assumes explicitly that A is a function of time only. Integrating the above equation with the initial condition of A(0)= 1 will give us:

$$A = e^{-(\gamma G)^2 Dt^3/3}. \tag{2.32}$$

Replacing this expression for A, the M_+ solution will yield:

$$M_+ = M_0 e^{-i\gamma Gzt} e^{-(\gamma G)^2 Dt^3/3}. \tag{2.33}$$

If we incorporate the relaxation effect, it will give us:

$$M_+ = M_0 e^{-t/T_2} e^{-i\gamma Gzt} e^{-(\gamma G)^2 Dt^3/3}. \tag{2.34}$$

which is the solution to the Bloch equation for the magnetization (in the rotating frame) following an initial $\frac{\pi}{2}$ pulse. If we apply a π pulse at time τ, it can be easily shown that the

magnetization at time 2τ will be:

$$M_+ = M_0 e^{-2\tau/T_2} e^{-2(\gamma G)^2 D\tau^3/3}. \tag{2.35}$$

This is Hahn's famous result. If one applies a sequence of n π pulses spaced 2τ apart, one gets

$$M_+ = M_0 e^{-2\tau/T_2} e^{-2n(\gamma G)^2 Dn\tau^3/3}. \tag{2.36}$$

This equation is the basis of the Carr and Purcell technique which was later modified by Meiboom *et al.* to eliminate incomplete refocusing due to the cumulative effects of imperfect π pulses [42]. This equation will be used in later chapters to explain the particular distribution of the lung water density as a function of the geometric mean T_2 and to determine the diffusion coefficient.

2.1.3 Second Moment

Theoretically the various moments of the distribution curve $f(\omega)$ around the resonance frequency are given by Van Vleck's moments definition

$$M_n = \int_0^\infty f(\omega)\omega^n d\omega \tag{2.37}$$

where n is 2, 4, or 6 for M_2, M_4, and M_6 and so on. For a rigid solid, M_{2rigid}, can be exactly calculated from the accurate knowledge of the spatial distribution of protons in a sample and it is defined as (Van Vleck formula):

$$M_2 = \frac{3}{4}\gamma^4\hbar^2 I(I+1)\sum_k \frac{\left(1-3\cos^2\theta_{jk}\right)^2}{r_{jk}^6} \tag{2.38}$$

where the vector $\vec{r}_{jk}$ describes the relative positions of two neighbouring protons, and θ_{jk} is the relative angle between the applied magnetic field and the vector r_{jk}. For a powder made

of crystallites of random orientation $(1-3\cos^2\theta)^2$ can be averaged over all directions, and becomes

$$M_2 = \frac{3}{5}\gamma^4\hbar^2 I(I+1)\sum_k \frac{1}{r_{jk}^6} \tag{2.39}$$

However, for more complex systems we do not have enough knowledge about the distribution of the protons. In this case, the moments can be estimated by expansion of the linshape in terms of moments. An exact expansion for the lineshape in terms of moments can be obtained by using the Lowe-Norberg theorem. This theorem relates the amplitude of the lineshape function $f(\omega)$ to the free induction decay (FID) function F(t). Under general conditions, F(t) and $f(\omega)$ are related by a Fourier transform

$$F(t) = \int_0^\infty f(\omega)\cos(\omega t)d\omega. \tag{2.40}$$

where it is assumed that $\int_0^\infty f(\omega)d\omega = 1$. F(t) can be measured directly in a pulsed NMR experiment, for example, FID curve. If $\cos(\omega t)$ is replaced by its Taylor's series and made use of the definition of M_n we obtain

$$F(t) = \sum_0^\infty (-1)^n \frac{t^{2n}}{(2n)!} M_{2n}. \tag{2.41}$$

Chapter 3

Experimental Techniques

3.1 NMR and MRI Measurements

3.1.1 Samples

For the NMR measurements, twenty-one samples (of volume about 1 cm^3) of deflated peripheral lung were excised from four different normal juvenile pigs. The pigs had been euthanized with a sodium pentabarbitol overdose then exsanguinated passively by cutting the abdominal aorta before the lung excision. To minimize the susceptibility-induced magnetic field gradients, samples were chosen from parenchymal regions with no airways or blood vessels. The lung samples were sealed in sample tubes of 1 cm diameter. The animal experimental protocol was approved by the institutional ethics review board.

MRI measurements were performed on nineteen lungs from healthy juvenile pigs. The same procedure, as mentioned above, was taken to sacrifice the pigs and prepare the lungs. Ten single lung-water-content measurements were acquired with a quadrature birdcage head coil to ensure higher S/N ratio. The rest of the measurements were performed with the body coil to more closely replicate the human *in vivo* situation.

To partly simulate the *in vivo* conditions of lung, the trachea was intubated and the lungs were kept inflated with oxygen at an inflation pressure of 10 cm H_2O during the course of the

experiment. The lung volume remained constant throughout the imaging period. The lungs were placed in trays and covered with plastic wrap to prevent water loss. Two water phantoms doped with $MnCl_2$ were placed next to the lungs for reference. For one lung sample, MR measurements were acquired before inflation to investigate the effect of inflation on T_2 times.

Lung MRI measurements were also carried out on two live juvenile pig. Gating to the cardiac cycle was achieved by using the signal from a pressure transducer inserted into the carotid artery to trigger the MRI scanner. A respiratory bellows was used to monitor the pig respiratory cycle.

3.1.2 Hydroxyproline

To determine tissue collagen content, the collagen-specific amino acid hydroxyproline was assayed in 15 samples [46]. This experimental procedure was developed by Stegeman *et al.* [48]. Tissue samples were placed in tubes with 2 ml of 6 M HCl and were bubbled with 100% nitrogen gas for 30 seconds prior to sealing the samples to ensure the removal of oxygen, as much as possible. Then samples were heated at 105°C. for 16 hours. Since hydrolysis generates considerable browning, 5-10 mg charcoal was added to each tube. The charcoal was spun down using a bench-top centrifuge at 3500 rpm for 15 minutes.

A clear aliquot of the sample was evaporated to dryness in a desiccator over NaOH; this process usually took 24 hours. Then the sample was mixed with 2 reagents and placed in a hot bath tub at 60° C for 15 minutes. The first reagent was a solustion of chloramine T dissolved in water and propanol and PH 6 buffer and the other reagent was a aldehyde perchloric acid. The samples were then cooled and their absorptions at 550 nm were read. The absorption

values were compared with a series of hypro standards (purified type I collagen) with different concentrations of hydroxyproline ranging from 10 to 200 $\mu g/ml$. The hydroxyproline value for each sample was converted to collagen content based on an average collagen content of 1/7 hydroxyproline by weight.

3.1.3 NMR and MRI Equipment

Proton NMR measurements were carried out on a modified Bruker SXP 4-100 operating at 90 MHz with an $11\mu s$. receiver dead time. Data acquisition and analysis were carried out on a system which includes a locally built pulse programmer [47], a Rapid Systems digitizer, and an IBM compatible computer. The ^{1}H NMR spectra measurements were performed on a 300 MHz Varian XL-300 spectrometer. All the experiments were done at 24° C.

In this study, MRI measurements were carried out on a 1.5T GE Signa MRI scanner (General Electric Medical Systems, Milwaukee, 5.4 level). Following a localizer scan, the lungs were imaged using a single slice multi-echo pulse sequence to produce an accurate T_2 decay curve for lung tissue and the water standard.

3.1.4 NMR Pulse Sequence Techniques

A modified version of the free induction decay (FID) pulse sequence was used to determine the water content and measure the moments. This pulse sequence was applied to distinguish the fast decaying non-aqueous signal from the water and mobile non-aqueous signal. The pulse sequence represented by:

$$90^\circ_0 - \frac{\tau}{2} - (180^\circ_{90} - \tau)_n \tag{3.1}$$

where $n = 8$, $\tau = 200\mu s$, and the repetition time was 10 s. The subscripts indicate phase shift of the pulses relative to the reference signal. The 180° pulses were applied to refocus phase dispersion in the mobile signal due to the magnetic field inhomogeneity. Strictly speaking, there is no difference between this pulse sequence and the CPMG echo train except the value of n is very small. The duration of the 90^0 pulse ranged from 1.8 to 2.2 μs.

The Carr-Purcell-Meiboom-Gill (CPMG) pulse train was applied to each sample to acquire the T_2 decay curve. The sequence is represented by

$$90^\circ_0 - \frac{\tau}{2} - (180^\circ_{90} - \tau)_n \tag{3.2}$$

where ($n = 4230$). A recycle time (TR) of 10 s after acquisition allowed re-equilibration of magnetization. 250 to 2500 scans were accumulated for the wet and fully dehydrated samples respectively. The sequence was repeated with $\tau = 100$, 200, 400, 600 μs in order to investigate the dependence of the decay curve upon echo spacing. To determine the T_2 distribution, four points per echo were averaged and 736 echo amplitudes collected from the echo train to obtain the transverse magnetization decay curves. These curves could be represented by the sum of several components,

$$S(t) = \sum_{i=1}^{m} S_i e^{-t/T_{2(i)}} \tag{3.3}$$

where S_i is the relative magnetization of each component (proportional to the number of protons) and T_{2i} are the corresponding ith component of the relaxation times.

A modified version of the Inversion Recovery pulse sequence was employed, represented by

$$90^\circ_x - TR \tag{3.4}$$

$$180_x^\circ - \tau - 90_x^\circ - TR \tag{3.5}$$

where the second signal was subtracted from the first to give a positive signal decaying to zero at long τ. The recycle time TR of 10 s was selected for the wet samples. Thirty τ values (the range over which τ varied depended on T_1) were chosen in a geometric fashion from $500\mu s$ to 5s.

3.1.5 MRI Pulse Sequence Techniques

To measure the water content and determine the T_2 distribution of the lungs by MRI, a single slice 16 echo pulse sequence was employed to acquire images. This sequence employed a slice selective 90^0 pulse followed by rectangular composite 180^0 pulses. The composite pulses were flanked by a series of gradient crusher pulses of alternating sign and decreasing amplitude designed to eliminate artificial contributions from stimulated echoes [50]. The sequence parameters were TR 2000 ms, echo spacing 10 ms, FOV 32 cm, bandwidth $\pm$32 kHz and the entire lung was imaged successively in 1 cm thick slices. The sequence produced 16 images per slice with TE times ranging from 10 ms to 160 ms in 10 ms steps.

For the *in vivo* measurement, the multi-echo sequence was run on a single axial slice. The cardiac gated *in vivo* sequence was initiated 250 ms after the pressure wave peak obtained with a catheter in the carotid artery. This timing corresponded to diastole in the cardiac cycle. Three or four pressure wave peaks were then skipped before initiation of the next repetition to produce a cardiac synchronized repetition time longer than 2 seconds. Respiratory artifacts were reduced by using a Respiratory Compensation algorithm (General Electric Medical Systems).

To estimate T_1 relaxation times for the *in vitro* lungs and water standards, a partial saturation spin echo sequence was applied to a single central lung slice with 8 TR times of 50, 100, 200, 400, 800, 1200, 2000, and 4000 ms, with a constant echo delay (TE=17 ms).

3.1.6 Dehydration

Following NMR measurements, all samples were weighed and dried under vacuum at 55^0 C to a constant weight in order to obtain their gravimetric weight. One additional sample was dehydrated incrementally by allowing evaporation of water under vacuum at room temperature. At each step, lung weight measurements were performed using an accurate balance (Sartorrius 2462) with sensitivity of 0.1 mg. Finally, the samples were completely dried under vacuum at 55 °C to a constant weight.

For MRI measurements, all samples were weighed right after the experiment and cut into smaller pieces to allow more surface for evaporation. To attain the gravimetric water content of each lung, the same procedure (mentioned above) was followed. Four lungs were dehydrated incrementally by allowing evaporation of water at room temperature under very light pumping to prevent excessive expansion and damaging of the lungs. At each step, after weighing the sample, MRI measurements of the water content and T_2 distribution were performed.

3.1.7 Non-Negative Least Squares (NNLS) Analysis of Relaxation

T_1 and T_2 relaxation curves were analyzed using a non-negative least squares algorithm [51]. This method requires no *a priori* assumptions about the number of exponential components and amplitudes (m), However, a large number of relaxation times must be specified. A basic

equation describing the relaxation of magnetization in an NMR experiment is

$$y(t_i) = y_i = \int_{T_{min}}^{T_{max}} s(T) e^{-t_i/T} dT \tag{3.6}$$

where the N decay-curve data y_i are measured at times t_i, s(T) is the unknown distribution amplitude as a function of the relaxation time T. One of the simplest and fastest ways to prepare Eqn. [3.6] for computer implementation is to assume that the spectrum is a sum of m δ functions with positive s_j at relaxation times T_j. That means

$$s(T) = \sum_{j=1}^{m} s_j \delta(T - T_j). \tag{3.7}$$

Typically m is selected between 100 to 200 therefore not restricting the solution to a specific number of relaxation times. Substituting Eqn [3.7] in Eqn [3.6], we obtain:

$$S(t) = \sum_{i=1}^{m} S_i \, e^{-t/T_{2i}} \tag{3.8}$$

where S_i is the relative magnetization of a component, proportional to the number of protons, and T_{2i} is the component of the relaxation time. All decay curves can be represented by the sum of m components. The NNLS algorithm designates non-zero amplitudes to a few of these T_2 times in order to minimize the χ^2 misfit as defined by the following equation

$$\chi^2 = \sum_{i=1}^{N} (y_i - y_i^p)^2 / \sigma_i^2. \tag{3.9}$$

where y_i^p are the data corresponding to the constructed spectrum and σ_i is the standard deviation associated with the measured data y_i. The preferred model has a value of $\chi^2 \approx N$ and its SD is $\sigma = (2N)^{1/2}$. If $\chi^2 \gg N$, the data are poorly fit and information about the true T_2 distribution is lost. Alternatively, if $\chi^2 \ll N$, the data are fit too accurately and an artifact of the noise is evident on the fit.

Smooth or continuous distributions of relaxation times were generated by incorporating extra constraints. A general form is to minimize $\chi^2 + \mu A$, where A is the sum of squares of the amplitudes of the solution and μ is the regularization parameter ($\mu > 0$). χ^2 is increased by 1 to 3% above its minimum by increasing μ.

3.1.8 NMR and MRI Relaxation Analyses

Using the CPMG technique, the transverse magnetization curves obtained from the excised lung tissues were analyzed by the NNLS method to determine T_2 distributions— for detailed information see chapter 5. MRI T_2 magnetization decay curves were derived from region of interest measurements on the same volume on all sixteen echoes from the multi-echo sequence. T_1 and T_2 relaxation times for deflated, inflated and *in vivo* lungs were derived from the decay curves using the non-negative least squares algorithm (NNLS). All the T_2 analyses were performed on body coil measurements.

Global characterization of the T_2 distribution was done by selecting the whole lung image as a voxel of interest (VOI). A decay curve was obtained from each voxel and it was analyzed as explained earlier. The geometric mean T_2 was calculated from the same decay curves. This topic will be discussed in greater detail in chapter 7 and 8.

Chapter 4

The Second Moment Measurements and Its Correlation With Water Content

4.1 Introduction

The proton magnetic resonance signal from lung tissue is quite complex, arising from distinct water compartments and different molecular constituents. A typical deflated excised lung sample consists of collagen, elastin, and "whole cells" in water. Whole cells, in turn, have an intricate composition consisting of lipids, membrane proteins, cytoplasmic proteins, and metabolites (Table 2) [50]. The interpretation of the ^{1}H NMR signal from lung is complicated by a number of factors including magnetic susceptibility variation [51], dipolar line broadening [51, 52], diffusion [28, 53], heterogeneity [28, 54], and paramagnetic solutes. Nevertheless, several types of useful information are available from the ^{1}H NMR signal.

The free induction decay signal from a lung tissue contains a rapidly decaying component (named motionally restricted) which lasts a few 10's of μs. The focus of this chapter is on the NMR properties of the motionally restricted component and its contribution to the transverse magnetization decay curve.

4.2 Materials and Methods

4.2.1 Samples and NMR Apparatus

The second moment measurements were performed on twenty-one-deflated excised samples of peripheral lung (see chapter 3). Following NMR measurements, the collagen content of 15 samples was determined. In addition, two blood samples were prepared for NMR measurements. ^{1}H NMR measurements on the lung were carried out with the solid state NMR spectrometer (see chapter 3) which had both a high signal-to-noise ratio (S/N), and a short dead time ($\approx 10\mu s$). These characteristics made it sensitive to the complete proton signal from the lung tissue.

4.2.2 Free Induction Decay Measurements

The modified version of the free induction decay (FID) pulse sequence (see chapter 3) was used to measure the moments and determine the Wet/Dry ratios. The total ^{1}H NMR signal of a typical lung tissue consists of a fast decaying component, lasting approximately 30 to 50 μs, and a slower decaying part which persists over 10 ms or longer (Fig. 4.1). The latter signal arises from water and mobile protons associated with cytoplasmic proteins and metabolites which undergo rapid isotropic motion, averaging dipolar interactions to zero [50]. The rapidly decaying component can be characterized by the second moment of its lineshape which provides us with insight into the dynamic structure of the solid component of lung [55, 56].

Since the lung tissue is composed of two major components, namely the motionally restricted and mobile components, the expansion of the FID function in terms of moments was changed slightly to accommodate the complexity of the system (see Eqn [2.40]). The fast decaying

signal, from dipolar-coupled protons of the sample, was fit to a moment expansion equation of the form

$$S(t) = (S_0 - L_0)(1 - M_2\frac{t^2}{2!} + M_4\frac{t^4}{4!} - M_6\frac{t^6}{6!}) + L_0 \tag{4.1}$$

where M_2, M_4, and M_6 are the second, fourth, and sixth moments of the total proton lineshape, respectively [57]. S_0 and L_0 are the signal intercepts at zero time from the total and mobile signals respectively. In this calculation, it was assumed that the mobile signal, L_0, was constant over the duration of the motionally restricted signal. S_0 and the three spectral moments were estimated by fitting Eqn [1] to sixteen to twenty FID points between approximately 12 to 32 μs using a non linear functional optimization program to minimize χ^2 [58].

The mobile signal is characterized by its T_1 and T_2 relaxation times which relate to the microscopic tissue environment. Eight points per echo were averaged to make up a mobile signal T_2 decay curve which was fit by a simple monoexponential fitting algorithm to estimate the constant, L_0. The spectral moments (obtained above) relate to the total NMR signal. To get the second moment for the motionally restricted component alone, the value from Eqn [4.1] was divided by $(S_0 - L_0)/L_0$ in order to remove the contribution from the mobile signal which was assumed to possess zero M_2.

4.3 Results and Discussion

4.3.1 FID and Moment Measurements

A typical FID from a lung sample is shown in Fig. 4.1. The 180^0 pulses were required in order to refocus phase dispersion due to magnetic field inhomogeneity. The simplest way to

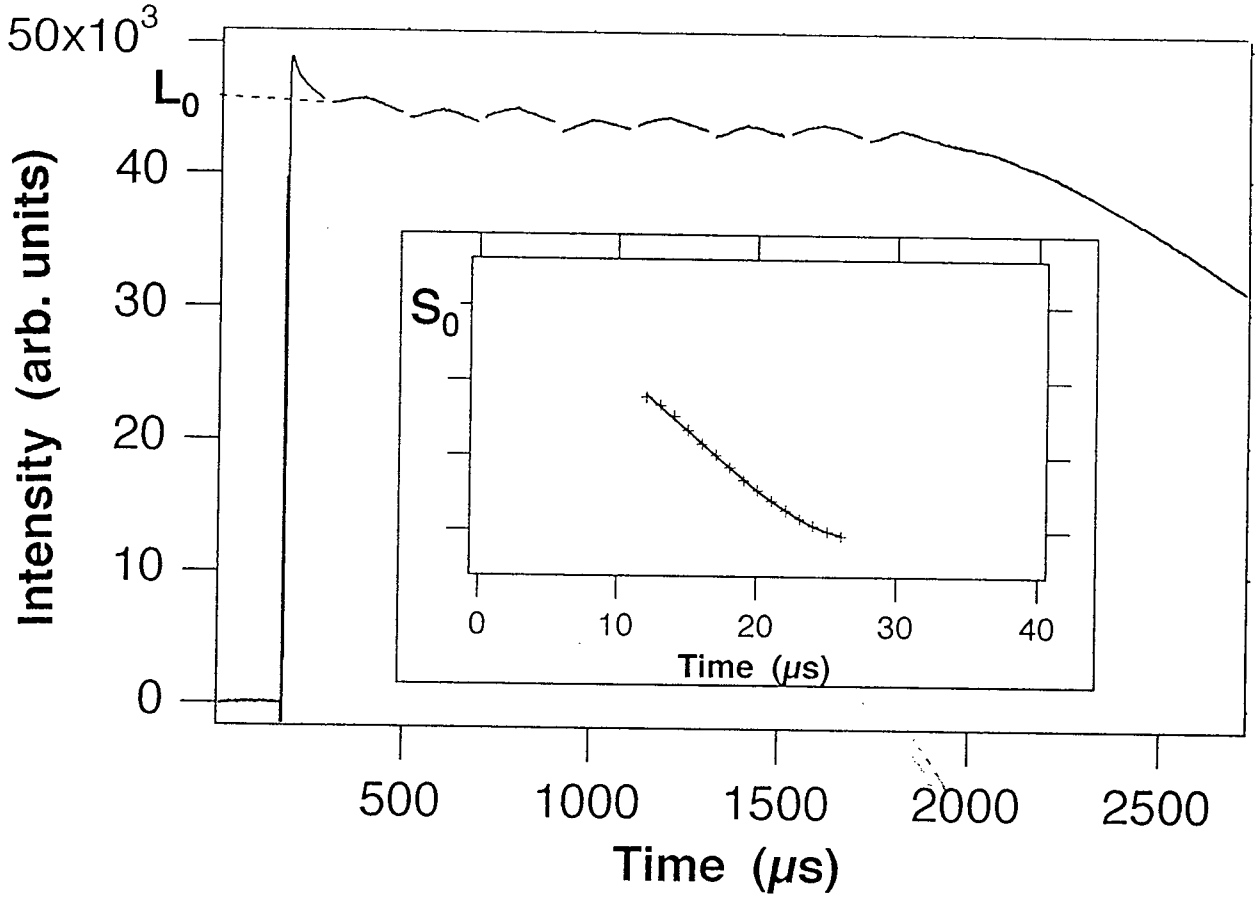

Figure 4.1: A typical free-induction-decay curve from a lung sample. The gaps indicate the applied 180^0 pulses, τ= 200 μs. The insert is the motionally restricted component fitted by the moment expansion.

obtain quantitative information from the broad-line NMR signal received from the non-aqueous component of lung tissue is the method of moments. The most important moment for structural studies is the second moment. To determine the moments, the fast decaying part of the signal, which has a shape determined by dipolar broadening, was fit to Eqn. [4.1] as shown in the inset of Fig. 4.1. The average M_2 value for the wet samples was about $3.42 \pm (0.25) \times 10^9 s^{-2}$. This value is similar to that obtained from other biological samples, *e.g.* , Rhodopsin [56].

Due to the presence of motion which is rapid on the proton NMR timescale, ${M_2}^{-1/2} \approx 10\mu s$, the measured second moment is generally less than the rigid lattice second moment. In the limiting case of rapid isotropic motion on the NMR timescale, the measured second moment approaches zero. For the complex heterogeneous structure of the lung, it is not reasonable to estimate the rigid lattice M_2 value. However, we know that it must be substantially smaller than that for a hydrocarbon chain of methylene (CH_2) groups ($\approx 2 \times 10^{10} s^{-2}$) [55] but likely larger than that estimated for long chain polysaccharides such as cellulose ($\approx 7 \times 10^9 s^{-2}$) [17]. The measured average M_2 value for lung tissue of $3.42 \pm (0.25) \times 10^9 s^{-2}$ therefore is probably about 1/3 the rigid lattice value. This implies that the long macromolecules undergo considerable anisotropic motion on the NMR timescale. M_2 values measured for lung are not appreciably different from that measured in other biological systems such as membranes [55].

To monitor the evolution of the second moment as a function of hydration level, one sample was dehydrated incrementally by allowing evaporation of water under vacuum at room temperature. Figure 4.2 depicts M_2 as a function of the hydration level. As water was removed, the orientational order (M_2) of the motionally restricted function remained constant from wet/dry level of 6 to 3. It then increased by a factor of two for a hydration level of 3 and lower. This

indicated a substantial reduction in molecular motion upon dehydration.

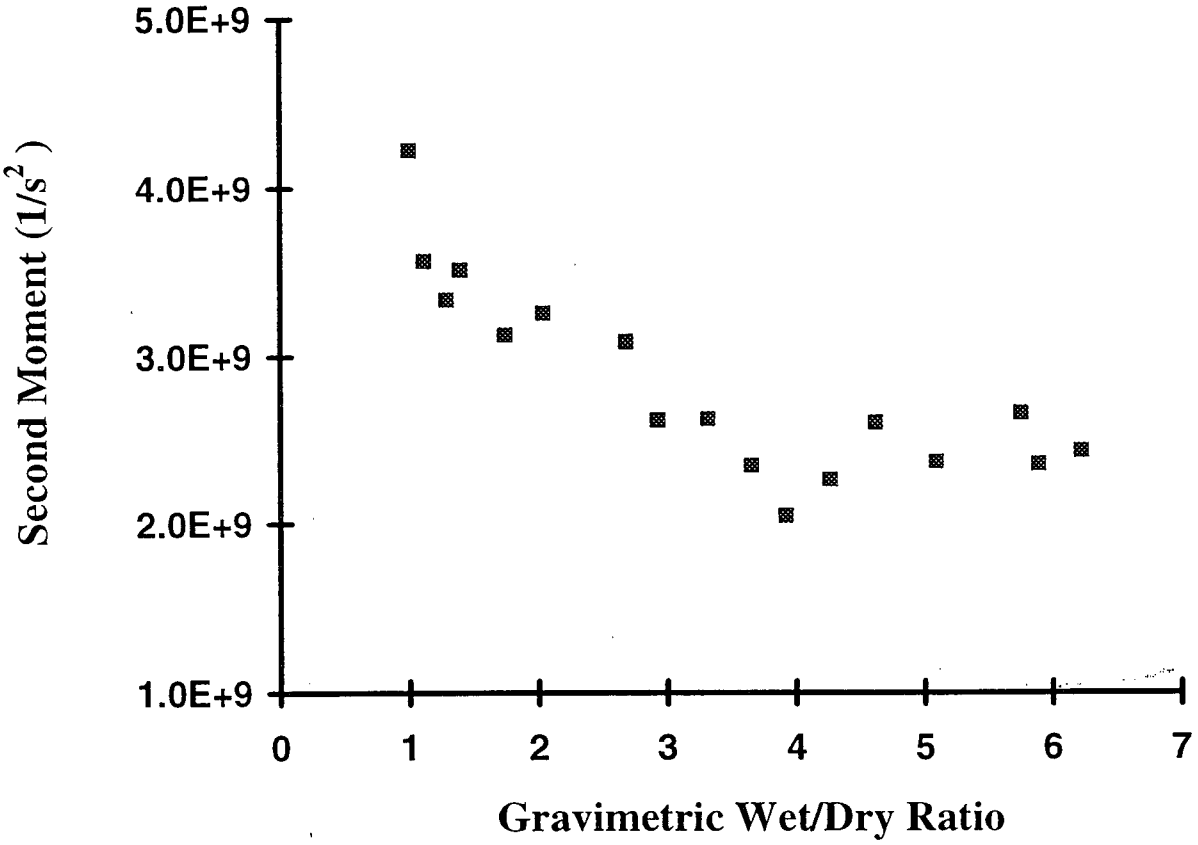

Figure 4.2: The second moment plotted as a function of wet/dry ratio for one of the lung samples. A two fold increase was observed as the sample was dehydrated.

4.3.2 Collagen Assay

Hydroxyproline assay experiments were performed in order to determine the collagen content of each individual sample; the collagen content of the peripheral lung tissue samples ranged from 13% to 41% of the dry weight. Figure 4.3 shows a histogram of the collagen content of the samples.

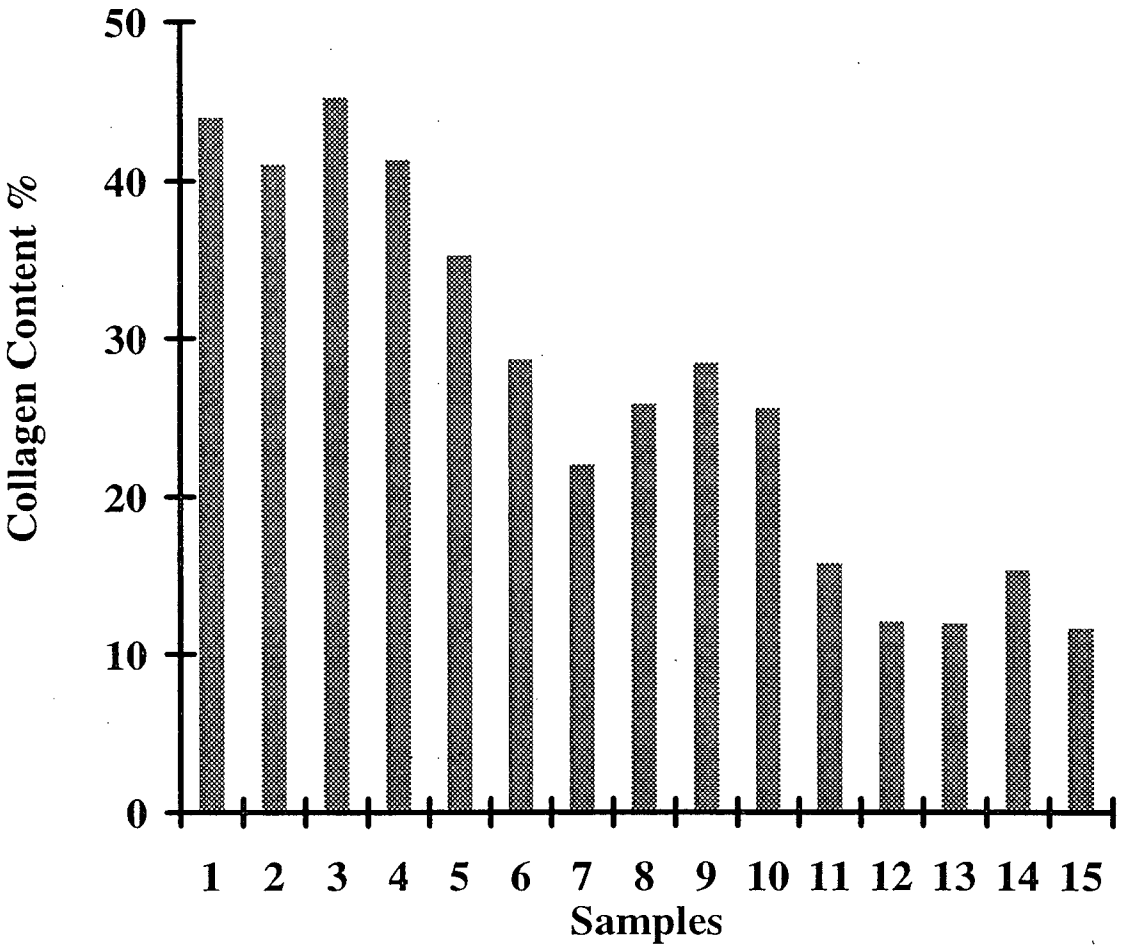

Figure 4.3: The histogram of collagen content in 15 lung samples.

Collagen is one of the major proteins present in most of the structures. Collagen molecules have rod like structures and they form tight fibrils. This property of collagen prevents the lung from collapsing. The high tensile strength and rigidity of collagen made it a very good candidate for examining the correlation between the second moment and collagen content of each sample.

However, no significant correlation ($R^2 = 0.44$) was established between the M_2 and collagen

content of each sample. This indicated that the effect and contribution of collagen in determination of dynamics of lung tissue cannot be considered independently of the other chemical constituents .

4.3.3 The Effect of Blood on M_2 Measurements

Second moment measurements were performed on samples in which the residual blood was minimal. However, to ensure the fast decaying component was associated only with the lung tissue, and that blood had no effects on M_2 values, the same FID measurements were performed on 2 blood samples. Blood is composed of a cellular portion (named formed element) and a fluid portion, called plasma. The formed element constitutes 45 % of the total blood volume and the plasma accounts for the remaining 55 % . The formed elements of blood includes two types of blood cells: erythrocytes or red blood cells, and leukocytes or white blood cells. Erythrocytes are by far the most numerous of these two types; a cubic millimeter of blood contains 5.1 to 5.8 million erythrocytes in males and about a million less in females. Since erythrocytes are relatively big (7 μm in diameter and 2.2 μm thick) it seemed worthwhile to explore their contribution to NMR properties, including motionally restricted signal intensities (M_2).

Since the rate of tumbling for the red blood cell is low, it, in principle, gives rise to a rapidly decaying magnetization curve. However, it may be shown that the anticipated fast decaying FID is about 1% of the total signal due to the low concentration of erythrocytes. Figure 4.4 shows an FID curve from a typical blood sample. Clearly, blood did not make any substantial contribution to the fast decaying component and consequently had no effect on M_2 values.

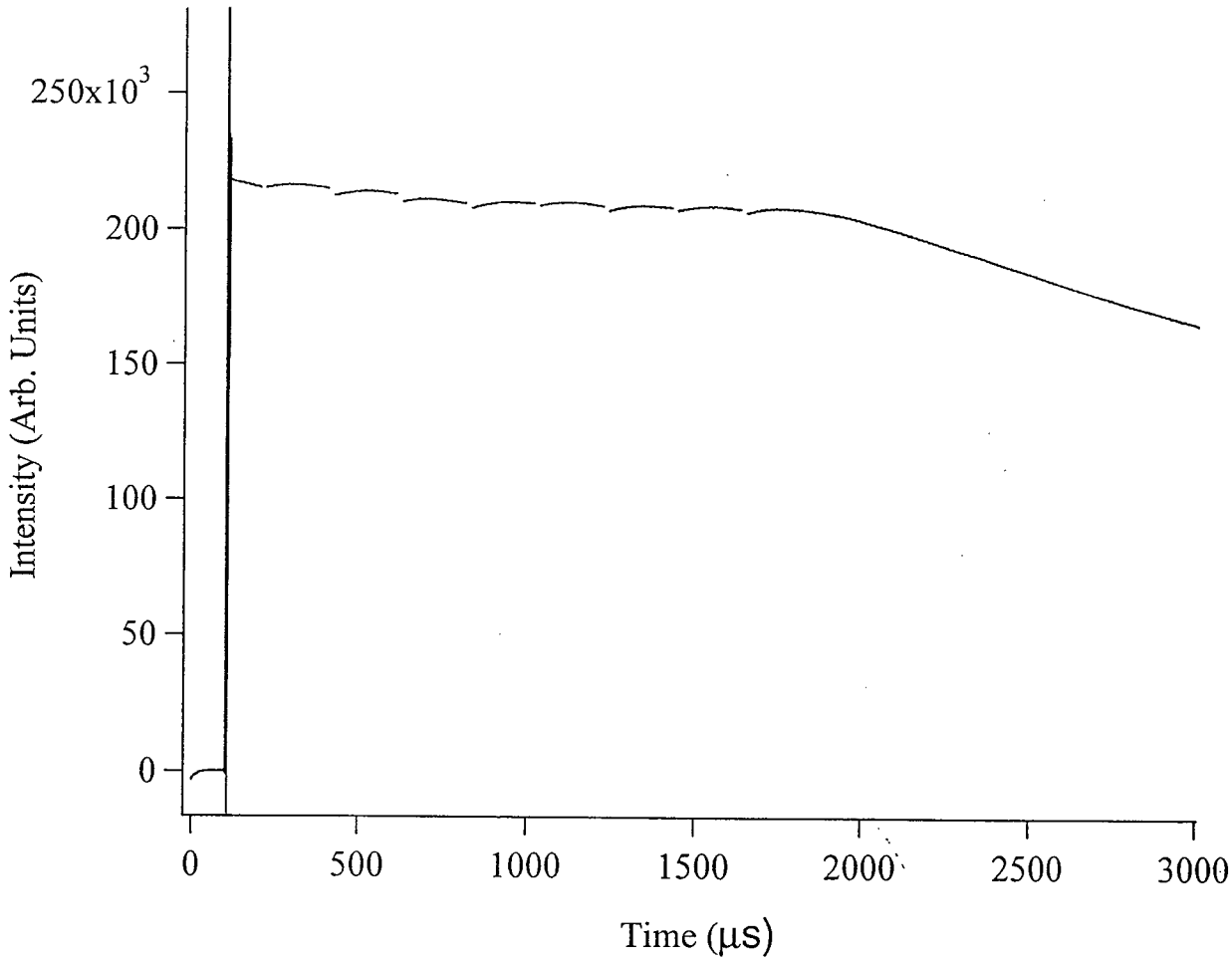

Figure 4.4: The free-induction-decay curve from a blood sample. No motionally restricted component was observed, $\tau = 200\mu s$.

Chapter 5

NMR Measurements of Water Content and Relaxation Distributions

5.1 Introduction

As mentioned earlier, (see chapter 2) chronic infiltrative and cardiopulmonary diseases are characterized by an increase in lung water content. For this reason, many studies have been conducted on the determination of water content both *in vivo* and *in vitro* [59, 60, 61, 62, 33, 14, 15]. Since the NMR signal can provide a direct measure of lung tissue water, MRI is a good method for investigation of inflammatory and degenerative diseases [63, 64].

Two significant NMR properties of many tissues including lung are spin-spin (T_2) and spin-lattice (T_1) relaxations which are measured by the CPMG and Inversion Recovery pulse sequences, respectively [42, 65]. In the lung or any biological tissue, protons exist in a variety of different environments giving rise to a wide range of relaxation times. Therefore, the measured decay curve is a sum of contributions from all spins which may have sampled different environments during the course of the experiment. As a result, these measurements should enable us to get information on the water distribution and tissue pathology. Previous studies have demonstrated that pulmonary injury can be characterized by changes in the tissue's relaxation times, T_1 and T_2 [66, 67, 68, 69, 29]. The latter, T_2, has been shown to be a more sensitive and useful parameter for pulmonary edema than T_1 [34, 63, 70].

A large number of diagnostic changes in lung tissue are characterized by alteration in the Wet/Dry ratio. The relative signals from water and non-aqueous tissue may be used to estimate the Wet/Dry ratio of the lung samples. In the absence of T_1 and T_2 weighting, the NMR signal intensities are proportional to the number of contributing protons. Therefore, to estimate Wet/Dry ratios from the free induction decay, we require values for the hydrogen content per unit mass for lung tissue and for water. Two methods were employed to estimate lung proton density: 1) a calculation based upon chemical content and 2) a measurement based upon the NMR signal from a lung sample dehydrated incrementally. For partial chemical characterization, the collagen content of several of the lung samples was obtained by hydroxyproline analysis.

5.2 Material and Methods

5.2.1 Samples and NMR Equipment

The same twenty-one deflated excised samples with their volume about one cm^3 (as in chapter 3) were used for the water content measurements. The collagen contents of 15 samples were determined, applying the hydroxyproline assay. The solid state ^1H NMR spectrometer (operating at 90 MHz) was employed to carry out NMR measurements. The ^1H NMR spectra measurements were performed on a 300 MHz Varian XL-300 spectrometer. All the experiments were done at 24^0 C.

5.2.2 NMR Water Content Measurements

The modified version of the free induction decay (FID) pulse sequence (defined in chapter 3) was used to determine the Wet/Dry ratios. This pulse sequence was employed to distinguish the fast decaying non-aqueous signal from the water and mobile non-aqueous signal. S_0 was estimated by fitting Eqn [4.1] to twenty FID points between approximately 12 to 32 μs using a non linear functional optimization program to minimize χ^2. Eight points per echo were averaged to make up a mobile signal T_2 decay curve which was fit by a simple monoexponential fitting algorithm to estimate the constant, L_0.

5.2.3 Relaxation Measurements

To acquire the T_2 decay curve, the Carr-Purcell-Meiboom-Gill (CPMG) pulse train was applied to each sample. The CPMG pulse sequence contained 4230 echoes of which 736 were chosen to obtain the transverse decay curve. Four points per echo were averaged to form the amplitude of each echo. To examine the dependence of the decay curve upon echo spacing, different τ values ranging from 100 μs to 600 μs were used. CPMG decay curves were represented by the sum of m components,

$$S(t) = \sum_{i=1}^{m} S_i \, e^{-t/T_{2i}} \tag{5.1}$$

where S_i is the relative magnetization of a component, proportional to the number of protons, and T_{2i} is the component of the relaxation time. Since the NNLS method requires no *a priori* assumption about the number of components T_{2i}, one hundred fifty geometrically spaced relaxation times from 0.01 to 5s were specified for spin-spin relaxation and 150 linearly scaled T_1 times from 0.01 to 10 s were used for spin-lattice relaxation. Smooth distributions of relaxation

times were generated by minimizing $\chi^2 + \mu A$, χ^2 was maximally increased by 3% above its minimum by enlarging the regularization parameter μ.

The modified version of the Inversion Recovery (see chapter 3) pulse sequence was employed to obtain the FID curves for T_1 analyses. Furthermore, the free induction decay curve was decomposed into two separate components to investigate T_1 distributions for the motionally restricted and the mobile components. To acquire the total NMR signal, S_0 was estimated by moment expansion as explained in chapter 4 for all the τ values to obtain a T_1 decay curve. For the mobile component, L_0 was estimated for all τ values by fitting the FID curve between 200 μs and 1800 μs to a monoexponential algorithm. T_1 decay curves for $S_0 - L_0$ and L_0 were analyzed with NNLS to determine the T_1 distributions for the motionally restricted and mobile components.

5.2.4 Dehydration

All samples were weighed and then dried under vacuum at 55^0 C to constant weight in order to obtain their gravimetric Wet/Dry ratio. One additional sample was dehydrated incrementally by allowing evaporation of water under vacuum at room temperature. Lung weight measurements were performed at each step. Finally, the samples were dried to constant weight.

5.3 Results

5.3.1 Collagen Assay

Employing hydroxyproline assay experiments, the collagen contents of 15 samples were determined. As mentioned earlier, collagen is an important protein present in the lung tissue. Its

properties include the high tensile strength, rigidity, and affinity for binding to water molecules due to its polar structure. The collagen content of the peripheral lung tissue samples ranged from 13% to 41% of the dry weight.

5.3.2 NMR Water Content Measurements

A typical FID from a lung sample was shown in Fig. 4.1. S_0, the total NMR signal at t=0, was estimated by fitting the motionally restricted component to the moment expansion (see the inset of Fig. 4.1). L_0, the signal from water and mobile non-aqueous tissue at t=0, was obtained from fitting the curve to a monoexponential algorithm. These values in conjunction with the percentage distribution and hydrogen content per unit mass of all the components were used to determine Wet/Dry ratios.

5.3.3 Inversion Recovery Measurements

The spin-lattice relaxation was measured in four lung samples. To obtain the T_1 decay curve, all curves with different τ values were first base-line corrected. After this correction, these curves were sampled in a window which ranged between 4 and 9 μs from the center of the 90° pulse. The inversion recovery decay curves were obtained and fit using NNLS to produce T_1 distributions for the motionally restricted and the mobile components.

For both components, the decay curves were monoexponential. The former component had an average $T_1 = 0.772 \pm (0.11)s$ and the mobile component had a T_1 of $0.967 \pm (0.02)s$. The smooth T_1 distributions for the motionally restricted and mobile components are depicted in Fig. 5.1. Since these T_1 values are relatively close to each other, there may have been an

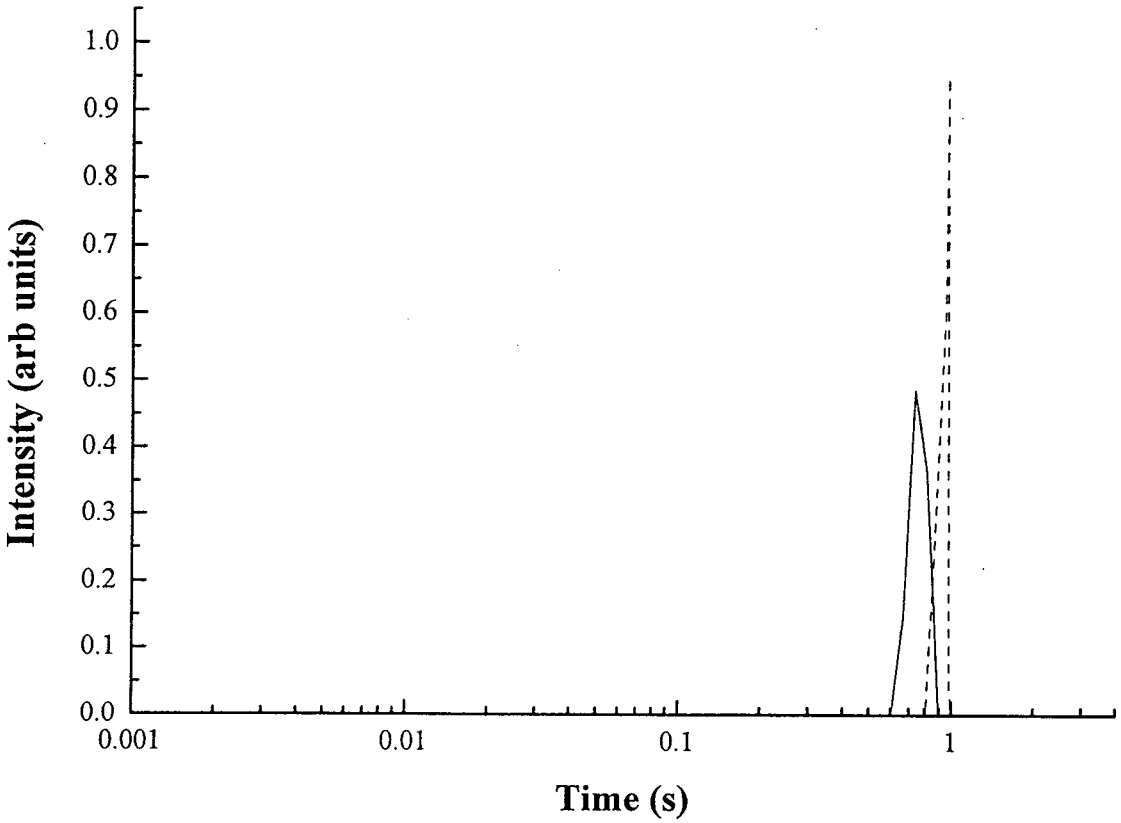

Figure 5.1: The solid line is the smooth T_1 distribution of the motionally restricted component and the dashed line is the smooth T_1 distribution of the mobile component from a representative lung sample.

exchange of magnetization occurring between the two components.

The T_1 time measured in this study was much shorter than the 10 s repetition times employed, indicating that the results were not corrupted by T_1 weighting.

5.3.4 CPMG Measurements

To characterize the mobile fraction of the lung samples, the T_2 relaxation decay curve was acquired using the CPMG sequence. The inset of Figure 5.2 demonstrates that the CPMG decay curve was not a straight line on a semilog plot and hence could not be fitted by a single

T_2 component corresponding to a single water environment. Figure 5.2 shows typical NNLS discrete and smooth T_2 distributions for the mobile signal. Due to the inhomogeneous nature of the structure and biochemical composition of the lung tissue, it may be more plausible to assume a smooth distribution for relaxation times. Moreover, the smooth fit is more robust in the presence of noise.

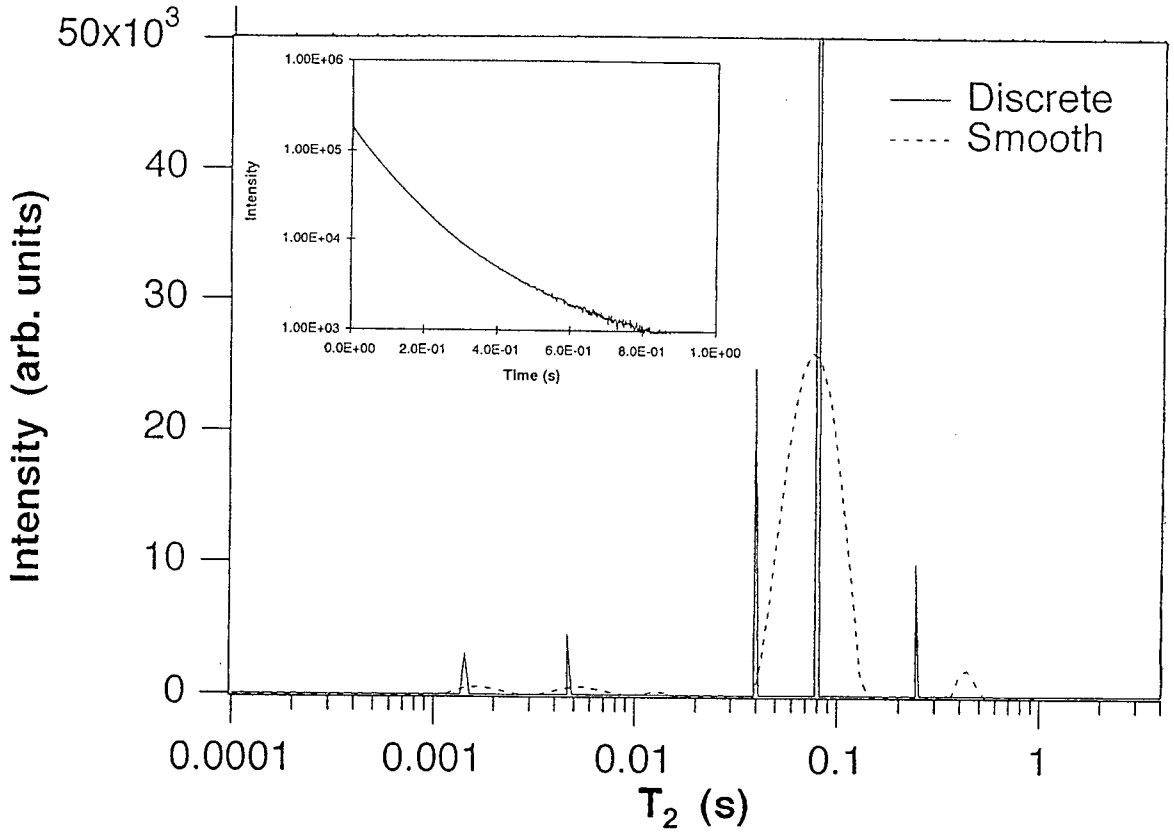

Figure 5.2: Smooth T_2 distribution of the mobile component (dashed lines) and discrete distribution (solid lines) from a typical lung sample. The inset is the T_2 magnetization decay curve from the CPMG pulse train on a semilog plot, $\tau = 200\mu s$.

Four to five resolvable T_2 components were consistently obtained which is in agreement

with the literature [54]. These components had ranges of 2-6, 10-40, 80-110, and 190-400 ms with average T_2 values of $4 \pm 0.4, 35 \pm 1.7, 93 \pm 2.8$, and 264 ± 28 ms. The largest component accounted for more than 75% of the total amplitude (between 80-110 ms).

To have a better understanding of the motions responsible for the T_2 relaxation, four different values of echo spacing, τ, of 100, 200, 400, 600 μs were applied to look for shifts or any other changes in the T_2 relaxation time distribution. However, no changes were observed. This result indicated unambiguously that correlation times of 100 μs or longer do not play any role in the T_2 relaxation results.

5.3.5 Gravimetric Wet/Dry ratios

All twenty-one lung samples were weighed immediately before and after NMR measurements, and after drying to a constant weight. The resulting mean gravimetric Wet/Dry ratio was $5.67 \pm (0.10)$.

5.3.6 Dehydration Measurements

One lung sample was dehydrated incrementally to a constant weight and the free induction decay, the CPMG decay curve, and the sample weight were measured at each hydration level. Using Eqn [4.1], S_0, L_0, and M_2 were estimated as a function of sample hydration. Figure 5.3 shows the T_2 distribution at 4 hydration levels. We note that the T_2 time of the shortest T_2 component remained relatively constant; however, its amplitude increased at later stages of the dehydration process and was non-zero after the lung had been dried to constant weight. This component was therefore assumed to be non-aqueous. The amplitudes and the T_2 times for the

other components decreased with decreasing moisture content and they were absent from fully dehydrated samples.

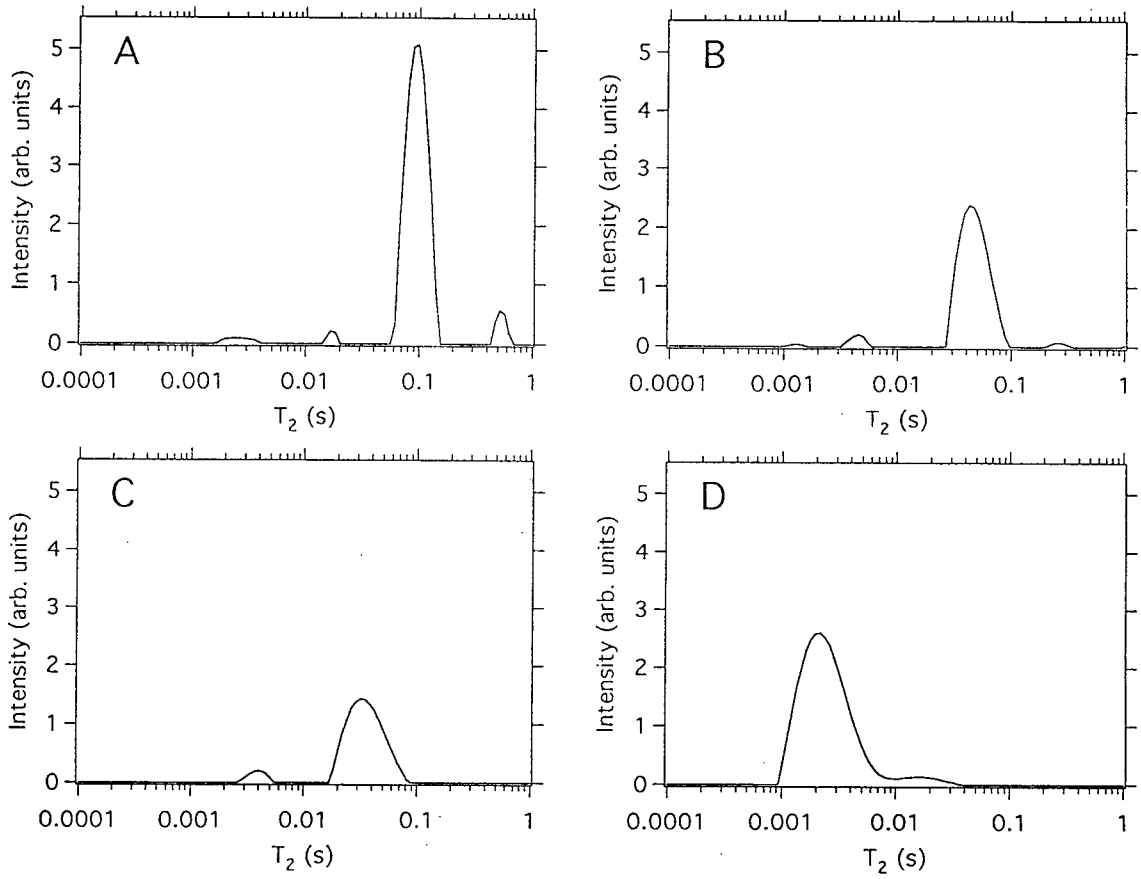

Figure 5.3: The smooth T_2 distribution of the mobile signal from a lung sample at four different hydration levels: (A) For the fresh lung sample, wet/dry = 6.22, four resolvable components were obtained. (B) As the sample was dehydrated, wet/dry = 3.65, the four resolvable components were shifted towards lower relaxation times and their amplitudes decreased. (C) At wet/dry = 2.65, only two components remained. (D) For the fully dehydrated sample, wet/dry = 1.00, a component with an average T_2 of 4 ms remained.

Three hundred MHz ^{1}H NMR spectra were measured on a wet and a fully dehydrated sample. For the wet sample, a single broad peak was observed centered around 5.3 ppm from $Si(CH_3)_4$ which was assigned to water (see Fig. 5.4). After the sample was fully dehydrated

under vacuum at 55^0, the spectrum contained a broad peak around 6.8 ppm (Fig. 5.4). This peak was associated with non-aqueous mobile protons.

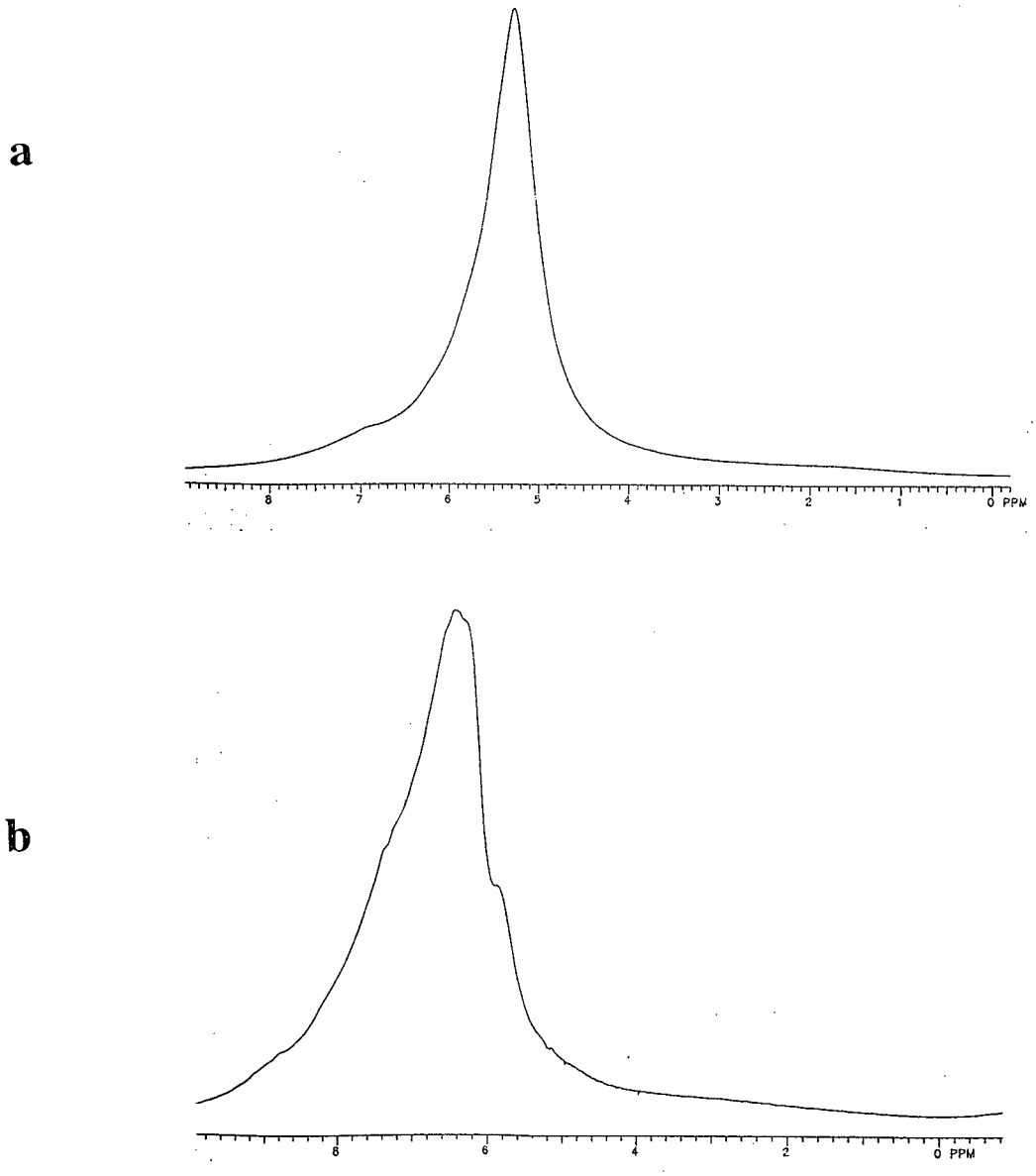

Figure 5.4: The ^{1}H NMR spectra of the lung tissue. a) The 300 MHz NMR spectrum of a wet lung tissue. A main peak centered at 5.3 ppm was observed . This was assigned to water. b) The spectrum obtained from the completely dehydrated tissue contained a broad peak was around 6.8 ppm which was associated with non-aqueous mobile protons.

5.4 Discussion

5.4.1 Collagen Content Measurements

Collagen is a major constituent of lung tissue representing from 13% to 41% of the weight of the samples used in this study. Collagens of different types are the major group of proteins in the lung, present in all major structures, and, more importantly, fibrotic tissue is believed to consist mostly of collagen. Thus, it seemed worthwhile to investigate the dependence of the NMR properties, including motionally restricted and the non-aqueous mobile signal intensities, M_2, T_2 times, T_2 amplitudes, and water content upon collagen content.

Moreover, since collagen is a hydrophilic protein, it should play an important role in the lung tissue water distribution [15]. Only two correlations with $R^2 \geq 0.5$ were observed. Figure 5.5 shows an inverse correlation ($R^2 = 0.760$) between the collagen content and the amplitude of the 1-10 ms T_2 component. This suggested that an increase in collagen content resulted a decrease in the non-aqueous component. An inverse correlation with $R^2 = 0.580$ was also found between the collagen content and the amplitude of the T_2 component which ranged between 80-110 ms and accounted for the bulk of lung water content (see Fig. 5.6). Note that R^2 represents the proportion of the variance attributed to one variable by the other variable which indicates that 0.76 and 0.58 are non-negligible amounts.

For other NMR properties, no linear correlations with correlation greater than ($R^2 = 0.43$) were found. We conclude that the role of the contribution of collagen in determining the structure and dynamics of lung tissue cannot be considered independently of the other non-aqueous molecular constituents.

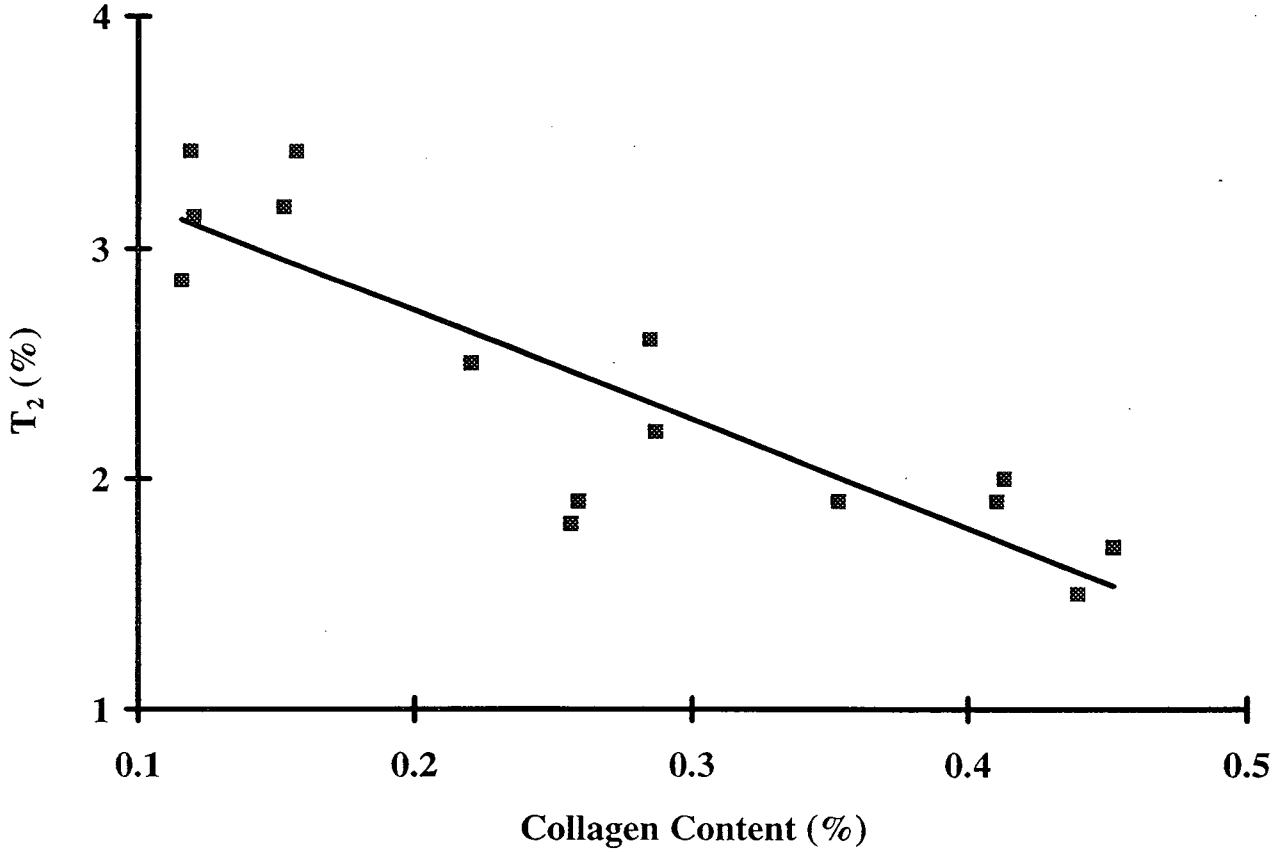

Figure 5.5: The amplitude percentage of the 1-10 ms T_2 component plotted as function of collagen content (collagen mass per dry mass) for each lung sample.

5.4.2 Mobile Non-aqueous Signal

In the dehydration study, it was noted that for the fully dehydrated samples, a mobile component with an average T_2 time of 4 ms remained; this component was also present in wet samples. It was then hypothesized that the 4 ms T_2 component was due to the non-aqueous mobile protons. This hypothesis was consistent with the NMR spectrum of the fully dehydrated sample which contained a broad line at 6.8 ppm. Figure 5.7 shows that the signal from the

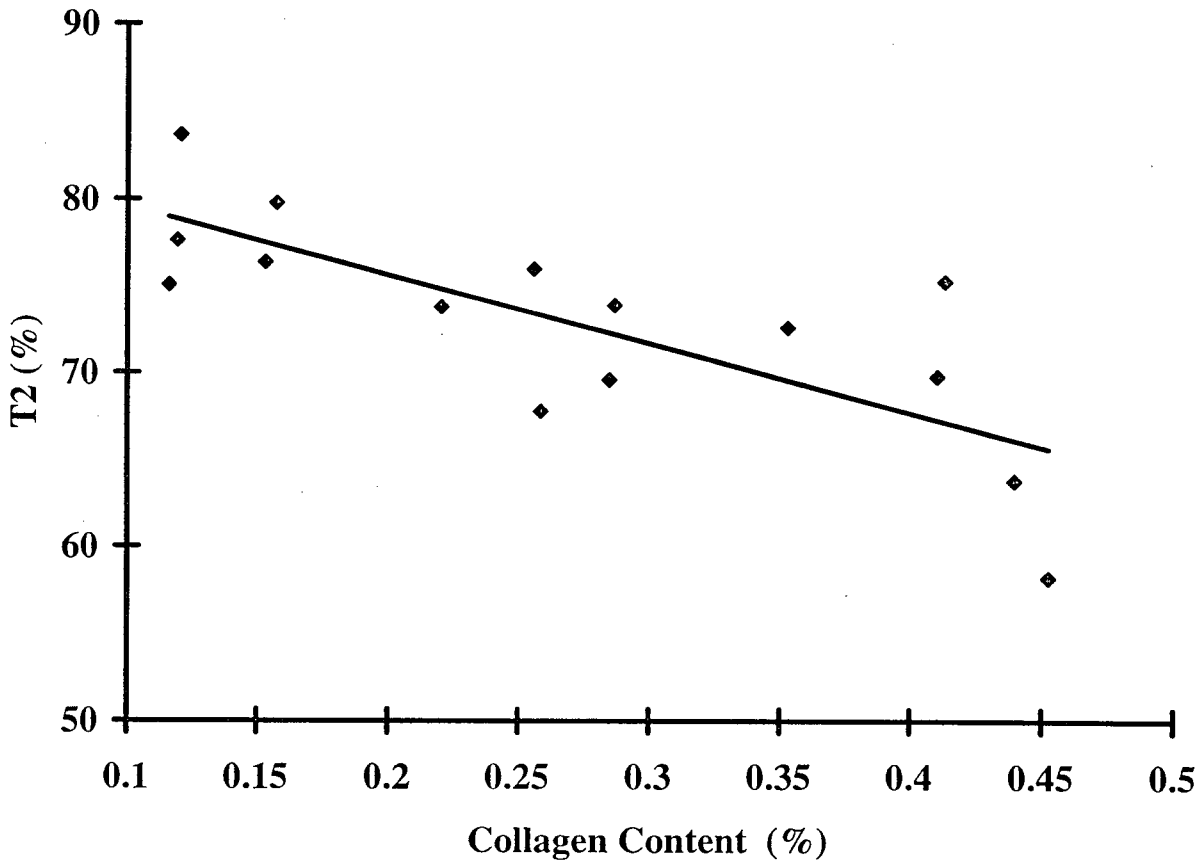

Figure 5.6: The amplitude percentage of the 80-110 ms T_2 component plotted as function of collagen content (collagen mass per dry mass) for each lung sample.

non-aqueous mobile component, L_{nm}, remained relatively constant for most of the dehydration process; $L_{nm}/(S_0 - L_0)$ was about 0.2 ± 0.05 up to the Wet/Dry ratio of 2. However, for Wet/Dry ratios lower than 1.8 it followed an abrupt increase. We do not understand this anomalous increase in $L_{nm}/(S_0 - L_0)$ at low hydrations; however, with regard to water content measurement, it has no physiological significance.

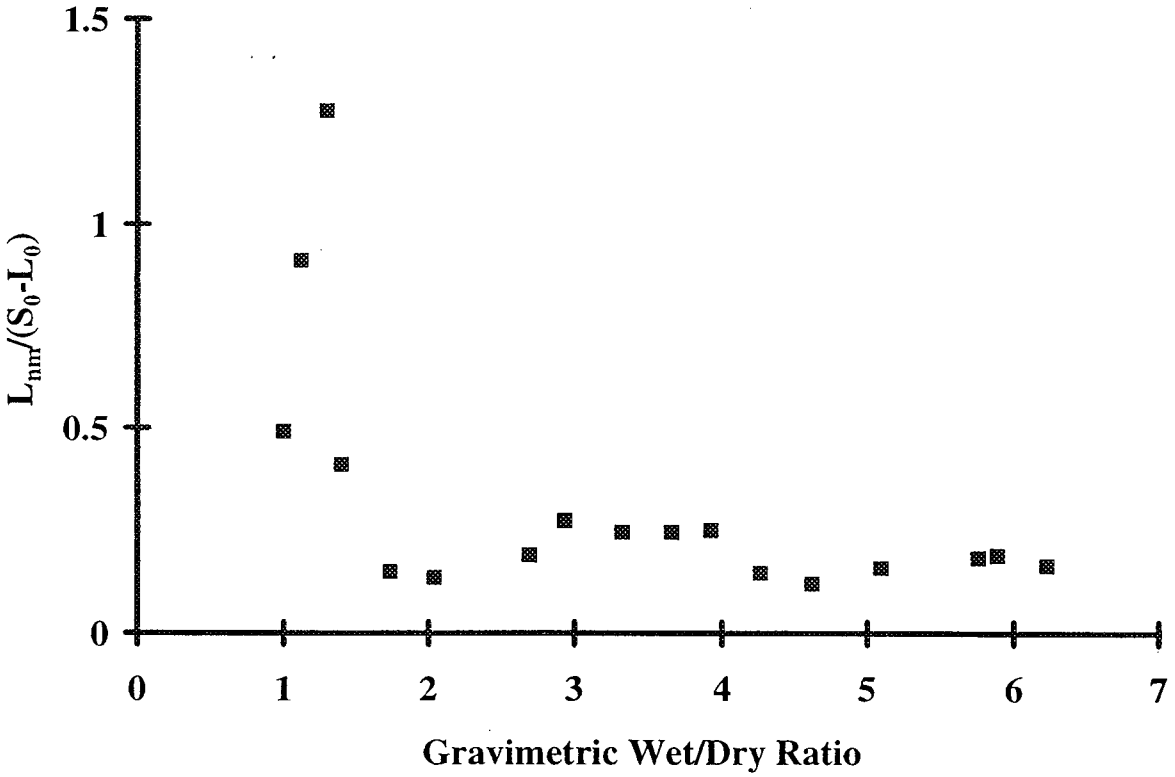

Figure 5.7: The nonaqueous mobile signal amplitude divided by the motionally restricted amplitude $L_{nm}/(S_0 - L_0)$ as a function of gravimetric wet/dry ratio.

5.4.3 NMR Signal Decomposition and Relative Proton Densities

The signal from the lung has been separated into components based upon the NMR properties of each component. NMR signal intensities are proportional to the number of contributing protons. Therefore, to relate NMR signal intensities to sample masses, the hydrogen content per unit mass (ρ) must be known. In this work, two approaches were developed to estimate ρ.

1) **Hydrogen Content Per Unit Mass Based Upon the Chemical Content of Lung:**

Table 5.1 shows a list of chemical constituents of the lung along with their estimated relative proportion [11, 73]. For each constituent, the ratio of the numbers of non-exchangeable hydrogens per molecule to the molecular weight was calculated. This provided the relative mass of hydrogen per unit mass. For collagen, it was assumed that hydrogens not bonded to carbon atoms underwent rapid exchange with water on the ^{1}H NMR timescale. Since more than 95% of collagen in lung is type (I) and (III) [11, 12, 73], collagen α type(III) (col-bovine) with average molecular weight 9365 and with 3817 non-exchangeable hydrogens was used as the representative collagen. Collagen type (I) and type(III) are homologous proteins. Since elastin is an extremely hydrophobic macromolecule, it was assumed that the hydrogens of elastin do not exchange rapidly with water. The representative macromolecule of elastin was els-bovine with average molecular weight of 64230 and with 4731 hydrogens.

Table 5.1: Biochemical Composition of Lung and Its Hydrogen Distribution

Component	Average Dry Weight %	Subcomponent	Average Dry Weight %	Estimated Hydrogen Content per Unit Mass
Collagen	30			0.041
Elastin	25			0.074
		Lipids	30	0.105
Whole cell	45	Proteins	25	0.066
		Non-aqueous mobile	45	0.060

The amount of hydrogen per unit mass of the whole cell constituents was obtained from

earlier study by Bloom *et al.* [50]. Some constituents (e.g. cytoplasmic proteins and metabolites) are expected to tumble isotropically at a sufficiently rapid rate ($\tau \approx 10^{-5}s$) that their dipolar interactions average to zero giving rise to a narrow line. For this reason, the molecular constituents of lung were divided into motionally restricted and mobile categories and their ρ was estimated separately for each classification. For the relative proportions listed in Table 5.1, we estimated the relative amount of hydrogens per unit mass for the motionally restricted non-aqueous, mobile non-aqueous, and water component. When the known collagen content of each sample was included in the calculation (assuming that a decrease in collagen was accompanied by an increase in elastin), the hydrogen content per unit mass for the motionally restricted component, ρ_s, ranged from 0.061 to 0.073 with a mean of $0.066 \pm (0.005)$. This indicated that the observed variations in collagen content had a minor effect upon the estimated ρ_s.

2) **Hydrogen Content Per Unit Mass Estimation Based on Incremental Dehydration:**

Figure 5.8 shows $S_0/(S_0 - L_0)$ plotted as a function of gravimetric Wet/Dry ratio. Assuming all the mobile signal is from water, the Wet/Dry ratio would be given by:

$$Wet/Dry = 1 + \frac{L_0}{(S_0 - L_0)} \times \frac{\rho_s}{\rho_w} \times 100\%. \tag{5.2}$$

where ρ_w is the hydrogen content per unit mass of water. However, if the contribution from the non-aqueous mobile component to L_0 is taken into account, the Wet/Dry lung mass ratio should be related to NMR signal intensities by the following equation:

$$Wet/Dry = 1 + \frac{(L_0 - L_{nm})}{(S_0 - L_0) \times (\rho_w/\rho_s) + L_{nm} \times (\rho_w/\rho_{nm}))} \times 100\% \tag{5.3}$$

where L_{nm} is the signal intensity and ρ_{nm} is the hydrogen content per unit mass of mobile

non-aqueous lung tissue.

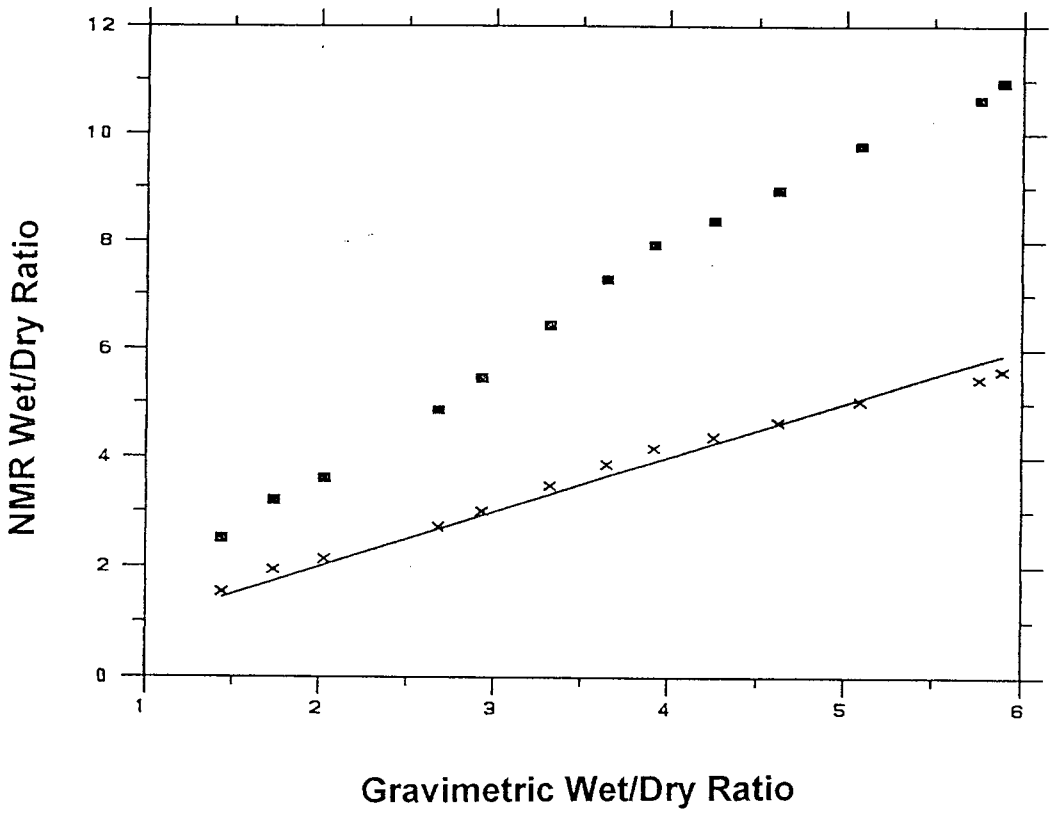

Figure 5.8: The NMR wet/dry ratio, taking the nonaqueous mobile component into account (crosses), and $S_0/(S_0 - L_0)$ (filled squares) plotted as a function of the gravimetric ratio.

Using a non linear functional optimization program [58] , Eqn [5.3] was fit to our results for S_0, L_0, L_{nm}, and gravimetric Wet/Dry ratio. The values of S_0, L_0, and gravimetric Wet/Dry ratio were obtained from the incremental dehydration study. The L_{nm} values were set to $0.2(S_0 - L_0)$ based on the dehydration experiments. Due to the rapid and non linear increase of L_{nm} at very low Wet/Dry ratios, only the first 13 points out of the 17 dehydrations were

used in the fit of Eqn [5.3] in order to estimate ρ_s and ρ_{nm} (Fig. 5.8). The resulting values for ρ_s and ρ_{nm} were 0.0717 and 0.045 respectively. The χ^2 for fitting Eqn [5.3] to the results was 1/16 that obtained using Eqn [5.2] underlining the importance and necessity of including L_{nm} in our calculations.

5.4.4 Estimation of Lung Wet/Dry Ratio by NMR

The NMR free induction decay from each sample was separated into a motionally restricted component with intensity $S_0 - L_0$ and a mobile component with intensity L_0. Using ρ_s, ρ_w, and L_{nm} derived from chemistry in conjunction with Eqn [5.3] we estimated the $(Wet/Dry)_{NMR}$ $/(Wet/Dry)_G$ ratio to be 1.00 ± 0.08 (Table 5.2). The values for ρ_s, ρ_{nm} from the dehydration experiment yielded an average $(Wet/Dry)_{NMR}/(Wet/Dry)_G$ ratio of 1.00 ± 0.05. The outstanding agreement between the two approaches confirms that the chemical composition of lung portrayed in Table 1 was remarkably accurate.

Table 5.2: Comparison of NMR and gravimetric lung wet/dry ratios.

(n=21)

ρ_s		Mean	σ
Estimated (Chemistry)	$(Wet/Dry)_{NMR}$	5.64	0.08
Experimental (NMR)	$(Wet/Dry)_{NMR}$	5.65	0.07
	$(Wet/Dry)_G$	5.67	0.10
Estimated (Chemistry)	$(Wet/Dry)_{NMR}/ (Wet/Dry)_G$	1.00	0.08
Experimental (NMR)	$(Wet/Dry)_{NMR}/ (Wet/Dry)_G$	1.00	0.05

5.5 Conclusions

This chapter reports on the NMR properties of the lung and demonstrates a significant correlation between the NMR signal and pulmonary tissue hydration. The NMR water signal was distinguished from that of non-aqueous mobile protons (in metabolites and cytoplasmic proteins) which had an average T_2 of 4 ms. Discerning these two components, in turn, helped us to obtain an excellent agreement between the NMR and gravimetric Wet/Dry ratio. This indicated that NMR techniques are applicable to the regional and whole assessment of the lung water content.

In conclusion, since many pathologic processes in lung tissue alter water content, this suggests that MR should distinguish normal from abnormal lung tissue. In addition, the differential behaviour of the various T_2 components within lung tissue offers the capability to characterize the water environment with MRI, possibly distinguishing inflammatory from fibrotic processes. This characteristic of the microscopic soft tissue environment cannot be performed by radiologic techniques which only measure lung density.

Chapter 6

MRI Measurements of Water Content and Relaxation Distributions

6.1 Introduction

Since alteration in lung water content is an important feature in a number of lung diseases, an accurate and non-invasive means of measuring lung water would be advantageous and desirable in clinical and research settings [63, 64, 74]. Various methods such as Compton scattering [75], computed tomography [76], gamma ray attenuation [77], and radioactive tracer [78] techniques have been devised and employed to measure lung water content. However, the accuracy and sensitivity of the current methods is only about 20% to 30% [33].

MRI offers the capability of accurately measuring water content in lung in a non-invasive/non-destructive manner [13] and has the potential of having higher sensitivity. For this reason, a large number of MRI studies have estimated the water content in lung both *in vivo* and *in vitro* [35, 79, 80, 81]. Lung water content can be measured by comparing the NMR signal from lung, in the absence of T_1 and T_2 weighting, with that from a water standard. This is, however, complicated by the rapid MRI signal attenuation due to the magnetic field gradients intrinsic to the air-soft tissue matrix of inflated lung. Consequently, the T_2 decay of the lung signal must be characterized in order to accurately measure water content.

Measurements of NMR relaxation times in lung tissue have also been performed both *in*

vitro and *in vivo* [28, 29, 68, 69, 70, 82]. As the relaxation times are affected by the local microscopic water environment, they can potentially differentiate clinically important processes such as inflammation or fibrosis.

In the previous chapter , using the NMR spectrometer, the entire proton signal from excised fragments of lung tissue was characterized and a nonaqueous mobile component was separated from the water signal [79]. In that study, excellent agreement was also found between the gravimetric and NMR water content measurements performed on excised deflated lung tissue fragments $(Wet/Dry)_{NMR}/(Wet/Dry)_G = 1.00 \pm 0.08$ [59, 79]. The primary goal of this chapter is to validate the use of a large bore 1.5 T clinical MRI scanner to measure water content in inflated *in vitro* whole lungs and extend our previous *in vitro* results. Ultimately, we would like to utilize MRI as a noninvasive method to diagnose the early stages of inflammatory diseases in patients. If inflammatory lung disease is diagnosed early before irreversible scarring occurs, current therapies are more effective. The secondary goal of this work is to report on T_2 distributions in *in vitro* deflated, *in vitro* inflated, and *in vivo* lung measured with the same experimental settings to make comparisons with previously published data [28, 29, 79].

6.2 Experimental

6.2.1 Samples

MRI measurements were performed on nineteen excised lungs from healthy juvenile pigs. The sample preparation was explained in chapter 3. Of the nineteen lungs, fifteen lungs were measured at a single water content, two lungs were measured at two water contents, and two

lungs were measured at three water contents for a total of 25 measurements. Ten single lung-water-content measurements were acquired with a quadrature birdcage head coil to ensure higher S/N ratio. The rest of the measurements were performed with the body coil to more closely replicate the human *in vivo* situation.

The lungs were inflated with an inflation pressure of 10 cm H_2O during the course of the experiment and their volume remained constant throughout the imaging period. Two water phantoms doped with $MnCl_2$ adjacent to the left and right lungs were imaged simultaneously for reference. One collapsed lung as well as collapsed regions of 2 other lungs were used to investigate the effect of inflation on T_2 distributions. Lung MRI measurements were also carried out on two live juvenile pigs. The cardiac gating procedure was demonstrated in chapter 3.

Four lungs were dehydrated incrementally in order to assess the sensitivity of MRI with respect to water loss and obtain a wider range of water content measurements. At each step, after weighing the sample, MRI measurements of water content and T_2 distribution were performed. Following MRI measurements, all samples were weighed and cut into smaller pieces to allow more surface for evaporation. To obtain the gravimetric water content, the lungs were left under vacuum for 1 to 2 days at room temperature. Then, the temperature was increased incrementally to 55^0 C, while still under vacuum. The drying process continued until constant weight was attained.

6.2.2 MR Measurements

MRI measurements were carried out on a 1.5 T GE Signa MRI scanner (General Electric Medical Systems, Milwaukee, 5.4 level). The lungs were imaged using a previously validated

single slice multi-echo pulse sequence (as defined in chapter 3) to produce an accurate T_2 decay curve for lung tissue and the water standard. The entire lung was imaged with successive offsets of 10 mm thick single slices.

The multi-echo sequence was run on a single midlung axial slice to perform *in vivo* measurement. The trigger time was 250 ms from the peak of the carotid pressure curve corresponding to the diastolic T_2 decay curve. The *in vivo* TR times were close to 2 seconds. Respiration artifacts were reduced by using respiratory compensation technique developed by GE.

6.2.3 Relaxation Analyses

The partial saturation spin echo sequence (as defined in chapter 2) was applied to a single central lung slice to estimate T_1 relaxation times for the lungs and water standards. The partial saturation data was converted to a decaying exponential form by subtracting it from the magnetization at infinite TR, S_{inf}. After this conversion, the T_1 value for each lung was determined using the NNLS algorithm.

The T_2 analysis was only performed on lung imaged with the body coil. The T_2 distribution for volumes of interest (VOI) from *in vitro* inflated, *in vitro* deflated and *in vivo* lungs were determined by the NNLS method. The decay curves obtained from the multi-echo pulse sequence can be represented by Eqn [5.1]. Smooth distributions of relaxation times were generated by minimizing $\chi^2 + \mu A$. χ^2 was maximally increased by 1% above its minimum by enlarging the regularization parameter μ. For the geometric mean T_2 calculation (the mean T_2 on a log scale), the analysis was performed on each of 10 lungs on a voxel-by-voxel basis.

6.2.4 Water Contents

For each lung and water standard, the average proton density was obtained by summing the T_2 component amplitudes in the T_2 distribution returned by NNLS. This is equivalent to the T_2 magnetization decay curve amplitude at zero time. For the head coil, there was substantial drop-off in coil sensitivity for locations a few cm away from the center of the coil along the coil axis. This radio frequency inhomogeneity effect was corrected by dividing the proton densities by a one dimensional coil sensitivity profile derived from MR images of a uniform water phantom in the head coil. For the body coil images, the coil sensitivity was relatively uniform across the images and no radio frequency inhomogeneity correction was applied.

Proton densities of the lung slices and the water standard were then corrected for T_1 saturation effects, using

$$S_c = S_0/(1 - e^{-TR/T_1}). \tag{6.1}$$

where S_0 is the measured signal at zero time, and S_c is the T_1 corrected signal. This equation applies to both lung and water standards. T_1 times were derived from the central slice. Then the average water density (in g/ml) of the lung in each slice was obtained from the ratio of the T_1-corrected proton densities for the lung and the water standard (assumed to have density of 1 g/ml). The amount of water in each slice was obtained by multiplying its average water density by the slice volume. The total water content of each lung was acquired by summing the contributions from all the slices.

6.3 Results and Discussion

6.3.1 Water Content Measurements

Figure 6.1 shows typical sagittal images of the left and right inflated lungs from one pig. MRI lung water content was estimated by comparing the proton density of the lung to that of the water standard.

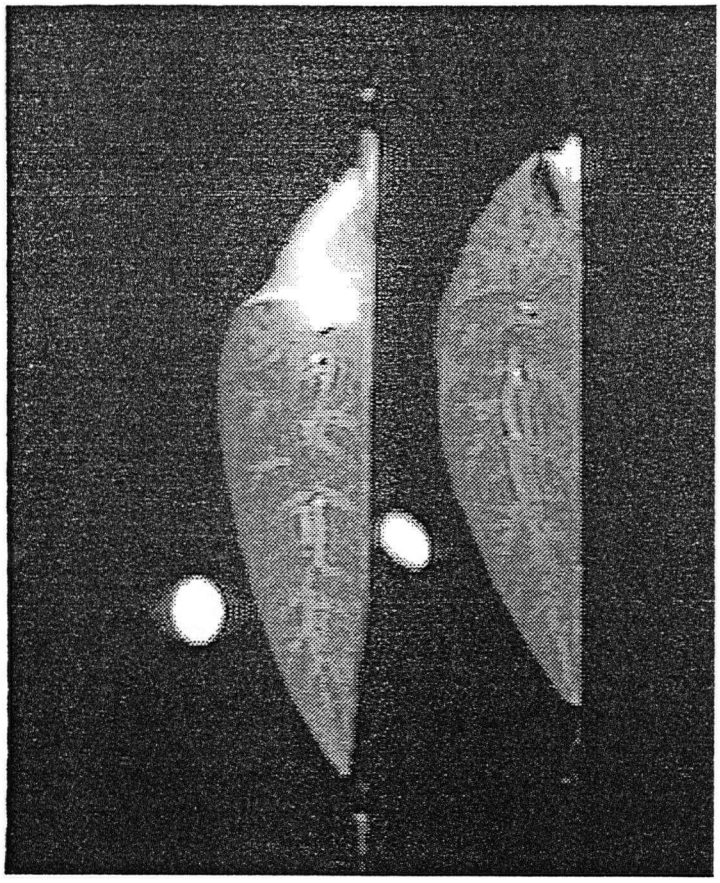

Figure 6.1: A sagitttal image of the left and right lungs with accompanying water phantoms generated using the single slice 16 echo pulse sequence (echo spacing of 10 ms).

Figure 6.2 shows the MRI water content plotted as a function of the gravimetric measurements. Linear regression analysis of the data in Fig. 6.2 gave a correlation coefficient squared (R^2) of 0.98. The values of the slope and intercept along with their standard deviations were 1.05 ± 0.03 and -3.1 ± 3.5, respectively.

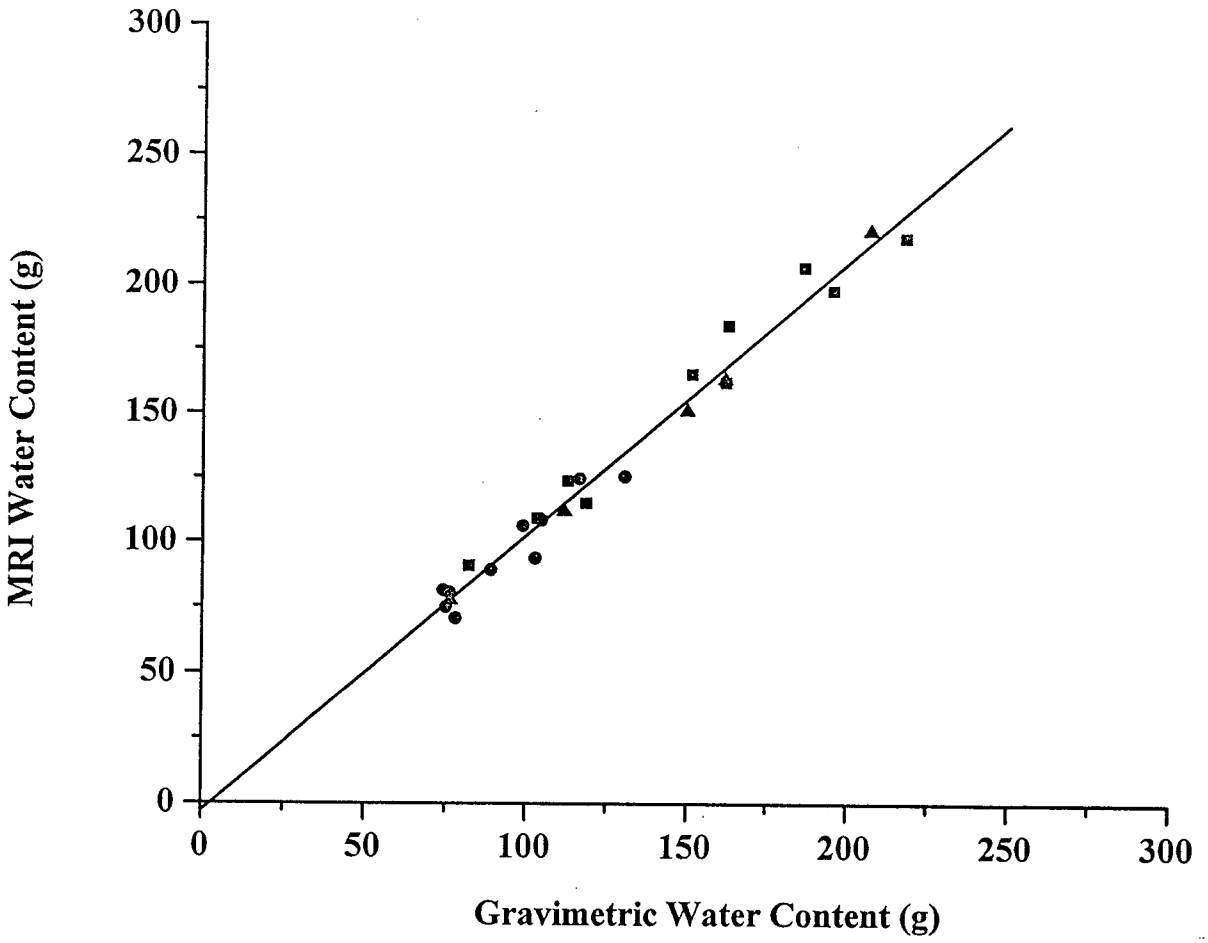

Figure 6.2: The MRI water content obtained from the dehydration technique (solid □), head coil (solid ○), and body coil (solid △) measurements are plotted as a function of gravimetric measurements. The line corresponds to the regression fit with $R^2 = 0.98$, m = 1.05 ± 0.03, and b = -3.1 ± 3.5.

When the zero intercept constraint was incorporated, it resulted in a linear correlation coefficient squared of 0.98 and a slope of 1.03 ± 0.04. In either case, there was excellent agreement

between the water content measured by MRI and gravimetric methods.

Assuming that the gravimetric measurements were accurate, the mean difference and standard deviation between the gravimetric and MRI water contents for the body coil (not including incremental dehydrations) and the head coil were $-3.6g \pm 5.6\%$ and $-0.7g \pm 6.2\%$,respectively. The low mean-difference value for the head-coil measurements indicated that the corrections of the rf inhomogeneity artifact were effective. Measurements from lungs which were dehydrated incrementally had a mean difference and standard deviation of $-7.8g \pm 8.6\%$. These higher values were mainly due to the most dehydrated lungs (wet/dry = 3.16, corresponding to 75 grams of water loss). The mean difference and standard deviation for all measurements combined was $-4.1g \pm 7.6\%$.

It is worthwhile mentioning that the most dehydrated samples had markedly different appearances from the wet lungs. If the measurements of the three most dehydrated lungs were excluded from the calculation, it would decrease the mean difference and standard deviation in water content for the incremental dehydration from $-7.8g \pm 8.6\%$ to $-2.9g \pm 6.0\%$ and all measurements from $-4.1g \pm 7.6\%$ to $-2.0g \pm 5.9\%$. The small negative mean differences observed between the two methods in all experiments may reflect minute evaporative losses in the time between MRI and gravimetric determinations (despite the cautions taken to prevent these losses). Therefore, our technique for MRI determination of lung water was robust with respect to head and body coil measurements and to a wide range of water contents.

In a previous study of pig lung [79], which employed a much shorter echo spacing of 200 μs, a mobile component with T_2 of 4 ms was measured. This T_2 component, which made up 1 to 3 % of the total NMR signal, was assigned to mobile nonaqueous protons. In the current

study, this component should contribute less than 0.5 % to the signal of the 10 ms echo and nothing to the other echoes. Hence, the mobile nonaqueous component could have introduced small overestimate to MRI water content measurements.

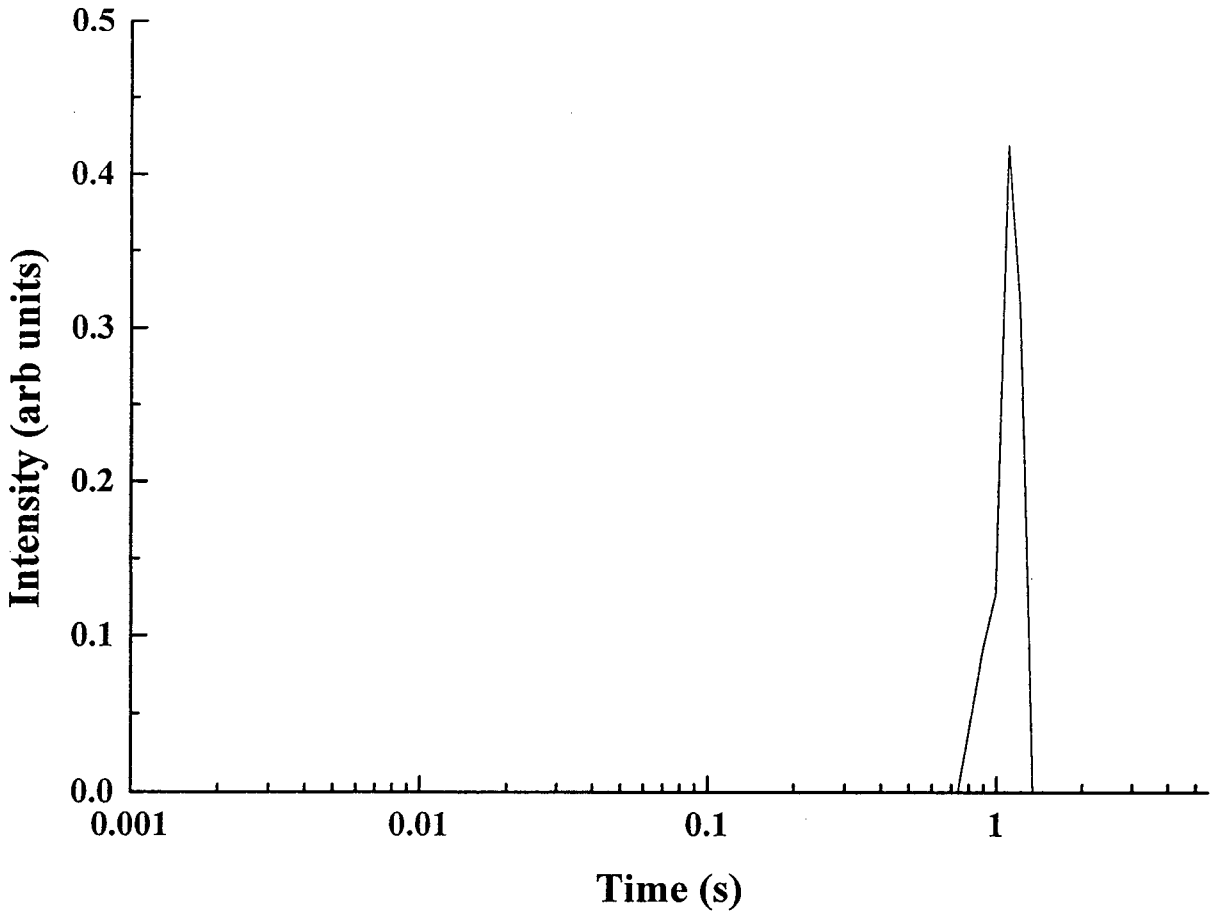

Figure 6.3: A typical T_1 distribution obtained from an inflated lung. The whole lung was selected as a voxel of interest (echo spacing of 10 ms).

T_1 relaxation measurements were performed to correct the MRI water content values for the T_1 weighting introduced by the relatively short repetition time (TR=2000 ms). The converted T_1-decay curves obtained from the partial saturation sequence were fit using NNLS to obtain

the T_1 values. The decay curves for the lungs were always found to be monoexponential with an average T_1 time of 1.06 ± 0.08 s, in four lungs. Figure 6.3 shows a representative T_1 distribution obtained from an *in vitro* inflated lung.

Figure 6.4 shows T_2 magnetization decay curves obtained from *in vitro* deflated (solid squares), *in vitro* inflated (solid triangles), and *in vivo* (solid diamonds) lungs .

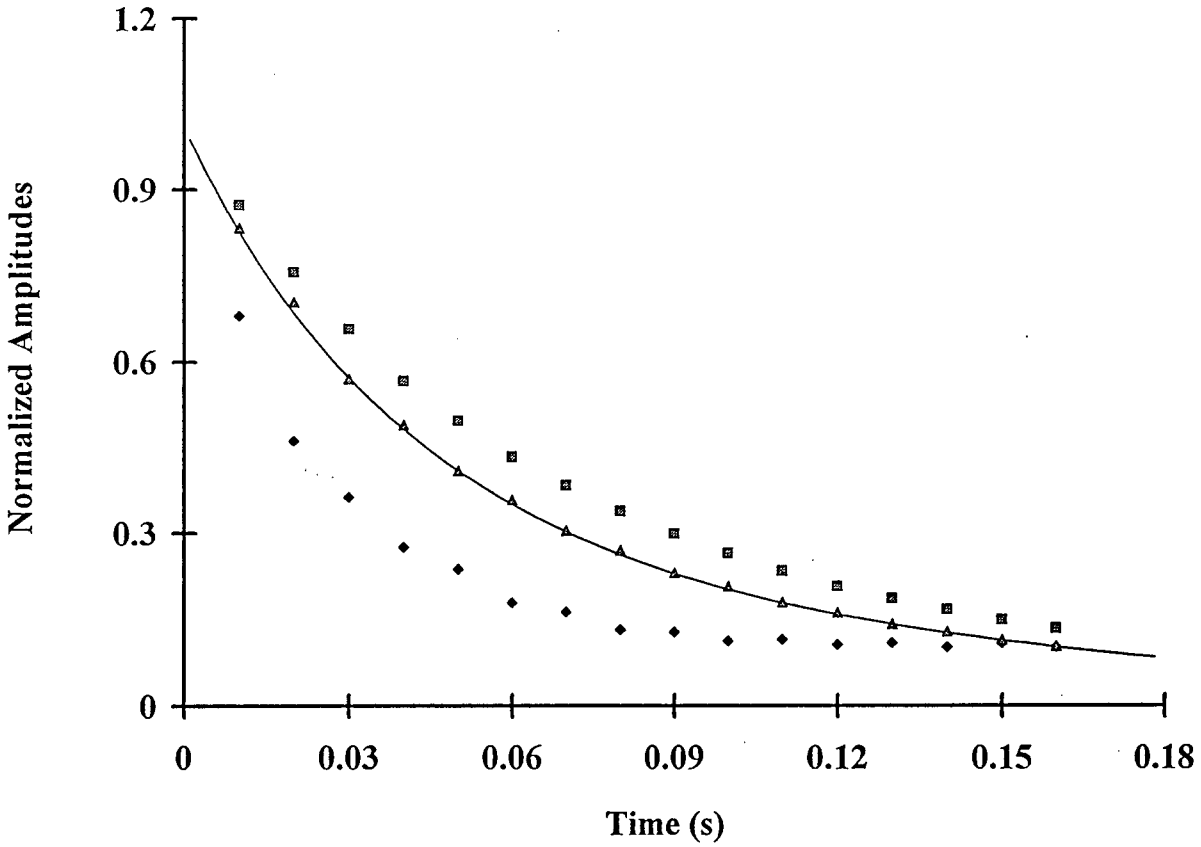

Figure 6.4: Representative T_2 magnetization decay curves from a deflated (solid □), an inflated (solid △), and *in vivo* lung (solid ◇) acquired by the single slice 16 echo pulse sequence with an echo spacing of 10 ms. All the three curves were normalized to have a zero time intercept of 1. The solid curve was obtained from fitting the data points using the NNLS algorithm.

When a collapsed lung is inflated, the T_2 decay curve steepens (relaxation times shorten).

The mechanism for this dephasing is diffusion of the water molecules in local magnetic field inhomgeneities caused by magnetic susceptibility differences at air-lung tissue interfaces [26]. The T_2 decay curve from *in vivo* lung is further steepened due to additional MR signal dephasing because of blood flow in the presence of air-tissue field gradients.

Figure 6.5 shows the smooth NNLS T_2 distributions corresponding to the 3 decay curves in Fig. 6.4. The T_2 distribution from the *in vivo* lung (dotted lines) contained two T_2 peaks whereas that from *in vitro* deflated (solid lines) and inflated (dashed lines) lung contained 3 peaks. The solid lines in figure 6.5 show a typical smooth T_2 distribution from an *in vitro* deflated lung. The average T_2 values, over 120 VOI's in 4 lungs, were 34 ± 13, 93 ± 6, and 163 ± 20 ms with relative amplitudes of $20 \pm 17\%$, $73 \pm 17\%$, and $7 \pm 6\%$ of the total signal, respectively. These T_2 distributions were in satisfactory agreement with those measured with a spectrometer on excised pig lung segments [79]. However, we should bear in mind that the previous measurements (8) were performed at 2.1 T with an echo spacing was $200\mu s$.

Figure 6.5 also illustrates a representative smooth T_2 distribution present in an *in vitro* inflated lung (dashed lines). Three distinct components were observed, over 120 VOI's in 10 lungs. The average T_2 values and their respective standard deviations were 18 ± 6, 59 ± 16, and 206 ± 35 ms with relative amplitudes of $41 \pm 14\%$, $53 \pm 12\%$, and $6 \pm 5\%$, respectively. The T_2 distribution for the inflated lung was shifted towards shorter relaxation times compared to deflated lung. This is felt to be due to the growth in the size of alveoli with lung inflation, which increases the magnitude of the internal magnetic field inhomogeneity.

A major problem in comparing T_2 studies of inflated lung by different groups is that the shape of the decay curve not only depends upon the strength of the magnetic field but also

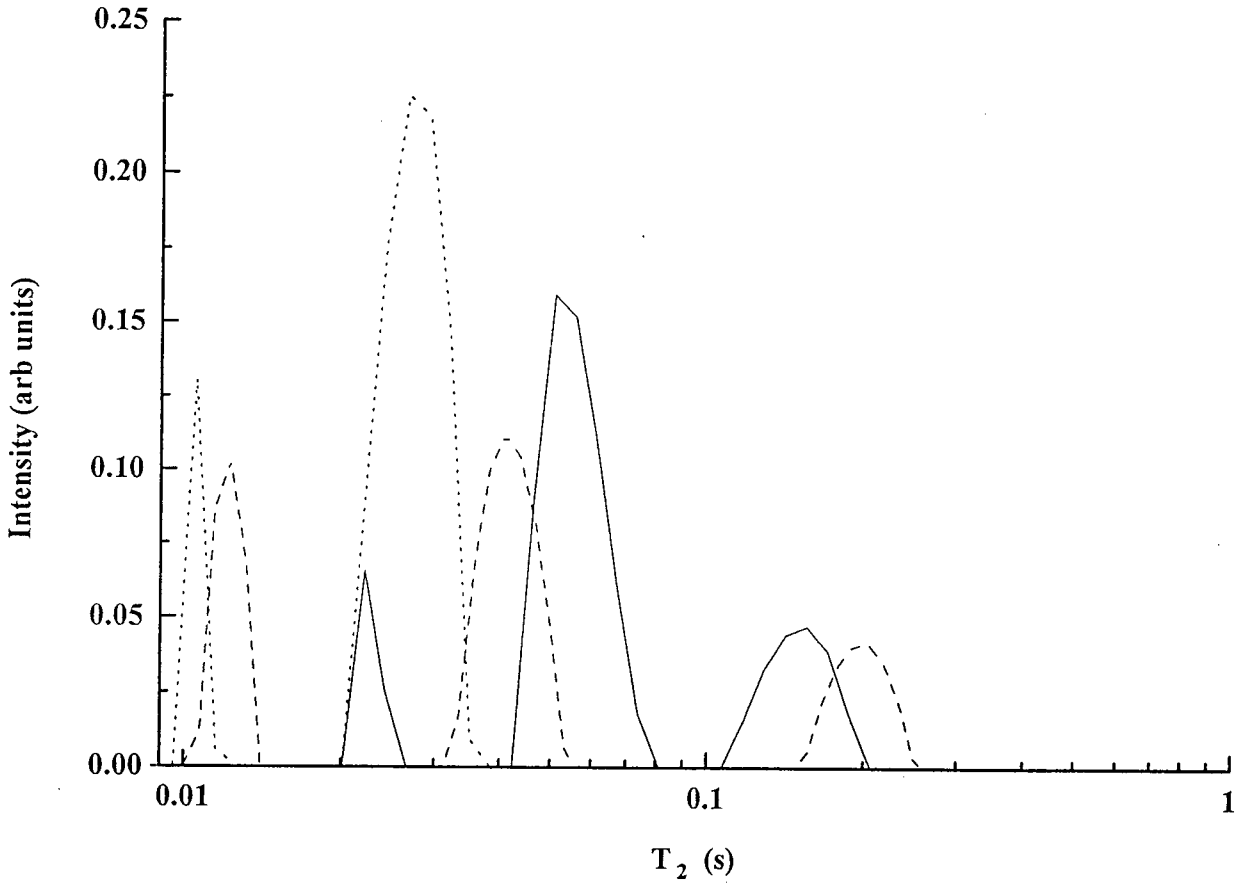

Figure 6.5: Smooth T_2 distributions from an *in vitro* deflated (solid lines), an *in vitro* inflated (dashed lines), and *in vivo* lung (dotted lines) superimposed.

upon how it is measured [26, 34]. In previous studies [27, 28, 29], *in vitro* T_2 measurements performed on Sprague-Dawley rats' excised whole lung inflated at 20 cm H_2O resulted in a T_2 distribution with two T_2 times of 10 and 35 ms. In that work, the images were acquired at 1.95 T using a single Hahn echo with echo times between 16 and 110 ms. The T_2 values measured in our study were longer due to the lower field (1.5 T). Besides, we used a CPMG pulse sequence with echo spacing of 10 ms which was capable of reducing MR-signal dephasing due to water diffusion. In fact, our study was able to detect the longer T_2 component which

was not observed in previous studies [28, 29] due to diffusion mediated dephasing and/or low S/N ratio. For the *in vivo* lungs, the diastolic T_2 distributions were obtained over 30 VOI's in

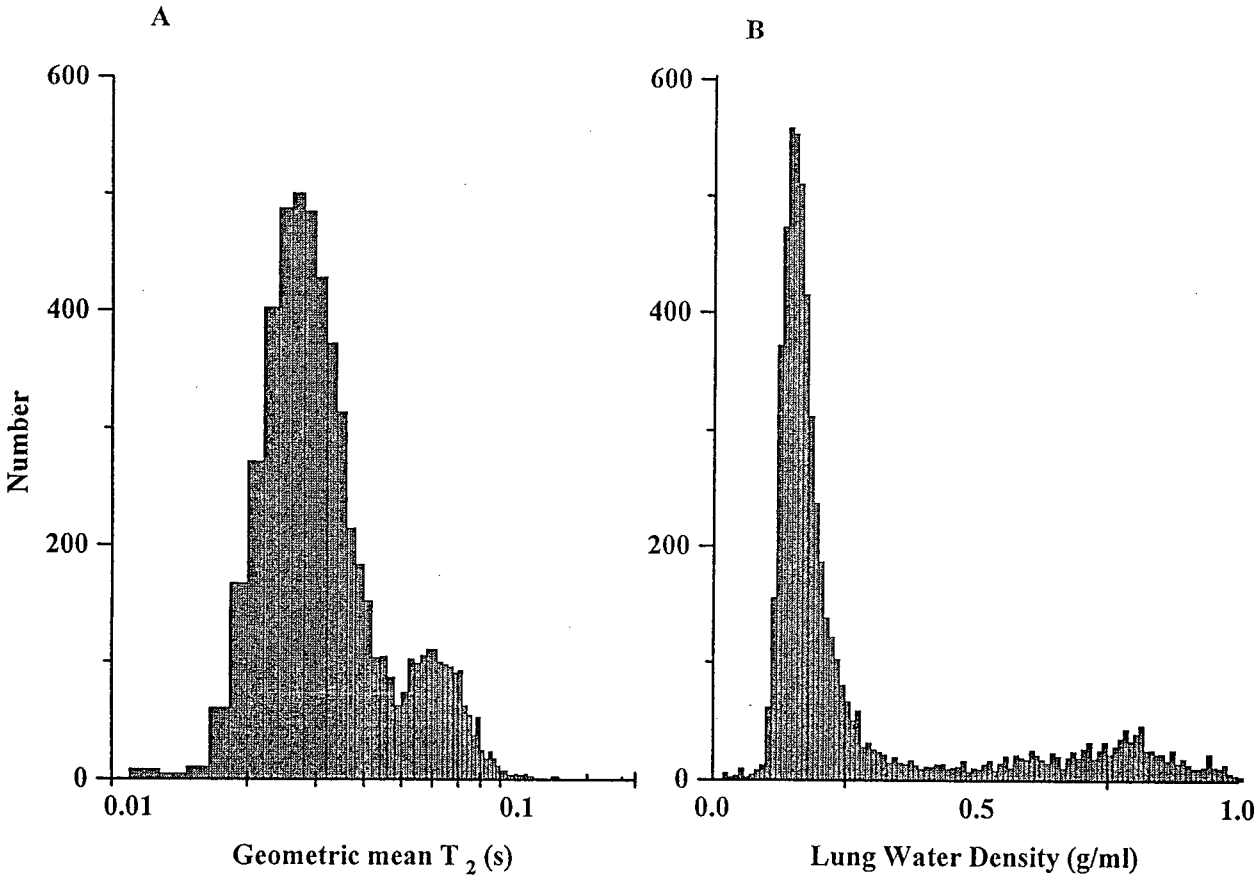

Figure 6.6: The geometric mean T_2 values (A) and lung water densities (B) histograms generated from each voxel in the mid-sagittal image.

2 pigs. The smooth T_2 distributions had two resolvable components with average T_2 times of 10 ± 1 and 29 ± 6 ms. Approximately, 85% of the total amplitude was at 29 ms. While the T_2 time of the 10 ms part was not very well defined because the shortest TE time and smallest value in the NNLS T_2 partition were also 10 ms, its amplitude should be much more robust.

In a previous study [28], which employed a modified line scan technique operating at 1.95 T, a series of 16 Hahn-spin echo sequences (TE= 16-90) were used to determine the T_2 distribution in rat lungs. The measured T_2 components were about 9 and 34 ms with more than 90 % of the total amplitude being around 9 ms. The average *in vivo* T_2 reported in our experiment was longer than the previous measurement [28] because we used a multi-echo rather than a Hahn-echo pulse sequence to determine the T_2 distribution.

Lung tissue is quite heterogeneous and complex. No other organ in the body is so heavily dependent upon the proper architecture and stability of the connective tissue for proper function. This intricacy and heterogeneity of lung tissue is clearly depicted in the nonuniformity of MRI signal intensity (Fig. 6.1). This inhomogeneity showed up in our analyses as variances in both water densities and T_2 distributions. For example, the longer T_2 time near 200 ms was not present in all VOI's chosen thereby making it difficult to compare the results from different lung regions.

To characterize the spatial dependence of the T_2 distribution and water density, images of lungs were globally analyzed and the geometric mean T_2 as well as the lung water density were determined for each voxel in the lung. The geometric mean T_2 histogram for an *in vitro* inflated lung, plotted in Fig 6.6A, contained two peaks: one at 28 and the other at 62 ms. The lung water density histogram from the same lung, Fig. 6.6B, also exhibited 2 distinct regions with 90 % of the lung volume at an average water density of about 0.18 g/ml and the rest of lung at an average density of 0.8 g/ml. The lung at 0.18 g/ml was inflated and that at 0.8 g/ml was collapsed. The linkage between the geometric mean T_2 and lung water density is investigated in the following chapter in detail.

6.4 Concluding Remarks

This part of the research project was designed to validate an MRI technique for measuring the lung water content in a whole body clinical imager operating at 1.5 T. The excellent agreement between gravimetric and MRI water contents in *in vitro* inflated and *in vitro* deflated lungs, which exhibited a wide range of water densities and T_2 distributions, suggests that this technique should be applicable to *in vivo* studies. Since many lung diseases are associated with changes in water content, the ability to measure lung water content *in vivo* non-invasively should be clinically valuable.

This study found that T_2 decay curves varied markedly within the lung. It also showed the multi-exponential nature of the T_2 distribution in lung samples. Although the multi-exponential nature of T_2 relaxation in lung has been observed in several studies [27, 28, 32, 79], so far there has been no assignment of these components to specific water environments. In other biological systems, different T_2 peaks have been related to different local water environments; for example, in brain, T_2 components have been assigned to water compartmentalized in myelin and cytoplasmic/extracellular water [84]. In wood, the T_2 peaks were assigned to cell wall water and lumen water [85].

If this behavior of the T_2 distribution in lung can be understood, there would be a potential for using T_2 results to obtain more specific information about lung pathology. Furthermore, the voxel based histograms of geometric mean T_2 and of lung water density, as introduced here, may provide a new tool for regional and/or global characterization of pulmonary diseases. These techniques demonstrate the potential resolving power and utility of MRI in determining

lung pathology.

Chapter 7

Characterization of the Susceptibility-Induced Magnetic Field Gradient

7.1 Introduction

The magnetic field inhomogeneity induced by the heterogeneity present in biological systems is a well documented difficulty for a variety of NMR measurements [31, 86, 87]. However, this problem is more enhanced in lung tissue because of the strong susceptibility-induced magnetic field gradient near air-tissue interfaces [24, 25, 88, 89, 90]. This magnetic field discontinuity will attenuate the NMR signal which leads to a substantial decrease in the MRI image intensity. It also complicates diffusion measurements and their interpretation.

Brownian motion (which is due to the thermal energy of molecules at equilibrium) is responsible for water diffusion. Diffusion, like any other random motion in a magnetic field, results in an irreversible loss of phase coherence. The mean square displacement of molecules due to diffusion over time t is given by the Einstein relation:

$$< R^2 >= 2nDt \tag{7.1}$$

where D is the diffusion coefficient and n is the number of dimensions.

In order to gain a better understanding of diffusion measurements in lung, it is essential to comprehend the nature and behavior of the internal magnetic field gradients. It was shown that the free induction decay curve was much shorter in inflated lung than in airless lung [24, 25]

and this fast decay was explained in terms of the magnetic field shift for different lung models [25]. In later studies, T_2 decay curves were found to have a multiexponential T_2 relaxation distribution [27, 34, 79].

The outline of this chapter is as follows. First, a spherical shell model [24] was employed to estimate the magnetic field gradients in inflated lungs. Second, this estimation was used to understand the effect of the intrinsic background gradients on the T_2 distribution and to determine the inherent T_2 (i.e. excluding the diffusion effect) in lung. Third, the previous steps were used to develop an understanding for the dependence of the T_2 distribution on lung water density. Fourth, the effect of dehydration on the T_2 distribution in inflated lungs was investigated.

7.2 Theory and Model Description

Alveoli are the functional units of the lungs where the gas exchange occurs. They are polyhedral in shape and usually clustered together. Once in a magnetic field, these air cavities (alveoli) behave as magnetic dipoles and modify the magnetic field surrounding them. A simple model which describes this alveolar shape, as a first order approximation, is a spherical shell [24]; the inner sphere is filled with air and surrounded by water. Using this model (see Fig. 7.1a), the magnetic field was first calculated inside and outside a sphere by introducing a scalar potential [24, 92]. The magnetic field, to the first order approximation in χ_m is given by

$$\triangle B = \frac{2}{3}\chi_m B_0 \qquad for \qquad r < R \tag{7.2}$$

$$\triangle B = -\chi_m B_0 \frac{R^3}{r^5}(r^2 - 3Z^2) \qquad for \qquad r > R \tag{7.3}$$

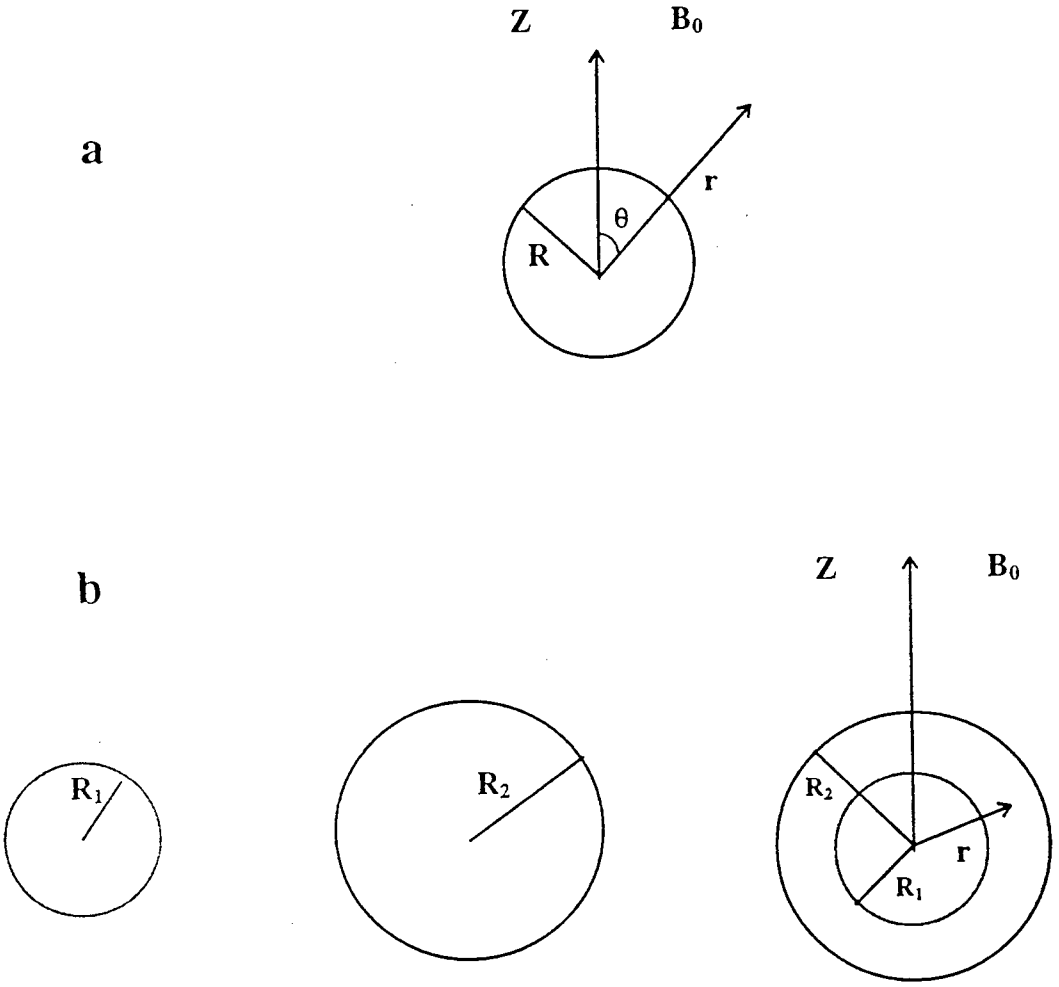

Figure 7.1: Calculation of the induced magnetic field at an arbitrary point inside and outside a sphere with a radius of R (a). The modified magnetic field within a spherical shell is obtained by subtracting the induced field outside the smaller sphere from inside the larger sphere (b).

where χ_m is the magnetic susceptibility of the material inside the sphere, R is the radius of the sphere, and r is the distance from the center of the sphere to an arbitrary point . For a spherical shell, as shown in Fig. 7.1b, the induced magnetic field is calculated by subtracting the field of the smaller sphere from the field of the larger one as defined here [24]:

$$\triangle B = -[\frac{2}{3} - \frac{R^3}{r^5}(r^2 - 3r^2\cos^2\theta)]\chi_m B_0 \tag{7.4}$$

where the spherical-coordinate equivalent of $Z = r\cos\theta$ has been substituted to simplify the equation. The gradient inside the shell is given by

$$\vec{G} = \nabla(\triangle B) = \nabla(-[\frac{2}{3} - \frac{R^3}{r^3}(1 - 3\cos^2\theta)]\chi_m B_0) \tag{7.5}$$

$$\vec{G} = -\chi_m B_0 \frac{R^3}{r^4}[(3\cos^2\theta - 1)\hat{r} + (2\sin\theta\cos\theta)\hat{\theta}] \tag{7.6}$$

where r is the distance of an arbitrary point (within the spherical shell) from the center.

The alveolar wall thickness and the radius of an alveolus are important parameters in determining the strength of the gradient. It is well known that the alveolar wall has an intricate structure and that its thickness varies considerably [93]. The reason is that the capillaries are not perfectly matched with the alveolar regions in most locations and are separated by connective tissues. This connective tissue separation has an average thickness of 2.2 μ [93, 94]. Figure 7.2 shows the thickness variation in the alveolar region. The capillaries are contained within the alveolar walls and they have an average diameter of 10 μ [93, 94]. For this reason, the thickness of the spherical shell can vary up to 12 μ in inflated lungs. Electron scanning micrography of human lung parenchyma has shown that alveolar diameters may rise as high as 150 μ. To emulate the structure of human lung tissue, average values of $R_1 = 50\mu$ and $d = 10\mu$ were incorporated into our calculation of the magnetic field gradient.

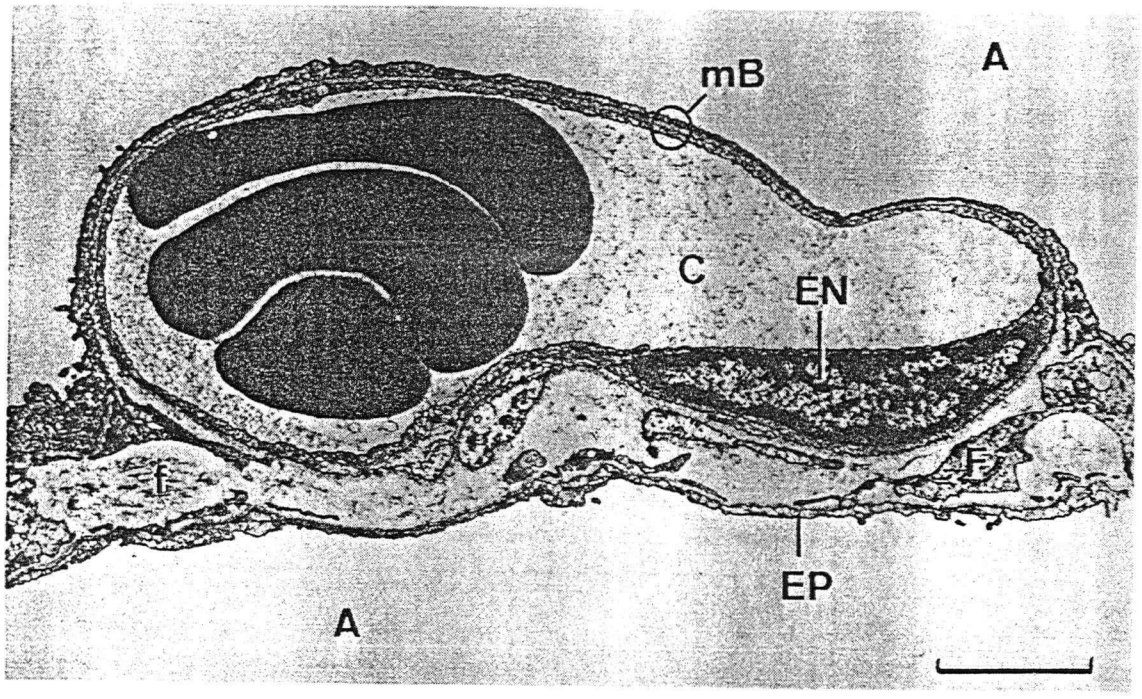

Figure 7.2: Capillary (C) in alveolar region is separated from air (A) by the tissue barrier which may or may not contain connective tissue fibers (f). EP and EN stand for epithelial and endothelial cells.

For unrestricted diffusion of spins, the resulting spin-echo attenuation is described as [45, 95]:

$$M_+(\hat{r}, 2\tau) = M_0\, e^{\frac{-2\tau}{T_2}}\, e^{-(\gamma G)^2 D \frac{2\tau^3}{3}}. \tag{7.7}$$

As shown in the above equation, the effect of the gradient on spin-echo attenuation is dependent upon G^2. In Fig. 7.3 a 3D mesh plot of G^2 (using Eqn. [7.6]) is depicted on the r and θ plane within the spherical shell for a constant wall volume of $3.81 \times 10^{-7} cm^3$ and the inner radius of 50μ which corresponds to lung water density of about 0.42 g/ml. This constraint was imposed in accordance with the mass-conservation principle. This means that during pulmonary ventilation

(inspiration and/or expiration) as the lung alveolar radius changes, the alveolar volume remains constant. Figure 7.4 shows a plot of G^2 at an arbitrary point within the spherical shell region as a function of the inner radius for a constant volume of $3.81 \times 10^{-7} cm^3$. A peak was observed at $\dot{R}_1 \approx 68\mu$ for all angles. The estimated value of G^2 along with Eqn. [7.7] was used to determine the signal attenuation.

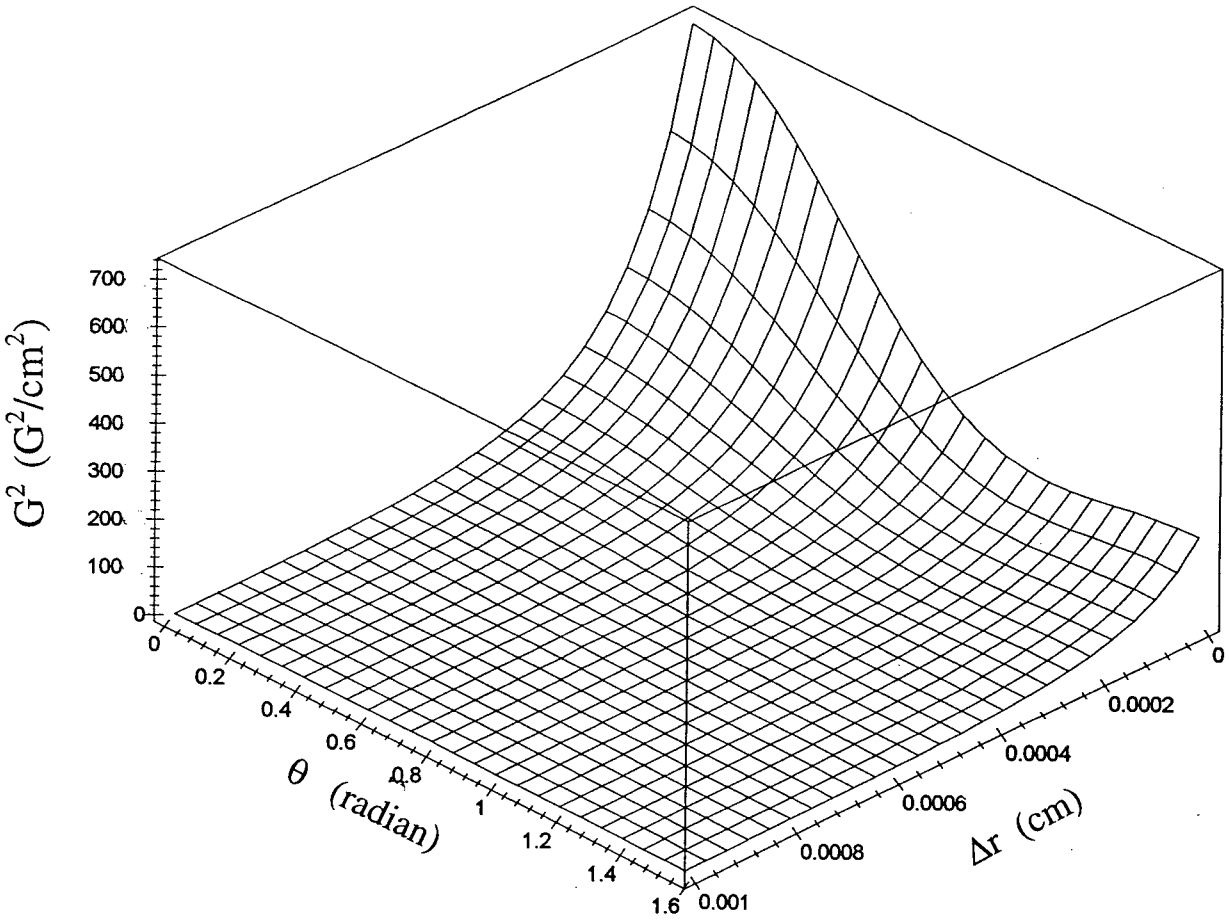

Figure 7.3: The surface map of the G^2 (susceptibility-induced magnetic field gradient) as a function of $\triangle r$ and θ within the spherical shell for a constant volume ($3.81 \times 10^{-7} cm^3$) with $R_1 = 50\mu$ and $\rho = 0.42 g/ml$.

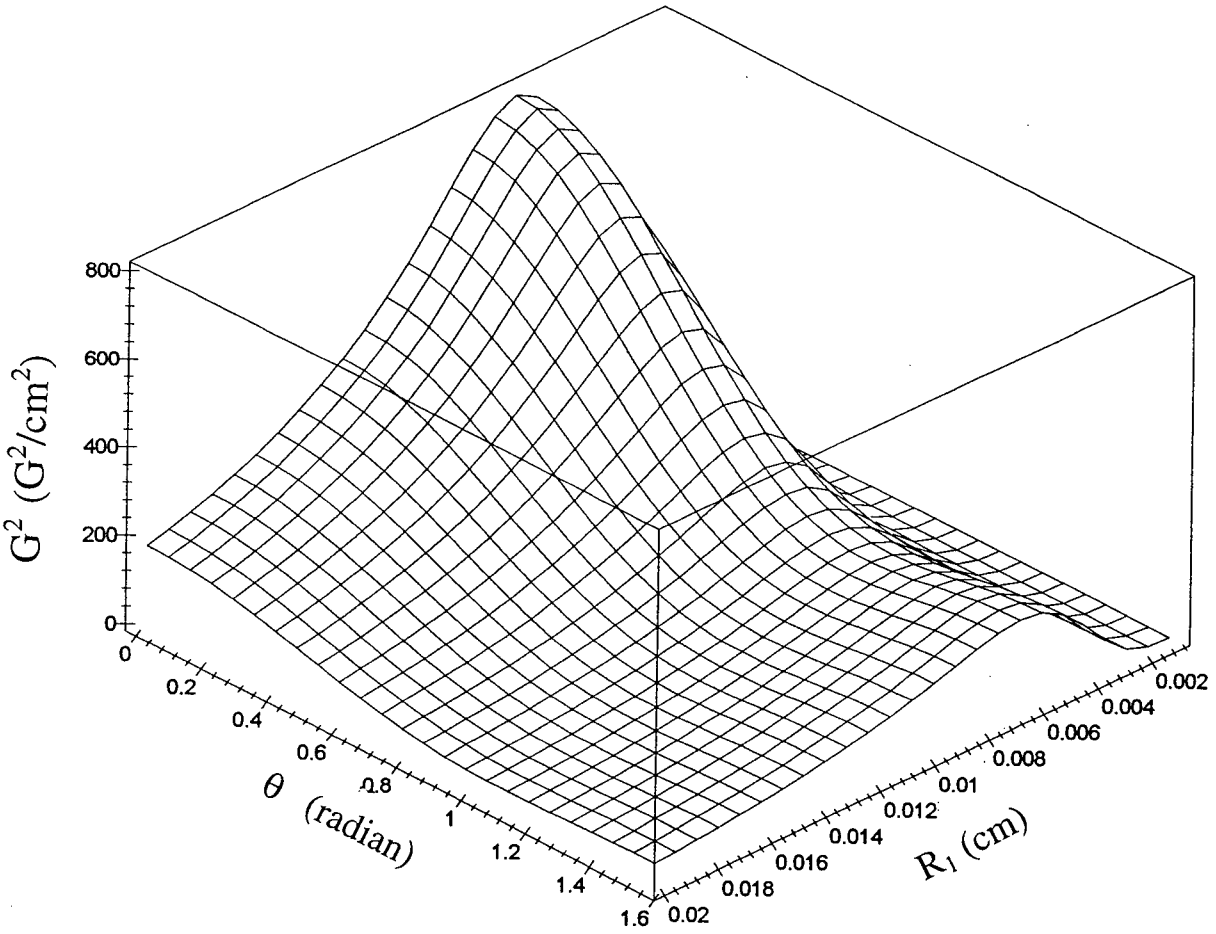

Figure 7.4: The surface map of the G^2 (susceptibility-induced magnetic field gradient) as a function of inner radius R_1 and θ for a constant volume ($3.81 \times 10^{-7} cm^3$). A peak was observed at $R_1 \approx 68\mu$ for all angles. This volume configuration corresponds to $\rho \approx 0.22 g/ml$.

For the spherical shell model with an inner radius of R_1 and outer radius of R_2, the lung-water density is given by

$$\rho_l = \frac{\rho_a . V_a + \rho_w . V_w}{V_a + V_w} \tag{7.8}$$

where V_a and V_w are the volumes occupied by air and water and ρ_l, ρ_a, and ρ_w are the lung-water density, air density and water density, respectively. To relate this equation to NMR measurements, ρ_a, was set to zero since vapor H_2O has negligible contribution to MRI signal intensity. This yields:

$$\rho_l = \frac{\rho_w . \int_{R_1}^{R_2} 4\pi r^2 dr}{\int_0^{R_2} 4\pi r^2 dr}. \tag{7.9}$$

In Fig. 7.5 the lung water density is depicted as a function of R_1 for a fixed volume of $V = 3.81 \times 10^{-7} cm^3$. The lung-water density along with the modeling of alveolar regions and G^2 estimation were used to analyze and elucidate the complex T_2 distribution in lung.

7.3 Experimental

MRI studies were performed on 12 lungs from healthy juvenile pigs and the MRI measurements were carried out on a 1.5 T GE Signa MRI scanner. The detail of the sample preparation and MRI measurements were explained in chapter 5 and 6.

7.3.1 Simulation

A simulation was performed to assess the effect of diffusion alone on the T_2 relaxation decay curves. To accomplish this task, the signal intensity was averaged over all possible positions

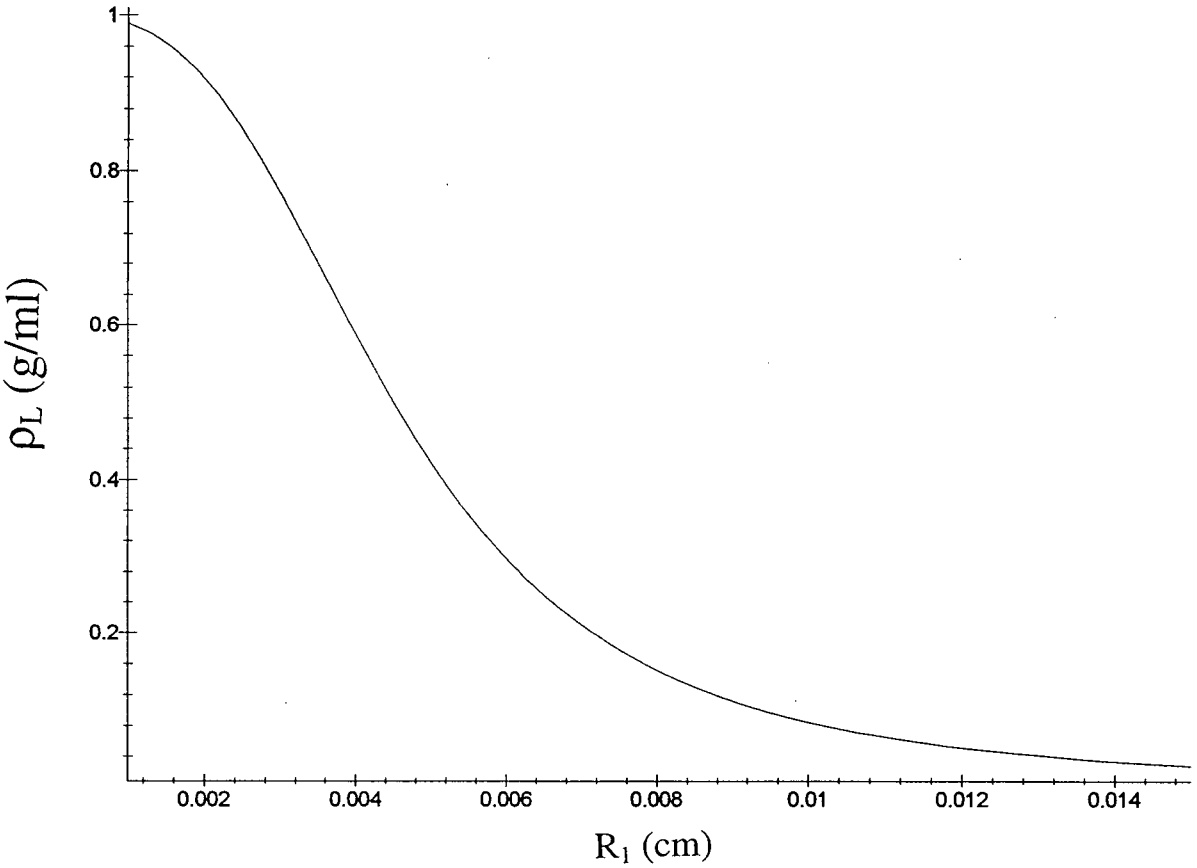

Figure 7.5: The lung-water density plotted as a function of R_1 for $V = 3.81 \times 10^{-7} cm^3$.

within the spherical region using the following equation:

$$S(\vec{r}, nTE) = \frac{S_0 \int_v e^{-(\gamma G)^2 Dn \frac{TE^3}{12}} dv}{\int_v dv}. \tag{7.10}$$

with D=$10^{-5} cm^2/s$ (this value was obtained from our diffusion measurements and discussed in chapter 8), TE is the echo spacing and set to 10 ms, and n is the number of echoes. The value of n was varied between 1 and 16 to produce magnetization decay curves for a given volume. By using the above equation, two assumptions were made implicitly. (1) The field gradient experienced by each water molecule does not change appreciably within the TE time

of 10 ms. (2) The diffusion is unrestricted over the TE time. According to Eqn. [7.1], water molecules cover approximately a distance of 4 μ in 10 ms. As a result, the second condition definitely holds for low TE values. Also within this distance, the changes in the magnetic field gradients are minimal for most locations within the shell. Decay curves from Eqn. [7.10] were analyzed to obtain T_2 distributions and the subsequent geometric mean T_2 values, using the NNLS algorithm. Finally, the generated decay curves obtained from Eqn. [7.10] were employed to fit the measured decay curves by taking into account the inherent T_2 relaxation property of the lung tissue (i.e. excluding the diffusion attenuation). To do so, the following steps were taken: (1) A VOI was selected from a lung image and a decay curve and its corresponding MRI lung water density were produced. (2) A specific spherical shell volume was chosen which provided us with a water density value in the vicinity of the measured value. (3) The following equation

$$S(\vec{r}, nTE) = e^{\frac{-nTE}{T_2}} \times \frac{S_0 \int_v e^{-(\gamma G)^2 Dn \frac{TE^3}{12}} dv}{\int_v dv} \tag{7.11}$$

was fitted to the observed decay curve (with only one parameter, T_2) and a nonlinear functional optimization program [58] was employed to minimize the χ^2 misfit. Note the above equation explicitly assumes that the inherent T_2 decay is monoexponential. For a given volume, the lung water density for the simulated decay curve was obtained from Eqn. [7.9].

7.4 Results and Discussion

7.4.1 Relaxation Analyses

In Fig. 6.1, representative sagittal images of the left and right lungs were depicted. The T_2 distribution was globally determined for each lung by deriving the T_2 magnetization decay curves for each voxel. Figure 6.4 showed a representative decay curve from a voxel (in inflated lung) with $\rho_l \approx 0.3g/ml$ and Fig. 6.5 plotted its respective smooth T_2 distribution. After obtaining the T_2 distribution, the geometric mean T_2 was calculated using

$$GMT_2 = exp[\int_{0.01}^{5} S(T_2)\, logT_2\, dT_2/(\int_{0.01}^{5} S(T_2)\, dT_2)] \tag{7.12}$$

Since T_2 relaxation times are related to the biological environment, a joint representation of the lung-water density and GM T_2 was employed. Figure 7.6a shows the distribution of the lung-water density as a function of the GM T_2 distribution from a healthy inflated lung. This distribution was similar to a hockey stick in shape and exhibited two distinct regions. The lower part of the distribution (lung density between 0 and 0.4 g/ml) contained a cluster of GM T_2 values (+ marker in Fig. 7.6a) ranging between approximately 15 and 65 ms with its average around 32 ms. As the lung-water density increased, the GM T_2 seemingly increased. On the other hand, the upper portion of the distribution (density of 0.4 g/m and higher) had a narrower range of GM T_2, between 55 and 90 ms (Fig. 7.6a). Moreover, The GM T_2 was proportional to the lung water density, however, its slope was much steeper than that of the lower part of the distribution.

To have a better understanding of the origin of this GM T_2 distribution and its shape, the lung was decomposed into 2 regions (see Fig. 7.6a): (1) the inflated part. (2) the partially or

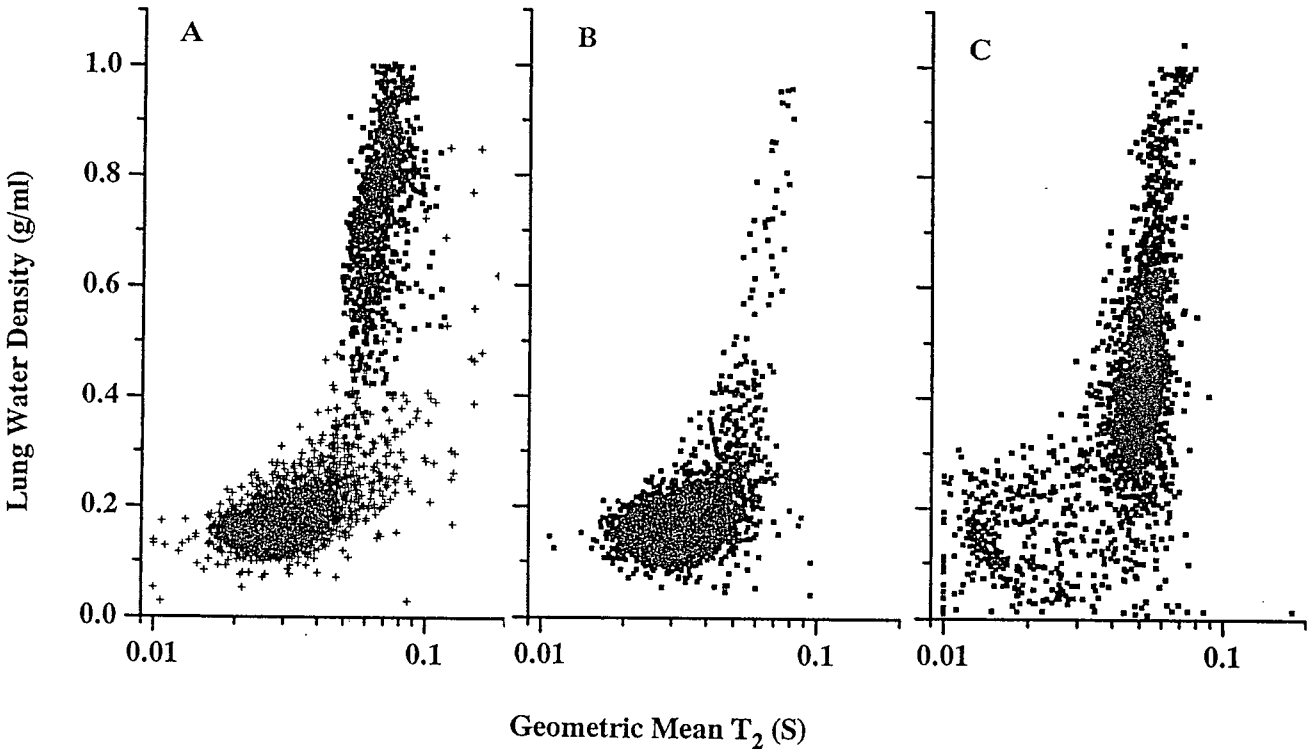

Figure 7.6: Lung water density plotted as a function of geometric mean T_2 for all voxels at different hydration levels. (A) For the fresh lungs (wet/dry = 3.96), there were 2 distinct regions, inflated (+) and collapsed (solid □). The shape of the total distribution looks like a hockey stick with the sharp curve near 0.4 g/ml. (B) As dehydration proceeded (wet/dry = 3.74), the threshold density (0.4 g/ml) and the shape of the distribution remained unchanged. (C) For the highest dehydration level (wet/dry = 3.16), the average GM mean T_2 shifted towards shorter values, nevertheless, the shape and threshold density were still fixed.

fully collapsed part. After this decomposition, each of these areas was analyzed separately. This approach helped us to establish a direct correlation between the location of each voxel and its GM T_2 time. The low values of GM T_2 came from the portion where the lung was inflated and consequently have low lung-water densities (+ marker). The rest of the distribution originated largely from the collapsed region (solid □). These two regions were separated by a threshold lung-water density of approximately 0.4 g/ml.

7.4.2 Dehydration Effects

To monitor the GM T_2 and investigate its relationship with alteration in water content, four lungs were dehydrated incrementally. Figures 7.6b, and 7.6c show the evolution of the GM T_2 distribution with respect to the incremental dehydration. Seemingly, the water loss began from the regions with high water density and trimmed the edges of the GM T_2 values in those regions. For the lowest hydration level , the lung water density was mostly concentrated near 0.4 g/ml and above because of the shrinkage in volume.

For all hydration levels, the shape of the GM T_2-density curve distribution remained unchanged and the threshold lung-water density (separating the two regimes) was the same. This indicated that the relationship between GM $T_2$and lung water density is independent of the hydration level, a phenomenon not reported previously.

7.4.3 Simulation Analysis

Five different volume configurations ($1.55 \times 10^{-7}, 2.55 \times 10^{-7}, 3.81 \times 10^{-7}, 5.32 \times 10^{-7}, 7.08 \times 10^{-7} cm^3$) for the spherical shell model corresponding to inner radii of 30, 40, 50, 60, and

70 μ were selected. For each volume, when the inner radius was changed, the shell volume remained constant (i.e. the wall thickness changed). The water density was estimated for each configuration and the simulated decay curves were generated. A T_2 distribution and GM T_2 value were derived from each curve. Figure 7.7 shows a T_2 distribution for $3.81 \times 10^{-7} cm^3$ with $R_1 = 57\mu$ which corresponds to $\rho \approx 0.3 g/ml$. It is interesting to note that this distribution qualitatively replicates the T_2 distributions obtained from the measured decay curves (see Fig. 6.5).

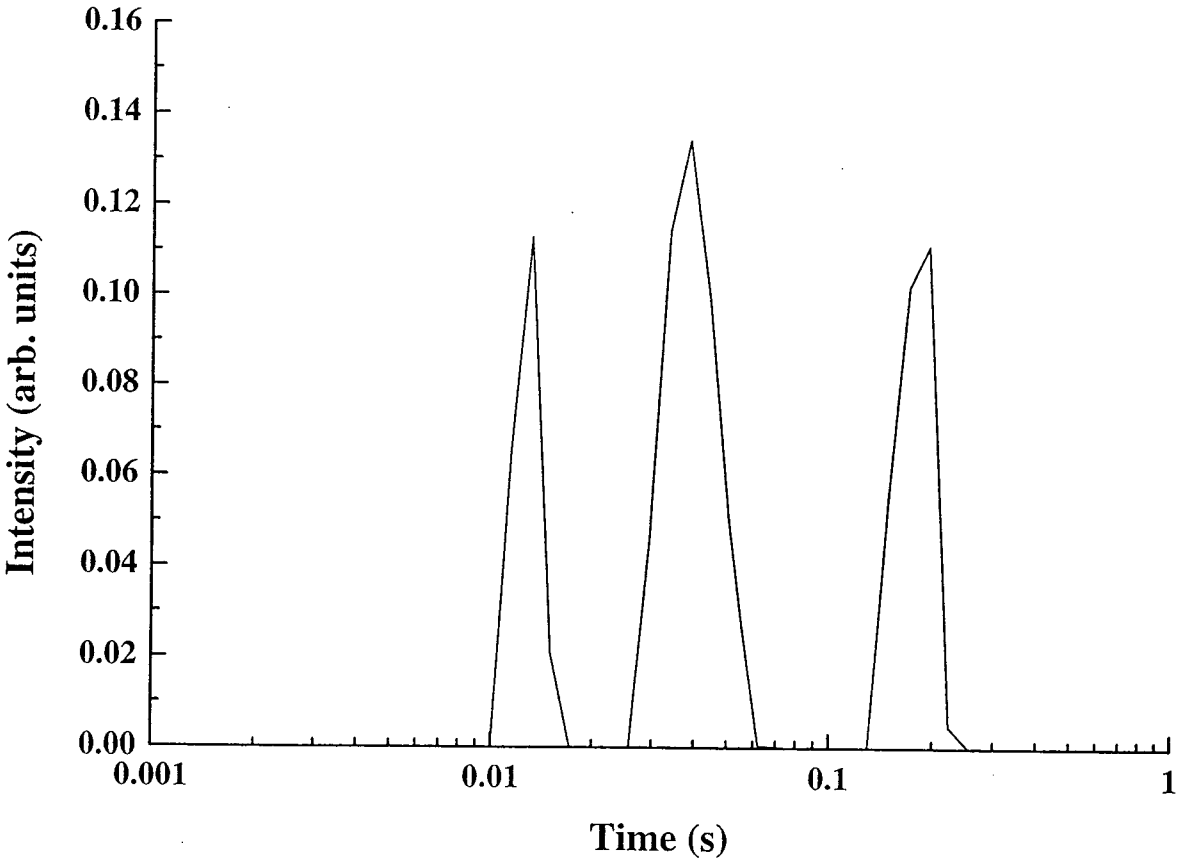

Figure 7.7: The simulated smooth T_2 distribution from a spherical shell with a volume of V=$3.81 \times 10^{-7} cm^3$ with the inner radius of 57 μ and $\rho \approx$)$0.3 g/ml$.

Although previous studies have demonstrated the multiexponential nature of the T_2 distribution in the lung tissue, none has suggested a clear mechanism for such a characteristic. Compartmentalization has been proposed as one of the possible mechanisms to account for this behaviour in other biological systems. To have a better understanding of this particular T_2 distribution (Fig. 7.7) and the origin of these peaks, Eqn. 7.10 (with G constant) was used for a wide range of G's and decay curves were generated. Using the NNLS method, the T_2 distribution was determined for each decay curve. For low values of G, two peaks were observed, one with a short T_2 time greater than 30 ms and the other one greater than 200 ms. As the gradient was increased, these two peaks were shifted towards lower values. On the other hand, for large values of G, only one peak was obtained which was between 10 and 20 ms. This analysis suggests that the short T_2 value corresponds to regions with high values of G and the longest T_2 corresponds to regions with lowest G. In the shell model, the highest G's experienced by water molecules are at $\theta = 0^0$ (parallel to the main field) the lowest G's are at and $\theta = 90^0$ (perpendicular to the main field). This demonstrates that diffusion (alone) of water molecules in a field gradient can produce such T_2 distributions in lung.

Figure 7.8 shows the water density depicted as a function of GM T_2 for a given shell with $3.81 \times 10^{-7} cm^3$ volume. This plot featured the same characteristics as in Fig. 7.6a. As the density decreased, the GM T_2 decreased slowly, up to $\rho_l \approx 0.5 g/ml$. A sharp change of GM T_2 was noticed around $\rho_l \approx 0.45 g/ml$. This density corresponded to a volume configuration with $R_1 = 51\mu$ and d=9 μ (Fig. 7.4). For shells with water density less than 0.4 g/ml, the diffusing water molecules experienced the strongest gradients. As a result, the T_2 magnetization decay curve steepened and led to shorter GM T_2 times. All these characteristics mentioned

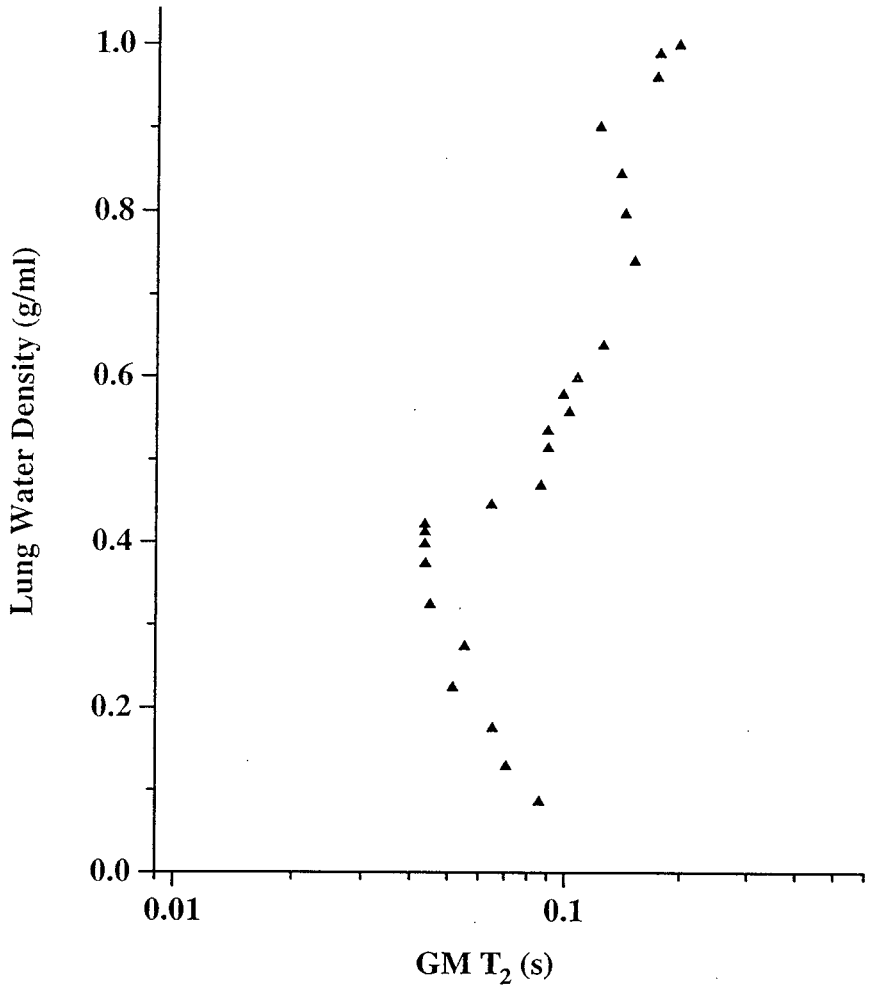

Figure 7.8: Simulated estimation of the lung water density as a function of GM T_2 for a spherical shell model with V=3.81 $\times$ $10^{-7}cm^3$ and inner radius ranging between 10 μ and 140 μ.

above, indicated that the spherical shell model (even though relatively simple) could explain this particular distribution of the GM T_2 values as a function of lung water density.

The same plots were made for other volume configurations and the following observations were noticed. As the volume of the shell increased, the threshold water density slowly increased from about 0.4 to 0.5 g/ml and the GM T_2 times were shifted towards larger values. However, the shape of the hockey-stick distribution remained unchanged.

7.4.4 Inherent T_2 measurements

Nine VOI's from *in vitro* lung images with lung water densities ranging from about 0.2 to 0.9 g/ml were selected and their T_2 magnetization decay curves were extracted. For example, a decay curve from a voxel with $\rho_l \approx 0.3g/ml$ was (obtained from the data) taken as a representative. A shell volume configuration of V= $3.81 \times 10^{-7} cm^3$ with the inner radius of 57 μ which corresponds to $\rho \approx 0.3g/ml$ was selected to produce the simulated decay curve due to diffusion alone. This curve along with Eqn [7.11] was fitted to the corresponding measured curve. A nonlinear algorithm (23) was employed to determine the only parameter, T_2. The results of this fitting is shown in Fig. 7.9 and the inherent T_2 value obtained for this particular fit was 174 ms. This approach definitely demonstrates the feasibility of measuring the inherent T_2 relaxation time of lung tissue and its relationship with the lung water density.

Figure 7.9 also shows 2 other fittings to decay curves with $\rho \approx 0.2, 0.9g/ml$. The obtained T_2 values were 116 and 527 ms, respectively. This indicated that the inherent T_2 time was a function of the lung water density. The same procedure was applied for other shell volumes mentioned in the previous section. However, the spherical shell volume of $3.81 \times 10^{-7} cm^3$ gave the lowest χ^2 misfit values. Besides, this volume was in agreement with the morphometrical studies of lungs. In Fig. 7.10, the inherent T_2 values are depicted as a function of lung water density.

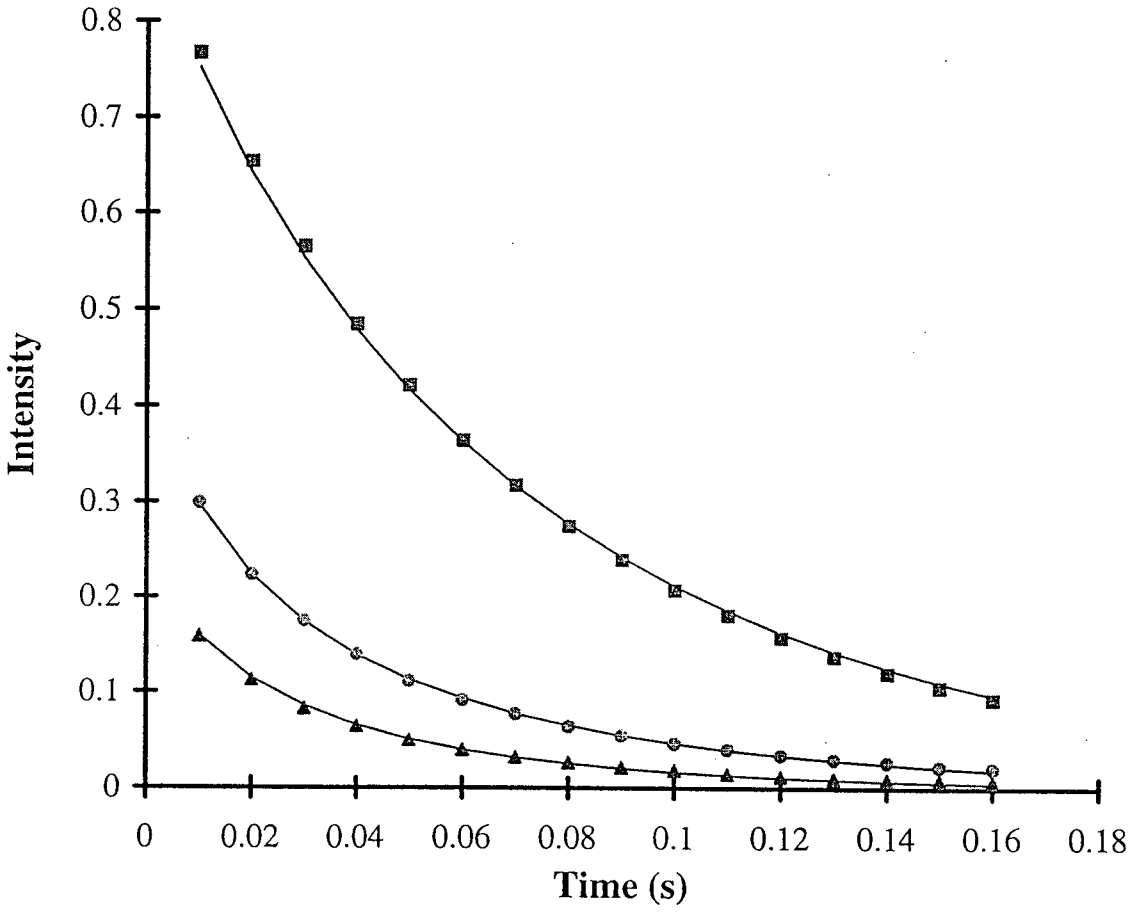

Figure 7.9: T_2 magnetization decay curves in inflated pig lungs measured with the sixteen echo-pulse sequence. Three different VOI's with the lung water densities of 0.2 g/ml (solid △), 0.3 g/ml (solid ○), and 0.9 g/ml (solid □) were selected. Solid lines are the fits to decay curves using Eqn. [7.11] and the inherent T_2 values were obtained from these fittings.

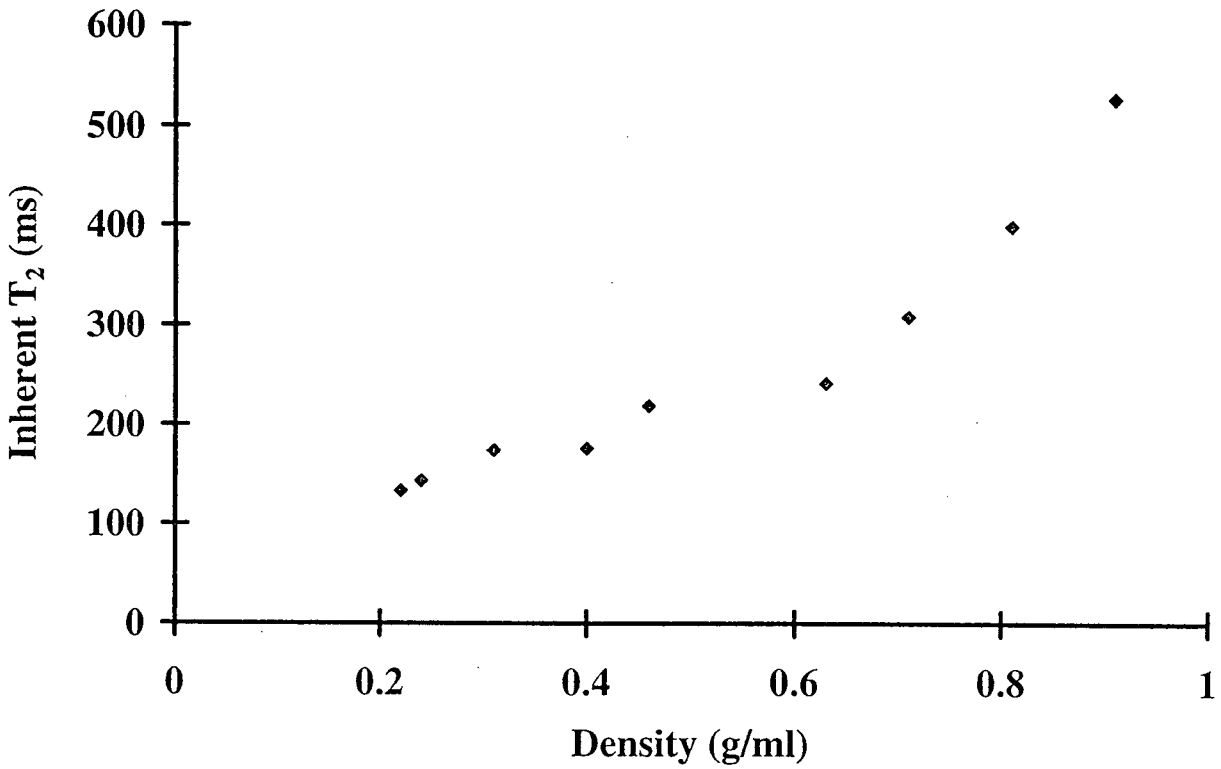

Figure 7.10: The inherent T_2 relaxation times plotted as a function of lung water density.

7.5 Conclusion

Even though the inhomogeneity in the magnetic field distorts the NMR signal obtained from biological tissues, this effect could be regarded as an opportunity to extract structural information. By carefully examining the decay curves obtained from MR images and fitting them by simulated curves (Eqn. [7.11]), we have found specific spherical shell configurations could give optimal fits. This indicated that MRI could potentially provide us with the geometry and sizes of the alveoli. The measurement of the inherent T_2 in the lung tissue and its relationship with

the water density also can be used as a monitoring device for regional assessments. In summary, all this information may provide us with a helpful diagnostic guide and could lead to a deeper understanding of the underlying processes responsible for the pathological and physiological states of tissue.

Chapter 8

Measurements of the Self-diffusion Coefficient in Lung

8.1 Introduction

Heterogeneity, at a variety of levels, is essential to the functioning of living organisms and some aspects of this phenomenon can be studied non-invasively by NMR. This effect, in biological systems, imposes inhomogeneity in the magnetic field within the sample. However, in lung, the more dominant inhomogeneous magnetic fields are induced by spatial variations of the magnetic susceptibility between air-soft tissue interfaces. The translational motion of spins (diffusion) introduces temporal variation in the magnetic field experienced by any nucleus. Since the motion is random and irregular, the temporal variation is not identical in different periods of time. This gives rise to a spatial distribution of nonlinear internal magnetic field gradients and the amplitudes of the spin echoes are modified by molecular diffusion in these magnetic field gradients.

Another important characteristic of biological tissues (i.e. lung) is that water molecules are confined to well defined volumes due to the complex structure of cells. If diffusion is measured over a short enough time, very few diffusing molecules experience the effect of barriers. On the other hand, if the time of observation is extended, water molecules are reflected or slowed down at barriers. As a result, diffusion should depend on the permeability and geometric

arrangements of barriers.

The effect of molecular diffusion on magnetization in an inhomogeneous field with a linear static magnetic field gradient $\vec{G}$ was incorporated into the Bloch equations by Carr, Purcell and Torrey [47, 97]. This important and crucial prediction of additional attenuation led to the application of the CPMG pulse sequence and development of the pulsed field gradient (PFG) technique [43] which are both capable of measuring the self-diffusion coefficient of spin-bearing species. In these methods, the magnetic field gradient is a known parameter and it is controlled by the experiment. However, in a heterogeneous system such as lung tissue the distribution of the intrinsic magnetic field is not well known.

The pulsed-field gradient technique is a version of the original Hahn-spin echo [41] modified by applying two equivalent gradient pulses on either side of the 180^0 pulse. The PFG technique has been widely used to study restricted diffusion [96, 97, 98] and observe anisotropic diffusion [99, 100]. Another approach is the Carr-Purcell method [42] and is theoretically capable of eliminating the diffusion effect as the time between 180^0 pulses approaches zero.

The use of the PFG method in lung tissue introduces cross terms [36, 101] between the applied and the internal magnetic field gradients. This makes the diffusion measurement and its interpretation complex [101]. Pulse sequences [53, 98, 102, 103] have been developed in order to control or eliminate the cross term. These pulse sequences were used to measure the diffusion coefficient in systems such as apples which mimic the lung-tissue structure. The reported internal magnetic field ($\sqrt{< G^2 >}$) in apples was measured to be 8.9 G/cm [101].

According to the spherical shell model (Fig. 7.3), the maximum gradients experienced by water molecules are about 30 G/cm which is at least an order of magnitude greater than the

imaging gradients. In previous studies [26, 34, 35], the PFG method was employed to determine the diffusion coefficient in excised rat lung. Their findings indicated D was dependent on diffusion time. However, the coupling between the applied and internal magnetic field gradient was not accounted for.

This chapter is focused on measurements of the apparent diffusion coefficient in the presence of the inherently inhomogeneous magnetic field in lung using a clinical imager. To accomplish this goal, the internal magnetic field gradient was first characterized using a spherical shell model [24]. Then the CPMG technique was employed to measure D and investigate its dependence on time.

8.2 Model Description and Experimental

A spherical shell model was employed to estimate the magnetic field gradients. This model was explained in the previous chapter in detail. The magnetic field and the field gradients were estimated within the shell region. MRI studies were performed on 12 lungs from healthy juvenile pigs. The sample preparation was discussed elsewhere (see chapter 6). MRI measurements were carried out on a 1.5 T GE Signa MRI scanner.

8.2.1 Diffusion Measurements

The diffusion coefficient can be estimated using the CPMG equation

$$S(\vec{r}, nTE) = S_0\, e^{\frac{-nTE}{T_2}} e^{-(\gamma G)^2 D \frac{nTE^3}{12}}. \tag{8.1}$$

where S_0 the signal intensity at zero time, γ is the gyromagnetic ratio, G is the field gradient, and TE is the echo spacing. It is important to note that the relative contribution of the diffusion

term compared to the T_2 term depends upon the echo spacing. Two different approaches can be taken to measure the diffusion coefficient using Eqn. [8.1].

(a) If the echo spacing is made very short, the attenuation due to diffusion processes should be negligible. This constraint reduces Eqn. [8.1] to the first term. Decay curves obtained from VOI's selected from images could be fitted to an exponential fitting routine and S_0 and T_2 values could be estimated. If S_0 and T_2 are known, D can be obtained from the Hahn echo equation. However, it is not trivial to obtain the inherent T_2 relaxation time. It is important to note that in the previous chapter a value of $10^{-5} cm^2/s$ was assumed for the diffusion coefficient. In principle, one could carry out a CPMG measurement at very short echo spacing, however, our MRI CPMG system was limited to the echo spacing of 10 ms.

(b) To eliminate the uncertainty involved in determining S_0 and T_2 values, the number of echoes, n, and echo spacing can be chosen in such a way that their products (nTE) remain fixed. Keeping (nTE) constant allows us to compare different numbers of echoes in the multiecho train at a fixed imaging time. For this set of experiments, nTE was fixed at 60 ms with n=1, 2, 3, 4, 5, 6. Using this approach, we can vary the factor involving diffusion while the T_2 weighting remains constant. This is advantageous because there is no need to know S_0 or T_2. Therefore, they can be eliminated from the CPMG diffusion equation by comparing signals obtained at different values of n, using

$$\frac{S(n_{max}TE_{min})}{S(nTE)} = e^{\frac{-n_{max}TE_{min}}{12}(\gamma G)^2 DTE_{min}^2} / e^{\frac{-nTE}{12}(\gamma G)^2 DTE^2}. \tag{8.2}$$

Taking the natural logarithm of both sides of the above equation yields:

$$Ln(\frac{S(n_{max}TE_{min})}{S(nTE)}) = -\frac{n_{max}TE_{min}}{12}(\gamma G)^2 DTE_{min}^2 + \frac{nTE}{12}(\gamma G)^2 DTE^2. \tag{8.3}$$

In this study, the latter approach was taken to measure D. The outline of the method is as follows. First a VOI was selected and the decay curve was extracted. Second, the echo attenuation for different combinations of the product nTE were measured. Third, these echo attenuations were compared and fitted by Eqn. [8.3] to obtain D, using a nonlinear fitting routine [58].

8.3 Results and Discussion

In Fig. 8.1 the logarithm of the ratio of echo attenuations plotted as a function of the square of the echo spacing time. These ratios were obtained using Eqn. [8.3]. The data clearly deviate from the linear dependence which would indicate a constant diffusion coefficient for an unrestricted and isotropic process. Using the spherical shell model with a constant volume ($V = 3.81 \times 10^{-7} cm^3$) along with Eqn. [7.6] were employed to fit Eqn. [8.3] to the data. A nonlinear fitting algorithm [58] was applied to obtain the apparent diffusion coefficients. Figure 8.2 shows the measured diffusion coefficients as a function of echo spacing. The apparent diffusion coefficient decreased from about $1.0 \times 10^{-5} cm^2/s$ to $1.7 \times 10^{-6} cm^2/s$ as the diffusion time increased from 12 to 60 ms. As the data suggest, for very short diffusion times, the apparent diffusion converges to the value of the self-diffusion coefficient for free water.

This result is similar to measurements performed by Wayne and Cotts [104]. In that study, the effect of diffusion on the NMR signal in finite samples was investigated, using the CPMG technique. Their findings indicated that for very short τ values, the apparent diffusion coefficient was the same as the self-diffusion coefficient for water. However, as the diffusion time increased, the apparent diffusion coefficient decreased.

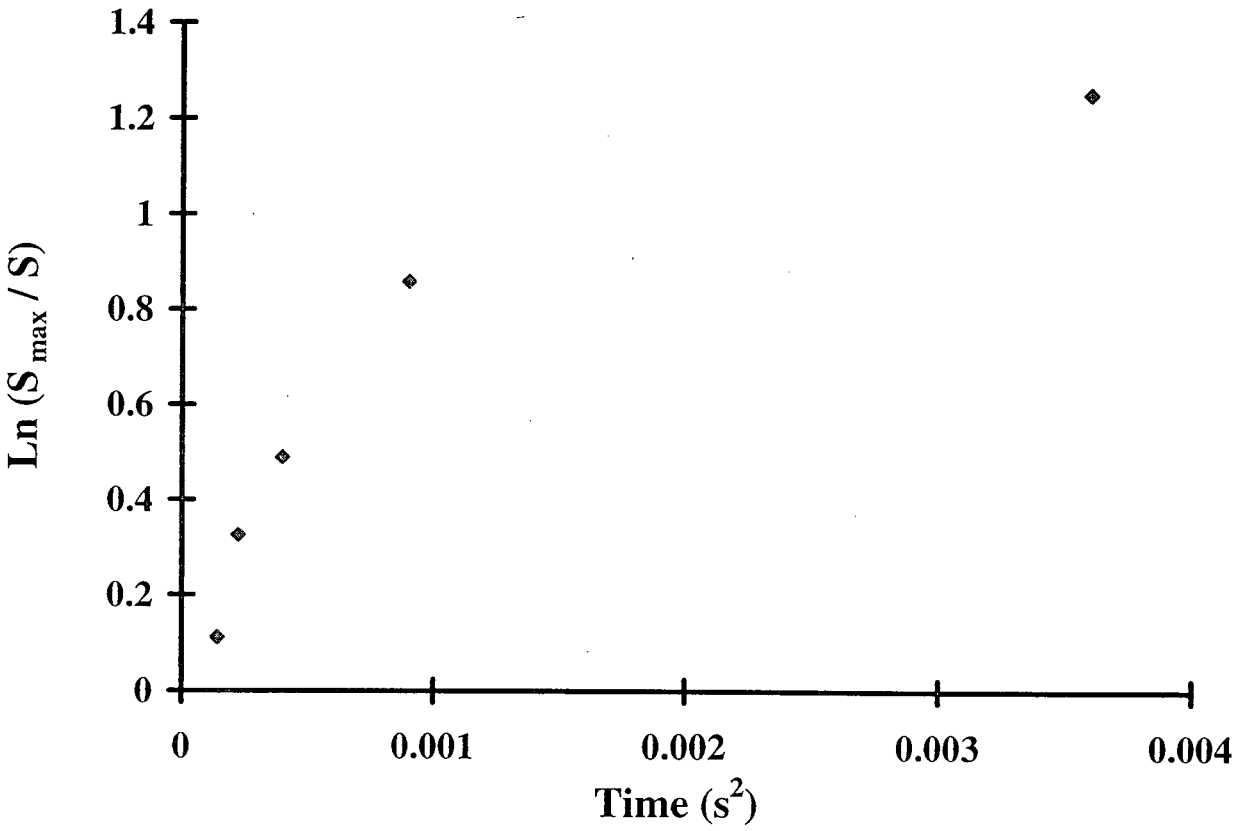

Figure 8.1: The logarithm of the ratio of different echo attenuations plotted as a function of the square of the echo spacing.

Using Eqn. [8.1] implicitly assumes that the gradients experienced by each nucleus are linear and fixed within the echo spacing time. As shown in Fig. 7.3, this assumption partially holds for a vast majority of locations within the spherical shell region, Also, note that below echo spacings of about 15 ms, the echo attenuation is solely due to unrestricted diffusion—the distance covered by water molecules in 15 ms is about 6μ which is within the range of the alveolar wall thickness. As the observation time is extended, the dephasing effects due to the field gradient for individual spins can change. The reason is that the value of root mean square distance covered by water molecules (see Eqn. [7.1]) becomes several times larger than

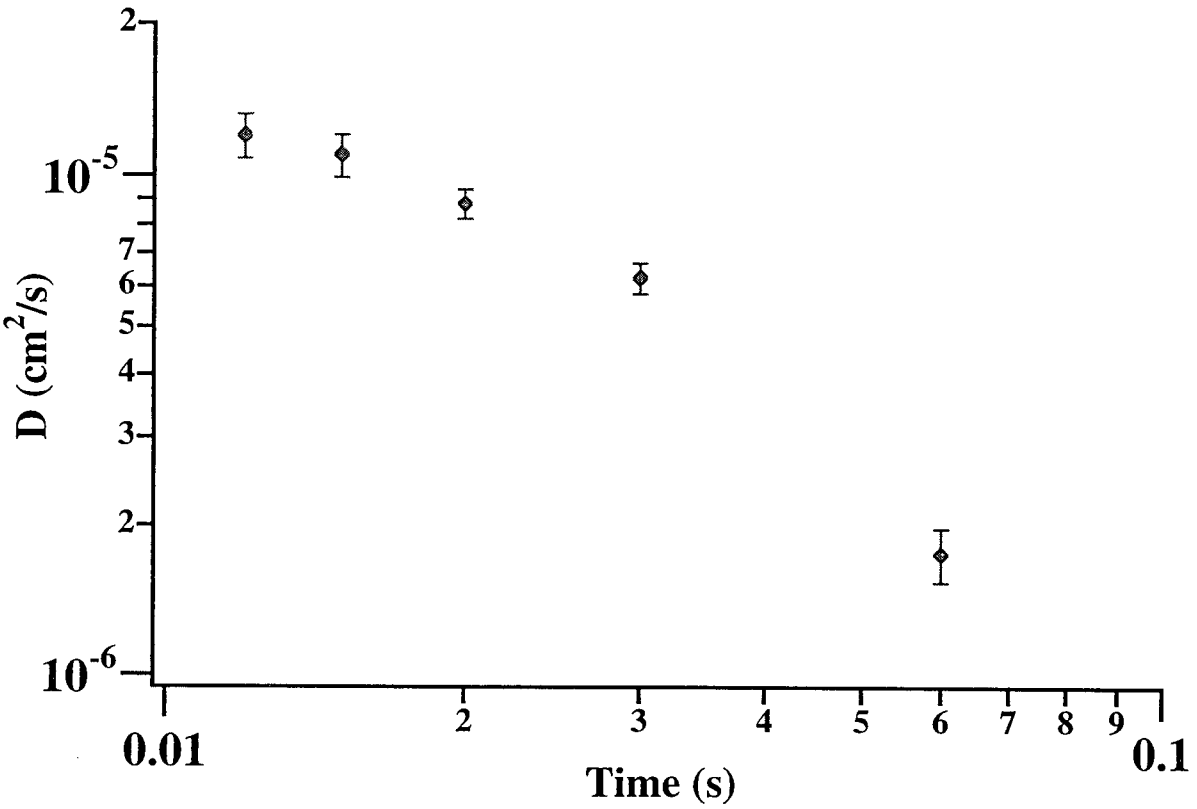

Figure 8.2: The apparent diffusion coefficient decreased from $1.1 \times 10^{-5} cm^2/s$ to $1.7 \times 10^{-6} cm^2/s$ as the diffusion time increased from 12 to 60 ms.

the alveolar thickness. For this reason, at sufficiently long echo spacing, the effects of restricted diffusion and diffusion in changing field gradients are tangled and cannot be distinguished.

To explain this in more detail, let us consider a system which consists of two water reservoirs (containing the same amount of water) experiencing two different gradients in the z direction, G_1 and G_2. According to Eqn. [8.1], the signal intensity for each water reservoir decays as a function of $e^{-(\gamma G)^2 D \frac{nTE^3}{12}}$, neglecting the T_2 effect. The total signal intensity from water

molecules will be obtained by summing up the signals from all reservoirs:

$$S(\vec{r}, nTE) = \frac{S_0}{2}[e^{-\gamma^2 G_1^2 D\frac{nTE^3}{12}} + e^{-\gamma^2 G_2^2 D\frac{nTE^3}{12}}]. \tag{8.4}$$

Writing G_1^2 and G_2^2 as:

$$G_1^2 = G^2 + (\triangle G)^2 \tag{8.5}$$

$$G_2^2 = G^2 - (\triangle G)^2. \tag{8.6}$$

and combining Eqn. [8.4], Eqn. [8.5], and Eqn. [8.6] will yield:

$$S(\vec{r}, nTE) = \frac{S_0}{2} e^{-\gamma^2 G^2 D\frac{nTE^3}{12}}[e^{-\gamma^2 (\triangle G)^2 D\frac{nTE^3}{12}} + e^{\gamma^2 (\triangle G)^2 D\frac{nTE^3}{12}}]. \tag{8.7}$$

The term in brackets is a hyperbolic Cosh function which is the dominating factor for long TE times. For this reason, the effect of restricted diffusion and diffusion in a distribution of field gradients can not be distinguished easily at long TE time.

In a previous study performed by Kveder *et al.* (using the PFG technique) a decrease in the apparent diffusion coefficient from $4.0 \times 10^{-6} cm^2/s$ to $1.3 \times 10^{-6} cm^2/s$ was measured as the time increased from 5 to 50 ms [26, 34]. Unfortunately, the magnetic field strength, at which measurements were done, was not mentioned. As we know, the internal magnetic field gradients are dependent upon the external applied fields. Later studies by Zhong *et al.* measured the apparent diffusion coefficient, using the same technique, at 2T. Their findings indicated a decrease in D from about $4.6 \times 10^{-6} cm^2/s$ to $0.1 \times 10^{-6} cm^2/s$ as the time increased from 15 to 85 ms [35]. However, in both studies the coupling between the applied and internal magnetic field gradient was not accounted for. In a more recent study by Laicher *et al.* [36], the applied and internal gradients were decoupled and it was found that D remained constant

($4.6 \times 10^{-6} cm^2/s$) as time increased from 18 to 106 ms. However, in the same study [36], it was reported that the Ultra High Static field Gradient (UMG) indicated a decrease in the apparent diffusion coefficient with increasing time.

It is important to note that in our method, measurements were performed on inflated lungs with inflation pressure of 10 cm H_2O compared to previous studies [26, 34] which were done on excised lung tissue (relatively deflated). Also, our diffusion measurements were performed at 1.5T which translates into lower internal magnetic field gradients and minimal applied MRI magnetic field gradients ($\ll 1G/cm$) were applied.

Chapter 9

Concluding Remarks and Future Direction

9.1 A Final Word

In vitro NMR experiments on excised lung tissues followed by measurements on inflated lungs (using a clinical MRI scanner) demonstrated that MRI is capable of measuring lung water content accurately. Our studies have reduced uncertainties involved in measuring water content from 15-20% (reported by previous studies) to 5%.

T_2 relaxation time measurements on inflated lungs were able to detect the longer T_2 component which was not observed in previous studies [28, 29]. More importantly, regional variations of the T_2 distribution were characterized (by a voxel-by-voxel analysis of images) as a function of lung water density. This T_2-density curve had a particular shape which was found to be independent of hydration level, a phenomenon not reported previously.

The estimation of the internal magnetic field gradients along with simulated diffusion decay curves helped to assess the effect of diffusion alone on the T_2 magnetization decay curve. This approach demonstrated that diffusion of water molecules in the presence of the field gradients inherent to lung alveoli can explain the experimentally observed multiexponential nature of the T_2 distribution in lung tissue. Moreover, exclusion of the diffusion effect facilitated the measurement of the inherent T_2 which has never been done before.

A new approach was taken to measure the diffusion coefficient of water in lung. By fixing the product of nTE at 60 ms, it allowed us to vary the diffusion factor while maintaining the T_2 weighting constant. This eliminated the uncertainty involved in determining the T_2 distribution and reduced the number of parameters. All and all, the experiments and calculations described in this thesis have shown that NMR techniques have the potential to resolve pathological changes. This work also demonstrates that, by adding accurate quantification and increased specificity, MRI techniques could eventually become part of routine diagnostic techniques for the assessment of pulmonary diseases.

9.2 Future Plans

9.2.1 Internal Magnetic Field Gradients and Diffusion Measurements

As shown in chapter 7, the internal magnetic field gradients in lung were estimated using a spherical shell model. It would be advantageous if we could experimentally measure these gradients and compare them with the estimated values. It has been demonstrated that the Applied Pulsed Field Gradient (APFG) is capable of measuring diffusion in systems with large background (internal) magnetic field gradients [102]. This technique eliminates the cross term, suppresses the effect of the internal gradients, and amplifies the effect applied gradient. This method could be used to determine D for very short times (less than 10 ms) and then one could use this diffusion coefficient to estimate the internal background gradients.

Moreover, a diffusion image could be generated by sampling the echo amplitudes from the APFG sequence in an imaging mode which would provide us with voxel-by-voxel information on D. This approach is advantageous and the diffusion information is not corrupted by imaging

gradients.

Also it is worthwhile mentioning that the lowest echo spacing which can be attained by the current equipment is 10 ms. We will soon have access to an MRI imager which enables us to apply these techniques on inflated lungs with a very short echo spacing. This is desirable because if the echo spacing is long, only spins experiencing weak gradients can be observed.

9.2.2 Perfusion

An accurate means of measuring microcirculatory flow is very advantageous and desirable. Motivations for a simple and quantitative measure of perfusion include pulmonary embolism in lung, brain ischemia following the stroke, assessment of gangrenous limbs, infarcted myocardium as an indication for bypass surgery, kidney function, and improved angiography techniques. In general, the transport of fluid elements at the capillary level is neither truly random nor deterministic. The NMR signal from a perfused system decays more rapidly than a stationary one due to a wide velocity distribution— this expedites the phase dispersion and, in turn, makes the signal decay more quickly.

Microcirculation has been studied by several investigators using NMR. But to date no formalism or technique has been comprehensive enough to include the general case of perfusion. We wish to understand the behavior of the perfused signal and develop a theory which enables us to look at the effects due to microcirculatory flow. To have a quantitative approach to the perfusion problem, we need to develop a model which takes into account parameters such as the susceptibility induced magnetic field gradient, the applied magnetic field gradient, porosity, and the time of NMR measurement. The theory should also account for the phase distribution

due to the magnetic susceptibility variation.

We also would like to test the theory by computer simulation and verify it by experiments; our experiments would include phantoms and volunteers. We may be able to use a computer-controlled pump system which can emulate the human heart. Possible phantom experiments would include flow through glass beads (the susceptibility induced magnetic field gradients would be dominant) and flow through gel beads (the applied gradient would be dominant). The former experiments would mimic the biological conditions in organs like lung, in which the flow is highly perfusive, and the latter experiments would be a good model for organs like brain.

Bibliography

[1] R. J. crystal, J. E. Gadek, V. J. Ferrans, J. D. Fulmer, *et al.*, *Am. J. Med.*, **70**, 542, (1981).

[2] R. J. Crystal, P. B. Bitterman, S. I. Renard, A. Hance, *et al.*, Ferrans, J. D. Fulmer, *et al.*, *N. Engl. J. Med.*, **310**, 154, (1984).

[3] D. H. Bowden, *Lab. Invest*, **50**, 487, (1984).

[4] O. Kawanami, V.J. Ferrans, R.C. crystal, *Lab. Invest*, **46**, 39, (1982).

[5] M. B. Strauss, A. R. Hargens, D. H. Gershani, *et al.*, *J. Bone. Joint. Surg*, **65A**, 656, (1983).

[6] G. B. Hart, R. C. Lamb, M. B. Strauss, *J. Trauma*, **23**, 191, (1983).

[7] A. A. Luisada (1970), *Pulmonary Edema* Warren H. Green. Inc, St louis Missouri, U.S.A.

[8] W. H. Noble, *Can. Anaesth. Soc. J.*, **27**, 286, (1981).

[9] American Lung Association (1975)), *Introduction to Lung Diseases*, Sixth Ed. American Lung Association, U.S.A.

[10] D. J. Prockop, K. L. Kivirikko, L. Tuderman, N. A. Guzman, *N. Engl. J. Med.* , **301**, 13, (1979).

[11] G. L. Laurent, *Thorax* , **41**, 418, (1986).

[12] K. S. Cheah, *Biochem. J.* , **229**, 287, (1985).

[13] B. C. Starcher, *Thorax* , **41**, 577, (1986).

[14] M. J. Fazio, D. R. Olsen, E. A. Kauth, C. T. Baldwin, *et al.*, *J. Invest. Derm.* , **91**, 458, (1988).

[15] C. H. Sear, M. E. Grant, D. S. Jakson, *Biochem. J.* , **194**, 587, (1981).

[16] G. M. Hass, *Arch. Pathol.* , **19**, 334, (1935).

[17] J. A. Pierce, R. V. Ebert, *Thorax* , **20**, 469, (1965).

[18] A. Huggert, E. Odelblad, *Acta. Radiol.*, **51**, 385, (1958).

[19] E. Odelblad, U. Bryhn, *Acta. Radiol.*, **47**, 315, (1957).

[20] E. Odelblad, B. Westin, *Acta. Radiol.*, **49**, 389, (1958).

[21] M. Goldsmith, J. Koutcher, R. Damadian, *Cancer*, **41**, 183, (1978).

[22] M. Goldsmith, J. Koutcher, R. Damadian, *Br. J. Cancer*, **36**, 235, (1977).

[23] H. E. Frey, R. R. Knispel, J. Jruuv, *et al.*, *J. .Natl. Cancer*, **49**, 903, (1972).

[24] T. A. Case, C. H. Durney, D. C. Ailion, *et al.*, *J. Magn. Reson.*, **73**, 304, (1987).

[25] C. H. Durney, J. Bertolina, D. C. Ailion, *et al.*, *J. Magn. Reson.*, **85**, 554, (1989).

[26] M. Kveder, I. Zupanicic, G. Lahajnar, R. Blinc, D. Suput, D. C. Ailion K. Ganesan, C. Goodrich, *Mag. Reson. Med.* **7**, 432 (1988).

[27] H. Kolem, C. Goodrich, K. Ganesan, D. C. Ailion, A. G. Cutillo, S. Chen, A. H. Morris, S. Shioya, and S. Watanabe, *S.M.R.M. Abstracts.* p685, (1989).

[28] S. Shioya, R. Christman, D. C. Ailion, *Mag. Reson. Med.* **16**, 49 (1990).

[29] S. Shioya, H. Kolem, D. C. Ailion, K. C. Goodrich, A. G. Cutillo, *Mag. Reson. Med.* **26**, 1 (1992).

[30] C. E. Hayes, T. A. Case, D. C. Ailion, *Science*, **216**, 1313 (1982)

[31] D. C. Ailion, T. A. Case, D. D. Blatter, A. H. Morris, A. G. Cutillo, C. H. Durney, S. A. Johnson, *Bulletin. Magn Reson.* **6**, 130 (1984).

[32] A. G. Cutillo, A. H. Morris, D. Blatter, D. C. Ailion, *J. Appl. Physiol*,**57**, 583 (1984).

[33] F. M. Maclennan, M. A. Foster, F. W. Smith, G. A. Crosher. *Br. J. Radiol.* **59**, 553 (1986).

[34] M. Kveder, G. Lahajnar, R. Blinc, I. Zupanicic, *Mag. Reson. Med.* **6**, 194 (1988).

[35] J. Zhong, J. Gore, *Mag. Reson. Med.* **19**, 276 (1991).

[36] G. Laicher, D. C. Ailion, A. G. Cutilo, *J. Magn. Reson. Series B*, **111**, 243, (1996).

[37] R. M. Cotts, M. R. Hoch, T. Sun, J. T. Marker, *J. Magn. Reson.*, **83**, 252, (1989).

[38] M. Goldman (1988). *Quantum Description of High-resolution NMR in Liquids*, Clarendon Press. Oxford.

[39] F. Bloch, W. W. Hansen, M. Packard, *Phys. Rev.*, **69**, 127, (1946).

[40] F. Bloch, W. W. Hansen, M. Packard, *Phys. Rev.*, **70**, 474, (1946).

[41] E. L. Hahn, *Phys. Rev.* **80**, 580 (1950)

[42] S. Meiboom, D. Gill, *Rev. Sci Ins. trum.* **29**, 688 (1958)

[43] E. O. stejskal, J.E. Tanner *J. Chem. Phys.* **42**, 288 (1965)

[44] A. G. Redfield, *IBM. J.* , **1**, 19, (1957).

[45] H. C. Torry, *Phys. Rev.*, **92**, 962, (1953).

[46] H. Stegemann, K. H. Stalder, *Clinica Chemica Acta*, **18**, 267, (1967).

[47] E. Sternin, *Rev. Sci. Instrum.*, **56**, 2043, (1985).

[48] C. S. Poon, R. M. Hankelman, *J. Magn. Reson. Imaging.* **2**, 541 (1992).

[49] K. P. Whittall, A. L. MacKay, *J. Magn. Reson.*, **84**, 134 (1989).

[50] M. Bloom, T. Holmes, H. Carolyn, E. Mountford, *J. Magn. Reson.*, **69**, 73 (1989).

[51] R. A. Christman, , D. C. Ailion, T. A. Case, C. H. Durney A.G. Cutillo, S. Shioya, K. C. Goodrich, A. H. Morris *Magn. Reson. Med.*, **73**, 6 (1996).

[52] D. D. Blatter, A. H. Morris, D. C. Ailion, A. G. Cutillo, T. A. Case, *J. Magn .Reson. B*, **102**, 293 (1993).

[53] P. Bendel, *J. Magn. Reson.*, **86**, 509 (1989).

[54] G. Laicher, D. C. Ailion, A. G. Cutillo, *Proc. SMR. Abstracts.* p 609, (1993).

[55] A. L. MacKay, *Biophys. J.*, **35**, 301 (1981).

[56] A. L. MacKay, E. Burnell, A. Bienvenue, P. F. Devaux, M. Bloom, *Biochem .Biophys. Acta.*, **728**,460 (1983).

[57] A. Abragam (1961), *principle of Nuclear Magnetism*, Oxford univ P ress, Oxford,UK.

[58] F. James, M. Roos, *Comput .phys. Commun.* **10**, 343 (1975)

[59] M. R. Estilaei, A. L. MacKay, C. Roberts, J. Mayo, *Proc.SMR. Abstracts*, p.1616, (1995).

[60] J. R. Mayo, A. L. MacKay, K. P.Whittall, E. M. Baile, P. D. Pare, *J. Thorac. Imag.* **16**, 73 (1995).

[61] A. G. Cutillo, A. H. Morris, D. C. Ailion, C. H. Durney, T. A. Case, *J. Thorac. Imag.* **1**, 39 (1986).

[62] F. E. Carrol, J. E. Loyd, K. B. Nolop, J. C. Collins, *Inves. Radiol.* **20**, 381 (1985).

[63] J. R. Mayo, N. L. Muller, B. B. Forester, M. Okazawa, *Can. Assoc. Radiol. J.*,**6**, 281 (1990).

[64] P. M. Philips, P. S. Allen, S. F. P. Man, *J. Appl. Physiol.* **66**,1197 (1989).

[65] C. P. Slichter, *Principle of Magnetic Resonance*, (1990), 3rd Ed.,Springer-Verlag, New York.

[66] S. Shioya, M. Haida, M. Fukuzaki, Y. Ono, *et al.*, *Ragn. Reson. Med.* **14**, 358 (1990).

[67] G. N. Ling, M. Tucker, *J. Natl. cancer. Inst.* **64**, 1199 (1980).

[68] G. Antonio, A. H. Morris, K. Ganesan, D. C. Ailion, T.A. Case, *Magn. Reson. Med.* 12, 137 (1989).

[69] P. A. Bottomly, C. J. Hardy, R.. Argesinger, G.A. Moore, *Med. Phys.* **14**,1 (1987).

[70] S. Shioya, M. Haida, C. T. Suji, *Mag. Reson. Med.* **8**, 450 (1988).

[71] J. R. Mayo, A. L. MacKay, N. Muller, *Radiology.* **177** ,313 (1990).

[72] S. Shioya, M. Haida, M. Fukuzaki, Y. Ono, M. Tsuda, Y. Onta, H. Yamabayashi *Mag. Reson. Med.* **14**, 358 (1990).

[73] J. D. Fulmer, R. G. Crystal *The Biochemical Basis of Pulmonary Function*

[74] C. L. Partain, A. E. James , F. D. Rollo, R. R. Price (1983), *Nuclear Magnetic Resonance Imaging*, Saunders, Philadelphia.

[75] E. S. Garnett, C. E. Webber, G. Coates, *et al.*, *Can. Med. Assoc. J.*, **116**, 153, (1977).

[76] L. J. Rosenblum, D. O. Manceri, D. E. Wellenstein, *et al.*, *Radiology*, **129**, 521, (1978).

[77] D. S. Simon, J. F. Murray, N. C. Staub, *J. Appl. Physiol.*, **47**, 1228, (1979).

[78] F. Fazio, T. Jones, C. G. C. MacArthur, C. G. Rhodes, *et al.*, *Brit. J. Radiol.* , **49**, 393, (1976).

[79] M. Estilaei, A. MacKay, C. Roberts, J. Mayo. *J. Magn. Reson.*, 124, 410 (1997).

[80] H. R. Wexler, R. L. Nicholson, F. S. Prato, L. S. Carey, S. Vinitski, L. Reese. *Invest. Radiol.*, **20**, 583 (1985).

[81] A. D. Siefkin, B. C. Nichols, *Am. Rev. Resp. Dis.*, **134**, 509 (1986).

[82] A. G. Cutillo, A. H. Morris, K. Ganesan, D. C. Ailion, T. A. Case, *Magn. Reson. Med.* **12**, 137 (1989).

[83] W. T. Sobol and M. Pintar, *Mag. Reson. Med.* **4**, 537 (1987).

[84] K. P. Whittall, A. L. Mackay, D. A. Graeb, R. A. Nugent, D. K. B. Li, D. W. Paty, *Magn. Reson. Med.* **37**, 34 (1997).

[85] R. S. Menon, A. L. MacKay, S. Flibotte, J. R. T. Hailey, *J. Magn. Reson.* **82**, 205 (1989).

[86] D. Zamir, R. C. wayne, and R. M. Cotts, *Phys. Rev. Iett.* **12**, 327 (1964).

[87] R. L. Cooper, D. B. Chang, A. C. Young, C. J. Martin, and B. Ancker Johnson, *Bul. Am. Phys. Soc.* **18**, p410 (1973).

[88] A. H. Morris, D. D. Blatter, T. A. Case, A. G. Cutillo, D. C. Ailion, C. H. Durney,and S. A. Johnson, *J. Appl. Physiol.* **58**, 759 (1985).

[89] S. Majumadar and J. C. Gore, *J. Magn. Reson.* **78**, 41 (1988).

[90] J. Zhong, R. P. kennan, and J. C. Gore, *J. Magn. Reson.* **95**, 267 (1991).

[91] A. L. Lucas, S. J. Gibbs, E. W. G. Jones, M. Peyron, J. A. Derbyshire and L. D. Hall, *J. Magn. Reson.* series A. **104**, 273 (1993).

[92] J. D. Jackson, (1962), *Classical Electrodynamics*, Wiley, New York.

[93] E. R. Weibel (1984), *The Pathway for Oxygen.* Harvard University Press, Cambridge, MA.

[94] E. R. Weibel (1980), *Design and Structure of the Human Lung.* In Pulmonary Diseases and disorders. Edited by A. P. Fishman, McGraw-Hill, New York.

[95] H. Y. Carr and E. M. Purcell, *Phys. Rev.* **94**, 630 (1954).

[96] J. E. Tanner, E. O. stejskal, *J. Chem. Phys.* **49**, 288 (1968).

[97] R. L. Cooper, D. B. Chang, A. C. Young, *Biophys.* **14**, 161 (1974).

[98] M. Neeman, J. P. Freyer, L. O. Sillerud, *J. Magn. Reson.* **90**, 303 (1990).

[99] M. E. Moseley, J. Kucharczyk, H. S. Asgari, D. Norman, *Magn. Reson. Med.* **19**, 321 (1991).

[100] F. A. Howe, A. G. Filler, B. A. Bell, J. R. Griffiths, *Magn. Reson. Med.* **28**, 328 (1992).

[101] J. Lian, D. S. Williams, I. J. Lowe, *J. Magn. Reson. series A* **106**, 65 (1990).

[102] R. F. Karlick, Jr., I. J. Lowe *J. Magn. Reson.* **37**, 75 (1980).

[103] X. Hong, W. T. Dixon, *J. Magn. Reson.* **99**, 561 (1992).

[104] R. C. Wayne, R. M. Cotts *Phys. Rev.*, **151**, 264, (1966).